ALMA MATER STUDIORUM · UNIVERSITY OF BOLOGNA

School of Science
Department of Physics and Astronomy
Master's Degree

Analysis of the production of ϕ-meson pairs in pp collisions with ALICE at LHC

Supervisor:
Prof.ssa Silvia ARCELLI

Co-Supervisor:
Dott. Roberto PREGHENELLA

Presented by:
Nicola RUBINI

Academic Year 2020/2021

University of Bologna

Abstract

School of Science
Department of Physics and Astronomy

Master's Degree

Analysis of the production of ϕ-meson pairs in pp collisions with ALICE at LHC

by Nicola RUBINI

My Thesis focuses on the analysis of the production of ϕ-meson pairs in proton-proton (pp) collisions. The measurement is performed with the ALICE detector at the LHC, exploiting its unique PID capabilities. It is motivated by the recent observations of enhanced production of strange and multi-strange hadrons, a possible signature of QGP formation, in high-multiplicity proton-proton collisions at the LHC.

This work starts with a presentation of the theoretical and experimental background of high-density QCD as studied in ultrarelativistic heavy-ion collisions. Special focus is given to the topic of strangeness enhancement and to models for hadron production. The ALICE Experiment and its performance are reviewed in the second chapter. In the third chapter a walk-through will be given from the idea pushing for the development of this analysis, all the steps that have been followed to establish it, to the final state of the analysis framework. Here we will make use of the theoretical models introduced earlier to explain ideas and assumptions that drove the realisation of the project.

The core of the work carried out for this Thesis concerns the development of a technique, novel within the ALICE Experiment, for the measurement of correlated production of ϕ mesons. The measurement being proposed is inspired by the phenomenology of the Lund string fragmentation, which is a microscopic QCD-inspired phenomenological model for hadron production.

The approach is a full review of the technique development from concept to deployment on data with special focus on the issues and solutions encountered and adopted along the way. The main idea of the technique is to generalise the invariant mass technique for the reconstruction of short-lived particles to two dimension, to extract the signal from its irreducible background. The review will firstly examine how to build two dimensional invariant-mass histograms and the challenges and assumptions made in the present analysis framework, such as symmetrisation filling and coupling conditions for the subject particles. Secondly the signal extraction is considered: the extension of the fit in two invariant-mass dimensions and the modelling of the signal and background and how to constraint them from one-dimensional templates. Thirdly the issue of efficiency corrections is taken over, with a comparison between a natural 2-dimensional approach, against a somewhat more sophisticated combination of 1-dimensional efficiencies.

After the developed of the framework, this first prototype is used to produce preliminary results on real ALICE data for pp collisions at $\sqrt{s} = 7$ TeV.

University of Bologna

Abstract

School of Science
Department of Physics and Astronomy

Master's Degree

Analysis of the production of ϕ-meson pairs in pp collisions with ALICE at LHC

by Nicola Rubini

La mia tesi si focalizza sull'analisi della produzione di coppie di mesoni ϕ in collisioni protone-protone. La misura é stata fatta ad ALICE, presso l'LHC, sfruttando le sue eccellenti doti di Particle Identification. É motivata dall'osservazione di un aumento di produzione di adroni strani e multi-strani, una possibile indicazione per la formazione di QGP, in collisioni protone-protone ad alta molteplicitá.

Il cuore del lavoro di questa tesi riguarda lo sviluppo di una tecnica, nuova all'interno dell'esperimento di ALICE, per la misura della produzione correlata di mesoni ϕ. La misura proposta prende ispirazione dal modello a stringhe di Lund, che é un modello fenomenologico ispirato dalla QCD microscopica per la produzione di adroni.

Seguiremo l'approccio di una review completa dell'analisi dal concepimento al suo utilizzo sui dati con un focus speciale sui problemi incontrati e le soluzioni proposte nel suo sviluppo. L'idea principale della tecnica é una generalizzazione della tecnica della massa invariante per la ricostruzione di particelle a vita media corta in due dimensioni, per estrarre il segnale dal suo fondo irriducibile. La review esaminerá prima di tutto il metodo con cui viene costruito l'istogramma bi-dimensionale, con le problematiche e assunzioni ad esso associate, come per esempio il riempimento simmetrico e le condizioni di accoppiamento dei candidati. Successivamente viene considerata l'estrazione del segnale: l'estensione del fit sull' istogramma bi-dimensionale viene descritto nelle sue componenti di fondo e segnale e come vengono estratte informazioni preziose per questo processo dagli istogrammi mono-dimensionali. Verrá poi valutata l'efficienza, comparando la naturale efficienza 2-Dimensionale con un approccio piú raffinato dato dal prodotto di efficienze 1-Dimensionali. In ultimo il tema dell'estrapolazione del segnale viene considerato.

Dopo lo sviluppo dell'analisi, un primo prototipo viene impiegato per produrre una prima misura preliminare con dati veri di ALICE per collisioni protone-protone a $\sqrt{s} = 7$ TeV.

Contents

Introduction

The purpose of this work is to establish and validate an analysis framework aimed at the measurement of the pair production of ϕ mesons in proton-proton collisions. This thesis is organized as follows:

The First Chapter will be devoted to a general overview of the physical phenomena That are studied as part of the experimental programme of the ALICE experiment. Moreover we will go into some detail on some of the phenomenological models that currently best describe the data. Another item that will be a discussed is the Strangeness Enhancement phenomena, and more generally the strangeness production in hadron and heavy-ion collisions.

The Second Chapter will be devoted to a general overview of the detectors? performance in the ALICE experiment. We will describe the detectors structure and their basic functioning. After that we will explain the methodologies adopted for track reconstruction and particle identification, together with their resolution and efficiency.

The Third Chapter will focus on the development of the analysis technique and its validation through a simplified analysis based on the Pythia8 Monte Carlo. After the analysis has been laid down, a validation to compare results to the Monte Carlo truth is performed to establish the reliability and performance of the technique.

The Fourth Chapter will be devoted to the description of the results obtained by applying this technique on real data collected by the ALICE experiment. Moreover, the signal extraction systematics will be measured as a first estimate, and the results on the pi meson production will be presented.

Chapter 1

Fundamental Physics at the ALICE experiment

The ALICE (A Large Ion Collider Experiment) Collaboration at LHC aims at studying the Physics of strongly interacting matter at high energy densities [1]. At the energy densities reached in ultra-relativistic heavy-heavy-ion collisions a new state of matter emerges: the Quark-Gluon Plasma (QGP) which is one of the main subjects of research of the collaboration. This state of matter represents what is thought to have been the Universe a tiny fraction of a second ($\approx$1 µs) after the Big Bang, thus giving useful insights on how it all came to be. The focus of the experiment are ion-heavy-ion collisions, but proton-proton and proton-heavy-ion collisions are studied as well, as a mean of comparison to ion-ion and in their own right. The more general scope is the study of Quantum Chromodynamics (QCD) as a whole, investigating confinement, deconfinement and chiral phase transitions. Quark-Gluon Plasma

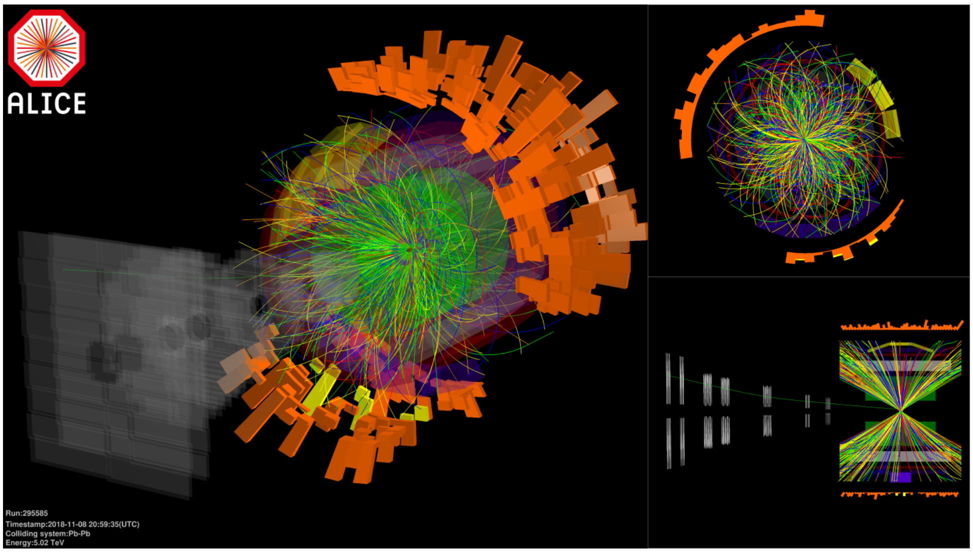

FIGURE 1.1: Particle showers in the ALICE detector during the first lead nuclei collisions the 2018 data taking period (Image: ALICE/CERN)

1.1 Quantum Chromodynamics

Quantum Chromodynamics (QCD) is the theory which describes the dynamics of the Strong interaction [2] in the Standard Model (SM). It is based upon two fundamental ideas:

- The existence of a color quantum number, describing the three color charges: Yellow, Red and Blue.
- The symmetry transformations are coordinate dependent as a local gauge theory, and their derivatives are absorbed in some gauge transformations of a set of massless vectors, the gluons.

The QCD is a non Abelian Gauge Theory based on the color group SU(3)$_c$, that is an intrinsic degree of freedom of color charge, this implies a local invariance for the non commutative group transformation. This degree was introduced in the Quark Model to achieve a fully skew-symmetric wave function accordingly to the Pauli principle. The interaction generated are described in the theory by the Lagrangian density:

$$\mathcal{L} = \bar{\psi}_q^i (i\gamma^\mu)(D_\mu)_{ij}\psi_q^j - m_q \bar{\psi}_q^i \psi_{qi} - \frac{1}{4} F_{\mu\nu}^a F^{a\mu\nu} \tag{1.1}$$

where $\psi_q = (\psi_{qR}, \psi_{qG}, \psi_{qB})^T$ is the quark field and the i index runs through the colors, γ^μ are the Dirac matrices, indicating the interaction is of the vector type and m_q gives the possibility for quarks to be massive, for example through the Higgs mechanism. $F_{\mu\nu}^a$ is the gluon strength field with adjoint color index a and D_μ is the covariant derivative in QCD:

$$(D_\mu)_{ij} = \delta_{ij}\partial_\mu - i g_s t_{ij}^a A_\mu^a \tag{1.2}$$

where g_s is the strong coupling ($g_s^2 = 4\pi\alpha_s$), A_μ^a is the gluon field and t_{ij}^a is proportional to the hermitian traceless Gell-Mann matrices of SU(3) with $t_{ij}^a = \frac{1}{2}\lambda_{ij}^a$.

1.1.1 Strong Coupling

The magnitude of the interaction is defined by the strong coupling g_s, is proportional to α_s. To give us a scale of comparison we can evaluate α_s with respect to α_{em}, the fine structure constant, characteristic of the electromagnetic interaction.

$$\alpha_{em} = \frac{e^2}{4\pi\varepsilon_0\hbar c} \approx \frac{1}{137} \qquad \frac{\alpha_s}{\alpha_{em}} \approx 100 \tag{1.3}$$

To first approximation, the QCD is scale invariant. That is, ideally the jet substructure should reproduce itself over again in a fractal fashion. This is called the Bjorken scaling, and it is a phenomena best captured by the limit of *dimensionless* kinematic quantities, such as scattering angles and ratios of energy scales.

On top of this simple behaviour there is the phenomenon of the running constant: the coupling is not absolutely scale invariant and it is in fact sensitive to the energies involved in the process: one possible parametrisation of such scaling is described in Eq. 1.4 (See Fig. 1.2).

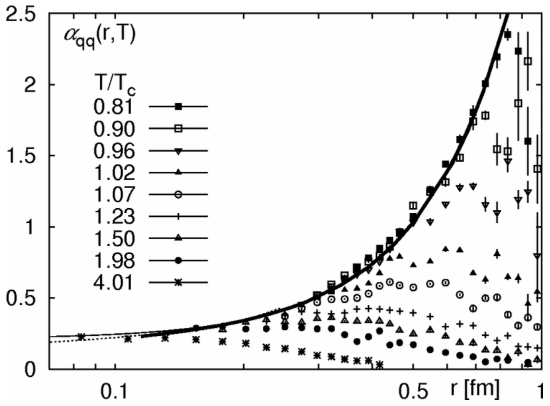

(A) The α_s against distance at different temperatures from Lattice QCD technique

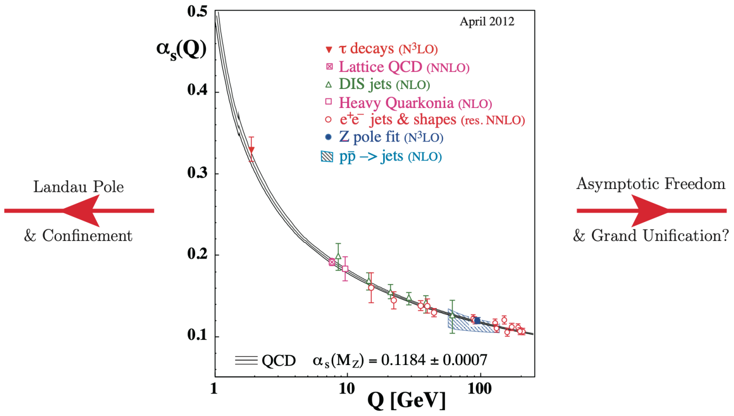

(B) Illustration of the running of α_S in a theoretical calculation (band) and in physical processes at different characteristic scales, from [2]. The little kinks at Q = m_c and Q = m_b are caused by discontinuities in the running across the flavor thresholds.

FIGURE 1.2: The strong coupling intensity as a function of transferred momentum and distance, highlighting the fact that it is not constant.

$$\alpha_s(Q^2) = \alpha_s(M_Z^2)\frac{1}{1 + b_0'\alpha_s(M_Z^2)\ln\frac{Q^2}{M_Z^2} + \mathcal{O}(\alpha_s)} \tag{1.4}$$

$$\lim_{Q^2\to\infty} \alpha_s(Q^2) = 0 \tag{1.5}$$

$$\lim_{Q^2\to 0} \alpha_s(Q^2) = \infty \tag{1.6}$$

Asymptotic freedom What is inferred by Eq. 1.5 is that in the limit of high energy the quarks are essentially free. That is the strong coupling effectively scales with the energies at play in a given process. This reduction at infinitely large energies means that perturbative theory may yield more and more precise predictions at higher energies.

Confinement What is inferred by Eq. 1.6 is that the soft processes in QCD are not approachable by a perturbation theory, at least not completely, because of the large values of the coupling. This means that other types of descriptions shall be used, such as phenomenological models based on experimental observations. One way to make the divergence more clear is to rewrite the coupling as:

$$\alpha_s(Q^2) = \frac{1}{b_o \ln \frac{Q^2}{\Lambda^2}}, \quad \Lambda \approx 200\,\text{MeV} \tag{1.7}$$

Where Λ should be the nominal energy for the divergence. It is useful to note that this is a parametrisation that does not necessarily imply that the physical quantity itself diverges.

1.1.2 Hard Processes

Hard processes are those where the energies involved are high, meaning the effective strong coupling admits a perturbation approach. The starting point is the Matrix Elements (MEs) which can be calculated at fixed orders. As an example, let's take one of the most occurring processes in hadron collisions, the Rutherford scattering of two quarks via a t-channel gluon exchange:

$$qq' \to qq' : \frac{\mathrm{d}\sigma}{\mathrm{d}\hat{t}} = \frac{\pi}{\hat{s}^2}\frac{4}{9}\alpha_s^2\frac{\hat{s}^2+\hat{u}^2}{\hat{t}^2} \tag{1.8}$$

where u, t, s, are the Mandelstam variables. This is the basic interaction probability, more corrections are needed to accurately describe a real event.

The first problem encountered during the calculation of this cross section is the hadron substructure. Hadrons are nominally formed by 2 or 3 quarks kept together by gluons, but the reality is that they are a cloud of multiple gluons and quarks constantly created and annihilated. This issue can be conveniently neglected making some consideration on the energy of the process; in this range the substructure of the target hadron is conveniently frozen in time. This effect rises from the fact that for the hadron to remain intact high-virtuality fluctuations are to be suppressed by powers of $\alpha_s\Lambda^2/|k|^2$, with k being the virtuality of the fluctuation. This restricts most fluctuations in timescales of Λ^{-1} whilst the process occurs over much smaller timescales $Q^{-1} \ll \Lambda^{-1}$. This means that the whole scattering happens whilst the substructure barely moved, effectively taking a "picture" of the hadron.

The direct consequence of this is that we can factorise the cross section into the parton distribution function (PDF), parametrising the hadron inner structure, and the partonic cross section (PCS) that ignores the hadron structure and only focuses on the struck quark interaction. For a hadron-hadron scattering, this factorisation takes the form:

$$\sigma_{h_1h_2} = \sum_{i,j}\int_0^1 \mathrm{d}x_i \int_0^1 \mathrm{d}x_j \sum_f \int \mathrm{d}\Phi_f \underbrace{f_{i/h_1}(x_i,\mu_F^2)f_{j/h_2}(x_j,\mu_F^2)}_{\text{PDF}} \underbrace{\frac{\mathrm{d}\hat{\sigma}_{ij\to f}}{\mathrm{d}x_i\mathrm{d}x_j\mathrm{d}\Phi_f}}_{\text{PCS}} \tag{1.9}$$

The parameter μ_F is the factorisation scale. This quantity is arbitrary and depends on the problem examined; it is meant to represent the maximum fluctuation energy for the PDFs and the lowest fluctuation energy for the PCSs.

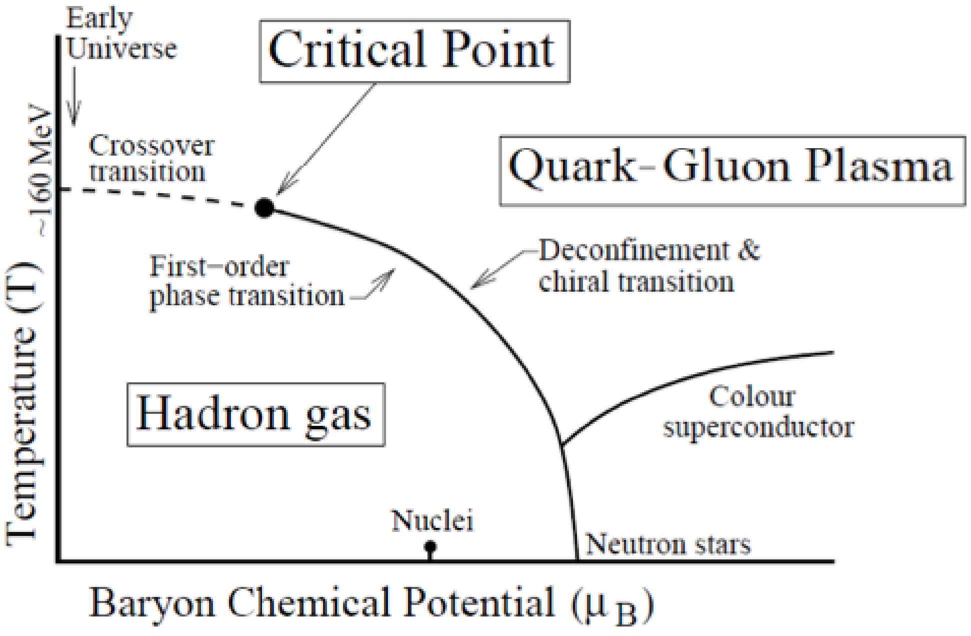

FIGURE 1.3: The Phase transition chart for QGP

PDFs: PDFs are usually unpredictable or hardly predictable by the theory and are inferred from data.

PCSs: PCSs are usually truncated at the desired precision, using perturbative QCD (pQCD)

1.1.3 Soft Processes

Soft processes are those where the energy scales are low, meaning the effective strong coupling does not admit a perturbation approach. The most common example of this kind of situations is *hadronisation*, which is going to be the topic of Section 1.3.

1.2 Phase transition in QCD: The Quark-Gluon Plasma

The phase transition in QCD can be seen in Figure 1.3. In fact when the temperature and the baryonic density, exceed critical values the coupling constant can no longer keep the confinement and a transition to a free state occurs: the QGP forms. The transition is closely related to the flavours and masses of the quarks at hand, as the process itself is closely related to the chiral symmetry.

We can now search the critical temperature at which the transition starts. To do so we will examine the critical temperature for relativistic pions, as those are the lightest hadrons. We will use the statistical thermodynamics principles to study our state of free quarks.

Grand Canonical Ensemble: We will make use of the Grand Canonical ensemble, as it represents an open set of particles that can exchange matter and heat with its surroundings. We start by recalling the fundamental relation

$$dE = TdS - pdV + \sum_{i=1}^{n} \mu_i dN_i, \tag{1.10}$$

where we can find all the classical thermodynamic variables and μ_i, which is the energy the system takes or releases when adding or removing a particle of the i-th specie and is called the chemical potential.

$$\mu_i = \frac{\partial E}{\partial N_i} \tag{1.11}$$

This potential grants the mean conservation, over major volumes or the whole system, of the i-th specie. We will focus for now on the *baryonic potential*, that is the chemical potential for particles holding a baryonic charge, because the baryonic number $B = (n_q - n_{\bar{q}})/3$ is conserved in all SM processes.

To have a glimpse at the QGP we can study a pion gas, the simplest hadron gas, and compare its properties to those of a gas of free quark and gluons. As Nature always chooses the states of highest pressure, or least mean free energy, the transition should occur at coinciding pressures [3] between the pion gas and the quark and gluon gas. We now deal with two types of free particle, quarks as fermions and gluons as bosons. Upon considering the appropriate quantum statistic for each type, integrating over the whole energy spectrum we can find:

$$N = g_{int} \int_0^{\infty} g(E) \frac{dE}{e^{\beta(E-\mu)} \pm 1}. \tag{1.12}$$

We can now consider the Semi-Classical approach, using the average over the statistical ensemble and the uncertainty principle to get a better approximation of the reality. Moreover we suppose that the energy necessary for the QGP to form is high enough to ignore the energy at rest for the relativistic particles, and get $E \approx p$. Now, from 1.12, the density for the QGP is

$$n_i = \frac{N_i}{V} = \int \frac{d^3 p_i}{2\pi} \frac{1}{e^{\beta E} \pm 1}, \tag{1.13}$$

and the energy density for the i-th particle is

$$\varepsilon_i = \frac{E_i}{V} = g_i \int \frac{d^3 p_i}{2\pi} \frac{1}{e^{\beta E_i} \pm 1}, \tag{1.14}$$

where g_i is the number of internal degrees of freedom of the particle and we have $g_b \frac{\pi^2}{30} T^4$ for fermions and $g_f \frac{7}{8} \frac{\pi^2}{30} T^4$ for bosons. The total energy density is

$$\varepsilon_{QGP} = \left(g_b + \frac{7}{8} g_f\right) \frac{\pi^2}{30} T^4 \quad \rightarrow \quad 37 \frac{\pi^2}{30} T^4 \tag{1.15}$$

The substitution was made considering that a gluon (g_b) has 16 degrees of freedom, accounting for 2 spin states and 8 color states, whilst a quark (g_f) has 12, accounting for 2 spin states, 3 color states and 2 flavours, if we only consider *up* and *down* quarks.

If we consider a pion gas, the values for the two variables are 0 and 3, being pions scalar particles. This gives us

$$\varepsilon_{\pi} = \frac{\pi^2}{10} T^4 \tag{1.16}$$

Furthermore we ask to find the pressure (P) of the gas, that is $P = \varepsilon_\pi/3$. At this point we need to deal with our approximations and add a term to the pressure we did not account for. That is $B \approx 0.5$ GeV/fm, that can be derived form Lattice QCD calculations. This additional term represents the confinement pressure the pions are subject to. Finally the pressure of the pion gas and QGP read as:

$$P_\pi = 3\frac{\pi^2}{90}T^4 + B, \qquad P_{QGP} = 37\frac{\pi^2}{90}T^4 + B. \tag{1.17}$$

Given the fact that the transition occurs when the pressures equal each other, we can compare them and find a critical temperature at which the QGP forms:

$$T_c = \left(\frac{45}{17}\frac{B}{\pi^2}\right)^{\frac{1}{4}} \approx 180\,\text{MeV} \tag{1.18}$$

Which is consistent with experimental data.

1.2.1 Evolution of the QGP

In high energy collisions many steps occur that lead to the final hadronisation process.

First Collision The primary fireball forms, every participant equilibrates in momentum and the total entropy of the process is compressed in a very small portion of space-time

Birth of the Fireball All the participants in equilibrium give in energy for internal processes as production of new flavours (s quarks) takes over: the fireball is formed and is in thermal equilibrium.

Hadronisation The fireball starts producing massive quarks and depletes in free gluons, the conservation laws disrupt the chemical equilibrium and stop the continuous production and annihilation of flavours: as the fireball cools down the strong force re-establishes as an unbreakable bond among quarks, hadrons start to form with an available space-phase probability.

Chemical freeze-out Hadrons are now fully formed and are projected out of the collision, stopping the changes in relative yields of particles.

Kinetical freeze-out The particles are now far enough apart that there are no more elastic scatterings allowing the exchange of heat between particles. The momenta are now constant along with their temperature ($\mathrm{T_{kin}}$).

Experimental Data for the QGP hypothesis The Experimental data supporting the QGP hypothesis are various, but are all based on the secondary reconstruction of the particles we detect. That is because of the short lifetime of the QGP in the laboratory frame, as the conditions in which it can subsist long enough to be directly measured are quite hard to achieve; the probes should be [4]:

1. Operational in the collision time scale, roughly 10^{-23}s.
2. Sensitive to the local color charge deconfinement.

3. Dependent on the gluon degrees of freedom, which is the characteristic new dynamical degree of freedom.

One of the most suitable probes, satisfying all requirements, is the Strangeness Enhancement, even though there are many others. Usually the probes are classified in three categories: *Soft*, *Hard* and *Electromagnetic*

1.2.2 Soft Probes

Soft probes are linked to particles emerging from the collision with low transverse momentum. Usually these particles are created in the hadronisation phase of the fireball, thus giving a direct hint on the processes concurring in the production of final states in a QGP environment.

Hadrochemistry

One way to establish useful information about the QGP is to study the hadronisation processes that occur in the collisions. The most straight-forward example is to measure particle yields. In fact many researches have focused their efforts in establishing discrepancies between experimental data and model predictions for various types of particle and resonances.

Hadronic Resonances: Hadronic Resonances are excited states of a given particle. Their effectiveness as a probe depend on their mean lifetime: the lifetime of the QGP is expected to last $\approx 10\,\mathrm{fm/c}$, so a resonance with a comparable lifetime represents a strong signature. This is because the resonance can decay before it exits the dense hadron gas and its decay products will not allow one to reconstruct the resonance as they will lose their correlation. In this context a good candidate is the $\Lambda(1520)$ with a mean lifetime of $\approx 13\,\mathrm{fm/c}$ or the $\mathrm{K}^*(892)^0$ with a mean lifetime of $\approx 4\,\mathrm{fm/c}$. Along the destructive effect, there also is a re-generation effect, partially re-establishing the original yield. This regeneration process comes from the scattering of decay products with each other, that will produce new resonance correlations. Experimental results in recent years have highlighted the suppression of the $\Lambda(1520)$ yield with respect to the sole hadronisation mechanism (Fig. 1.4a).

Strangeness Enhancement: This will be the main focus of the next section, where a more extensive and detailed description will be given. The main concept of this phenomenon is that in the QGP the production cross section for strange quarks is enhanced until it reaches a saturation. Strangeness Enhancement has been well established in heavy-heavy-ion collisions and has been recently observed in high multiplicity pp collisions (Fig. 1.4b).

Fluid Dynamics

Fluid dynamics come into play as a QGP probe. The plasma behaves as a nearly perfect fluid, and thus will have a certain gradient of pressure, coming from the anisotropy of the collision geometry [7]. This has a repercussion over the particle yields in the final state when differentiated in the azimuthal angle, whereas a nn-fluid scenario would predict no effects with respect to the initial state geometry. To identify this anisotropic flow, the momentum distributions of the particle yields are

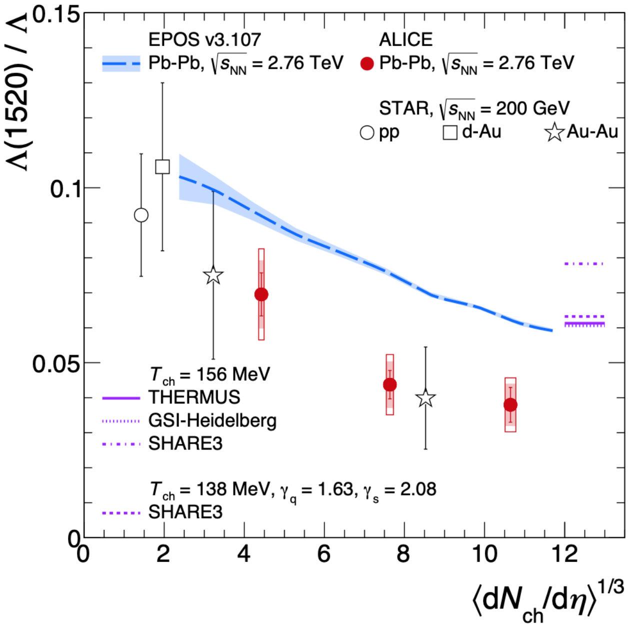

(A) p_T-integrated ratio of Λ(1520)/Λ production as a function of $\langle dN_{ch}/d\eta \rangle^{1/3}$. Predictions from several SHMs and from EPOS3 are also shown [5].

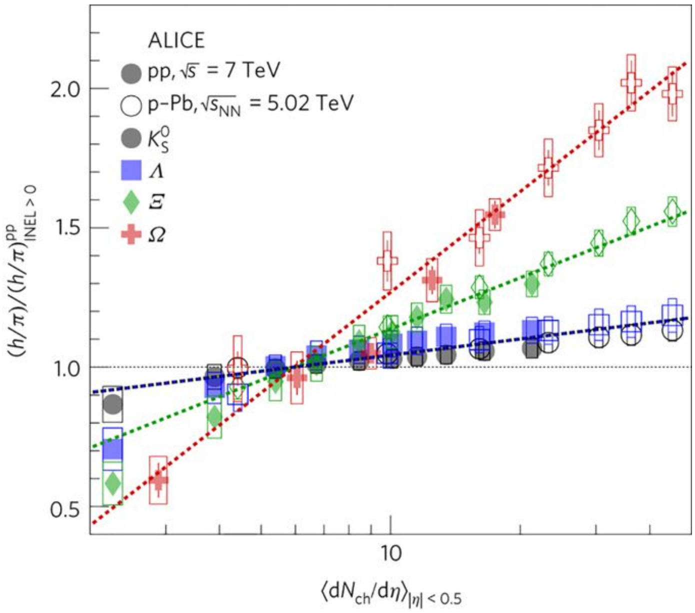

(B) Particle yield ratios to pions normalized to the values measured in the inclusive INEL > 0 pp sample [6].

FIGURE 1.4

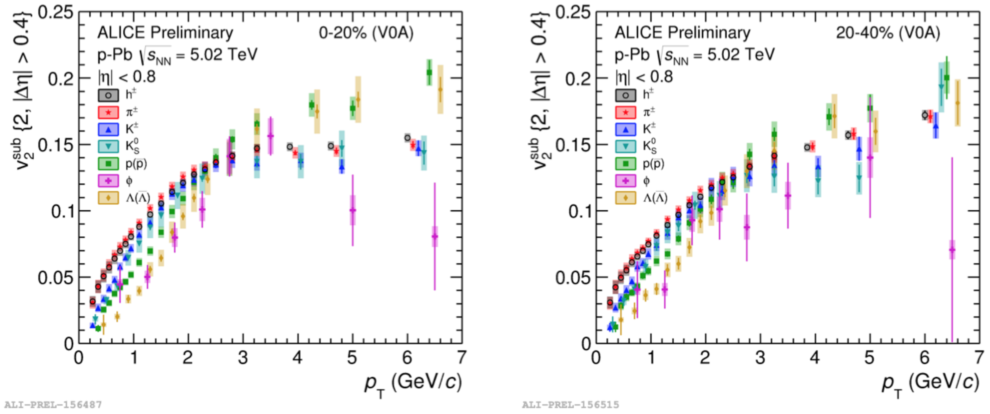

(A) Elliptic flow ν_2 for p-Pb collisions at $\sqrt{s_{NN}} = 5.02$ TeV for various species.

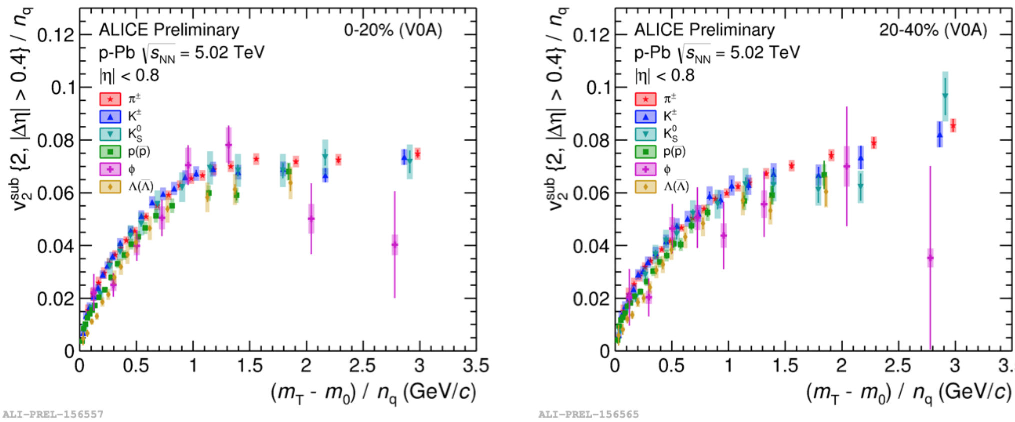

(B) Transverse kinetic energy (KE$_T$) scaling, where rest mass m_0 of individual species is subtracted from m_T, See [7]

FIGURE 1.5

expanded with the Fourier series:

$$E\frac{dN}{d\vec{p}} = \frac{1}{2\pi}\frac{d^2N}{p_T dp_T dy}\left[1 + 2\sum_{n=1}^{\infty}\nu_n \cos[n(\varphi - \Psi_n)]\right] \tag{1.19}$$

Where φ is the azimuthal angle, Ψ_n is the n-th harmonic symmetry plane, $\nu_n = \langle \cos n(\varphi - \Psi_n) \rangle$ are the anisotropic flow coefficients. The most interesting coefficient is the second, as it has a predominance, and it is called elliptic flow.

Experimental results Experimental results in recent years have proven this collective behaviour is found in pp collisions, p-Pb collisions and heavy-heavy-ion collisions. Figure 1.5 shows the typical results for the elliptic flow measured in p-Pb collisions.

1.2.3 Hard Probes

Hard probes are linked to particles emerging from the collision with high p$_T$[8]. There is a characteristic quantity evaluating the impact of the QGP on such particles,

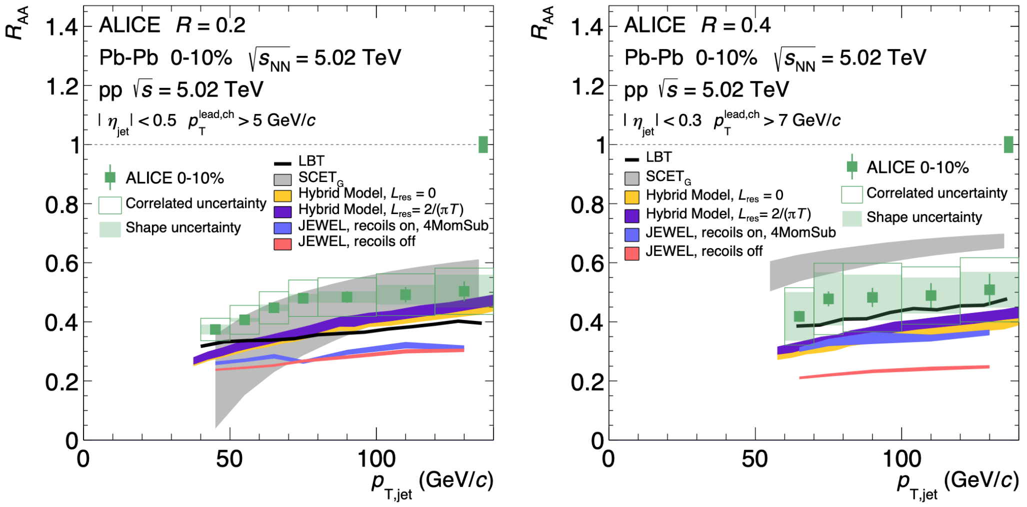

FIGURE 1.6: jet R_{AA} at $\sqrt{s_{NN}}$ = 5.02 TeV for R = 0.2 (left) and R = 0.4 (right) (R $\leq \sqrt{\Delta\phi^2 + \Delta\eta^2}$) compared to LBT, SCET$_G$, Hybrid model, and JEWEL predictions. The combined $\langle T_{AA} \rangle$ uncertainty and pp luminosity uncertainty of 2.81% is illustrated as a band on the dashed line at $R_{AA} = 1$. Systematic uncertainties are only included for the SCET$_G$ and Hybrid model predictions; see [9] for details

the nuclear modification factor:

$$R_{AA} = \frac{dN_X^{AA}/dp_T}{N_{\text{coll}} \cdot dN_X^{pp}/dp_T} = \frac{dN_X^{AA}/dp_T}{T_{AA} \cdot d\sigma_X^{pp}/dp_T} \tag{1.20}$$

Where N_{coll} is the number of binary nucleon-nucleon collisions, X is a given species or structure under scrutiny, AA and pp is heavy-ion collisions and pp collisions related respectively, T_{AA} is the nuclear overlap.

We can interpret this factor as the measurement of potential effects of any phenomena happening in heavy-ion collisions on the final yields of particles. That is because if no phenomena related to the nuclear nature of the collision is taking place, in such collisions one would expect the observables to be roughly the superimposition of N pp collisions. Usually this factor is studied for processes unrelated to the QGP hadronisation, instead it is useful as a mean of using pre-existing hadrons as probes traveling through the QGP medium.

Jet Quenching

The single parton, interacting strongly with the surrounding particles, emits a wide range of secondary products that interact themselves with any medium that might be present. The collection of these particles emerging from this interaction is called a jet. The Physics of jets aims to reconstruct the full kinematics of the multiple production from a single fast parton. One can then compare the results in heavy-ion collisions with what is expected in vacuum measuring the differences with the R_{AA} factor. The sum of the effects of medium on a jet is called jet Quenching. Common marks of jet quenching are the yield suppression and the energy imbalanced back-to-back di-jet pairs [9]. Experimental results in recent years have evaluated the nuclear modification factor for jets [10]. The R$_{AA}$ refers to Eq. 1.20.

Quarkonia melting

Quarkonium is a bound state of heavy quarks ($J/\psi, \Upsilon$). Their production is limited to initial hard scatterings of hadrons and cannot go on in the QGP, as the energy is too low: as we have seen the temperature of the plasma is of $\approx$ 180 MeV while the bottom quark mass is $\approx$ 4180 MeV [11]. The way they are used as probes is to understand the magnitude of colour deconfinement: due to the Debye screening mechanism the distance of deconfinement increases above the hadron dimension, dissolving it. Given the dependence of the suppression on the hadron dimensions we can expect the suppression to be differently impacting every species.

On top of the suppression mechanism, a recombination effect has also been observed in high energy collisions: once the hadron dissolves in the plasma, $c\bar{c}$ and $b\bar{b}$ roam freely in thermal equilibrium thus giving availability to their statistical recombination in Quarkonium bound states. If the energy in the collision is increased, the initial hard scattering will produce more $q\bar{q}$ and the final recombination will be more likely, even between quarks not coupled at production. Experimental results in recent years showed the predicted behaviour is confirmed: an increase in the collision energy results in an enhancement in the yield of Quarkonia state, and a different configuration of the Quarkonium affects the yield (Tab. 1.1).

	$\Upsilon(1S)$		$\Upsilon(2S)$
$\sqrt{s_{NN}}$	2.76TeV	5.02TeV	5.02TeV
R_{AA}	$0.30\pm_{st}0.05\pm_{sy}0.04$	$0.37\pm_{st}0.02\pm_{sy}0.03$	$0.10\pm_{st}0.04\pm_{sy}0.02$

TABLE 1.1: MeasuredR_{AA} for the $\Upsilon(1S)$ at $\sqrt{s_{NN}}$ = 2.76 TeV[12] and for the $\Upsilon(1S)$, $\Upsilon(2S)$ at $\sqrt{s_{NN}}$ = 5.02 TeV[13] in the forward rapidity region 2.5 < y < 4 in transverse momentum p_T < 15 GeV/c

1.2.4 Electromagnetic Probes

There are mainly two ways the QGP formation leaves his trace in the electromagnetic channel: photon and dilepton production [14].

Photons

There are essentially two sources of photons in relativistic heavy-ion collisions:

1. *Decay Photons*: The photons coming from hadronic decays, usually H$\rightarrow \gamma$+X, for example $\pi^0 \rightarrow \gamma\gamma$
2. *Direct Photons*: Produced in the primary interaction or in the evolution of the fireball
   (a) *Hard Photons*: These typically have high p$_T$ and are produced in:
      i. The initial hard N+N collisions
      ii. jet Fragmentation
   (b) *Thermal Photons*:
      i. *QGP generated*:
         A. $q\bar{q}$ annihilation: $q + \bar{q} \rightarrow g + \gamma$

        B. Compton Scattering: $q + g \rightarrow q + \gamma$
    ii. *Hadronic*:
        A. Secondary mesonic interactions: $m + m' \rightarrow m + \gamma$
        B. Hadronic Bremmstrahlung: $m + m' \rightarrow m + m + \gamma$

The Physics of photons as a probe in heavy-ion collisions comes form their large mean free path: they do not interact after production with the hot dense medium. In this scenario, if we imagine all phases to emit a certain kind of photons, the measured yield represents the integral of all emission sources along the evolution of the fireball. In particular low p_T photons carry information about the hot dense fireball.

Dileptons

Dileptons are essentially pairs of e^-e^+ or $\mu^-\mu^+$ that are produced in all stages of the collision from photons and have the advantage of having the invariant mass, as a reconstructed variable which constitutes an additional degree of freedom that can be exploited to investigate their origin. Their main sources are:

1. *Hadronic Sources*, depending on the invariant mass (GeV/c^2):
    - ≤ 1 Mainly decay of mesons, baryons and hadronic bremsstrahlung
    - 1 - 3 Leptons from correlated $D + \overline{D}$ pairs and multi-meson interactions
    - ≥ 3 Decay of vector mesons and initial Drell-Yan annihilation $q + \overline{q} \rightarrow l^+ + l^-$
2. *Thermal QGP Dileptons*:
    (a) Thermal annihilation $q + \overline{q} \rightarrow l^+ + l^-$
    (b) Compton Scattering $q + g \rightarrow q + l^+ + l^-$

The main information form the dilepton channel come from two invariant mass (M$_{\text{inv}}$) regions (GeV/c^2):

M$_{\text{inv}}$ $\in$[0.2 - 0.6] Increase in yield due to the formation of hadronic resonances and deformation of vector mesons in the hot and dense medium of the QGP.

M$_{\text{inv}}$ $\geq$ 1.2 Increase in yield due to the QGP radiation.

Recently there has been the measurement of the elliptic flow for the inclusive photon yield [15]. The measured photons are direct photons coming from all stages of the fireball, thus following the matter producing them. This behaviour will eventually mirror the collective flow of hadrons in the fireball (Fig. 1.7).

1.3 Hadron production and Strangeness Enhancement

The Physics of hadron production focuses on processes at the *hadronisation scale* $Q_{had} \approx 1$ GeV, that are comfortably in the non perturbative regime of QCD. This gives rise to general Physics models that are quite numerous, as many specialise to give a good approximation for specific issues, energy ranges or conditions, for which they almost perfectly fit the data; nonetheless, going out of their designed purpose will likely decrease or nullify their predictive power. These phenomenological models inevitably need to re-adapt to data analyses whenever discrepancies are found.

The hadronisation phase comes second to the initial hard scattering, posing the problem of "mapping" a set of partons to on-shell colour-singlet hadronic states. The

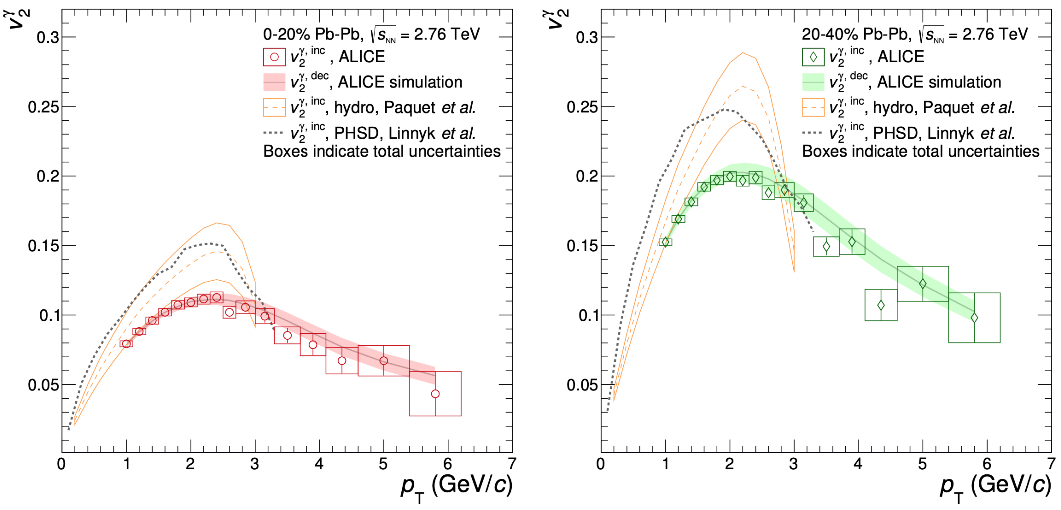

FIGURE 1.7: Elliptic flow of inclusive photons and decay photons, compared to hydrodynamic and transport PHSD model predictions in the 0-20% (left) and 20-40% (right) centrality classes. The vertical bars on each data point indicate the statistical uncertainties and the boxes indicate the sizes of the total uncertainties; see [15].

main steps in the Monte Carlo implementations of these models, and consequently what they are asked to accurately reproduce, are:

1. Mapping the system to high-mass hadronic states (strings or clusters)
2. Mapping strings to a discrete set of primary hadrons
3. Processing decays of the primary hadrons to secondary hadrons

Even though we are far from an exact calculation from the theory we are not completely blind in creating these models. Some basic constraints come from conservation laws we know are always valid, no matter the situation, for example Poincaré invariance, unitarity, causality etc. Moreover the lattice QCD technique can give quantitative results in certain aspects of the problem.

The phenomenon at hand is Strangeness Enhancement: very recently it has been observed in high-multiplicity pp collisions [6] without that being predicted by the most popular models. We will briefly go on about what is today's standard and possible new features.

1.3.1 Theoretical overview

The Strangeness Enhancement was first proposed in 1982 by J. Rafelski and B. Muller [16]. The basic idea behind this phenomenon is that the hot and dense medium would favor strange quark production, as the mass is not too large, gradually introducing more and more strangeness into the picture through the processes shown in Figure 1.8. After an equilibrium is reached, annihilation puts a stop to the strangeness proliferation, thus saturating to a limit density. Their first calculations suggested the predominant process is the production by gluons (Figure 1.8, Eq. 1.21); this gave way to a simplification of the rate equation. The rate per unit time and volume (A) for the elementary processes shown in Figure 1.8 is then:

$$A = \frac{\mathrm{d}N}{\mathrm{d}t\mathrm{d}^3x} \approx A_g = \frac{7}{3\pi^3}\alpha^2 M T^3 e^{-2M/T}\left(1 + \frac{51}{14}\frac{T}{M} + ...\right) \tag{1.21}$$

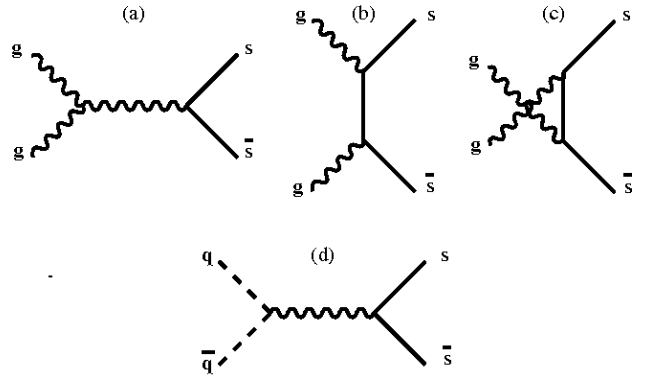

FIGURE 1.8: Lowest-order QCD diagrams for $s\bar{s}$ production: a-c) $gg \to s\bar{s}$ d) $q\bar{q} \to s\bar{s}$

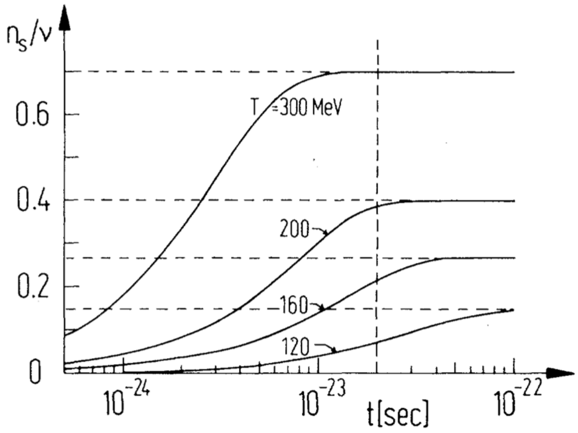

FIGURE 1.9: Time evolution of the relative strange-quark to baryon-number abundance in the plasma for various temperatures (M=150 MeV, $\alpha_s = 0.6$)

Given T is the temperature of the QGP, M is the mass of the quark and their ratio is roughly greater than 1. Further on taking into accounts the saturation by annihilation process, proportional to the square of the density itself, it is possible to evaluate the density function (Eq. 1.22).

$$\frac{dn_s}{dt} \approx A\Big[1 - \Big(\frac{n_s(t)}{n_s(\infty)}\Big)^2\Big] \qquad \tau = \frac{n_s(\infty)}{A}$$

$$n_s(t) = n_s(\infty)\tanh(t/\tau) \tag{1.22}$$

It can be useful to understand the mechanisms of particle production in laboratory collisions before going further on the Strangeness Enhancement; their first calculations yielded shapes like those in Figure 1.9.

In the following sections the phenomenological approaches to the soft Physics will be reviewed, as the perturbative strategy fails to give significant accordance to

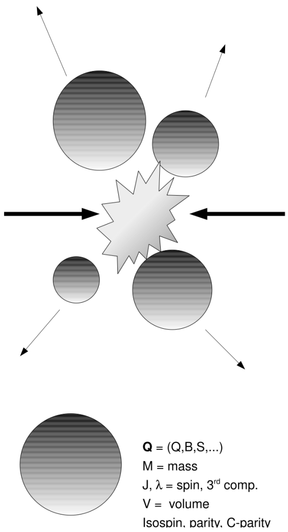

FIGURE 1.10: Schematic representation of the Hadron Gas Model

data in this context and the focus will be given to the mechanisms responsible to the Strangeness Enhancement.

Thermal Model

The Canonical Statistical (Thermal) model (CSM) is a phenomenological model that takes as an assumption that in heavy-ion collisions there is the creation of an equilibrated hadron gas, sign of QGP formation. Surprisingly the model describes well enough the behaviour of lighter (pp) collisions, even though it is highly non-trivial why such a small system would behave thermally. The idea is that the hadron gas divides in colourless droplets, clusters, fireballs at the hadronisation level (Figure 1.10) that carry various quantum numbers and Abelian charges. It is worth noting that the properties of such fireballs are defined as the complex result of the unfolding of the collision dynamic, whereas the hadron formation, as decay of such objects, is a purely statistical phenomenon. This concept is well summarized by the sentence:

> Every multi-hadronic state localized within the cluster and compatible with conservation laws is equally likely.

The defining characteristic of the Thermal Model is the finite size of the clusters, that implies the constant ratio between volume and mass of clusters when hadronisation takes place [17]. The partition function of the Grand Canonical ensemble is written as:

$$Z^{GC}(T,V,\mu_Q) = Tr[e^{-\beta(H-\sum_i \mu_{Q_i} Q_i)}], \tag{1.23}$$

where $\beta = 1/T$ is the inverse temperature, H is the Hamiltonian of the system, Q_i are the conserved charges, μ_{Q_i} the chemical potentials. From this, one can infer the average number $\langle N_i \rangle$ of particles i in volume V and temperature T, having strangeness S_i, baryonic number B_i, electric charge Q_i:

$$\langle N_i \rangle (T,\overline{\mu}) = \underbrace{\langle N_i \rangle_{th}(T,\overline{\mu})}_{\text{Thermal production}} + \underbrace{\sum_j \Gamma_{j\rightarrow i} \langle N_j \rangle_{th,R}(T,\overline{\mu})}_{\text{Decay production}} \tag{1.24}$$

Where the two parts highlighted are respectively the thermal production and the result of hadrons and resonances decays with a Γ branching ratio to the i species. The thermal production component can be expressed as:

$$\langle N_i \rangle_{th}(T, \overline{\mu}) = \frac{VTg_i}{2\pi^2} \sum_{k=1}^{\infty} \frac{(\pm 1)^{k+1}}{k^2} \lambda_i^k m_i^2 K_2(\frac{km_i}{T}) \tag{1.25}$$

Where g_i is the spin-isospin degeneracy factor, K_2 is the modified Bessel function, $\lambda_i(T, \overline{\mu}) = \exp[(1/T) \cdot (B_i \mu_B + S_i \mu_S + Q_i \mu_Q)]$ [18].

Coming back on the finite size of the cluster, as can be seen in Eq. 1.25, one must address the problem of evaluating it. The process connects the measured mean multiplicities to the differential production $\mathrm{d}N_j/\mathrm{d}y$ that is in turn connected to the differential volume $\mathrm{d}V/\mathrm{d}y$. This connects to the volume of the cluster V by a generic equation $V = k\mathrm{d}V/\mathrm{d}y$, for k>1. This choice is suggested by the hypothesis of a causal connection of fireballs which populate the longitudinal rapidity space. After some considerations for which we refer to [19], estimates for k in mid-rapidity range yield values of at about 3-6.

Summarizing, this is the so called "Vanilla CSM", based on the following scenario:

1. The full chemical equilibrium is established at the chemical freeze-out stage.

2. Constant chemical freeze-out temperature of T=155 MeV exists across all multiplicity bins, as suggested by the statistical model fits to the hadron yield data in most central Pb-Pb collisions.

3. The multiplicity dependence of various hadron yield ratios is driven by the canonical suppression only, i.e. by the changing value of Vc.

4. The correlation volume in rapidity is varied between V = $\mathrm{d}V/\mathrm{d}y$ and V = $6\mathrm{d}V/\mathrm{d}y$.

The results for this model are shown in Figure 1.11. Even though the description is approximately good for a number of ratios, others, most notably the ϕ/π ratio, are significantly out of trend.

To solve these discrepancies another approach in the CSM is possible. A first consideration might come from different chemical freeze-out temperatures across different multiplicities and different systems. Different T_{kin} values are found in pp collisions ($\approx$ 170 MeV) and in heavy-ion collisions ($\approx$ 100 MeV); the higher temperatures might hint at a shorter hadronisation phase. In the picture of an earlier strangeness chemical freeze-out a strangeness saturation factor γ_s is introduced:

$$\langle N_i \rangle_{th}(T, \overline{\mu}) = \frac{VTg_i}{2\pi^2} \sum_{k=1}^{\infty} \frac{(\pm 1)^{k+1}}{k^2} \lambda_i^k m_i^2 K_2(\frac{km_i}{T}) \times \gamma_s^{|s_k|}, \tag{1.26}$$

where s_k is the number of s-(anti)quark. This new conception is called the γ_sCSM, and provides a better description across all particle ratios (Fig. 1.12). This correction factor is leaning toward 1 in central ion collision, approaching the results of the Vanilla CSM.

Another approach, where γ_s is fixed to 1, was made varying the temperature of chemical freeze-out, yielding the results shown in Figure 1.13 [20].

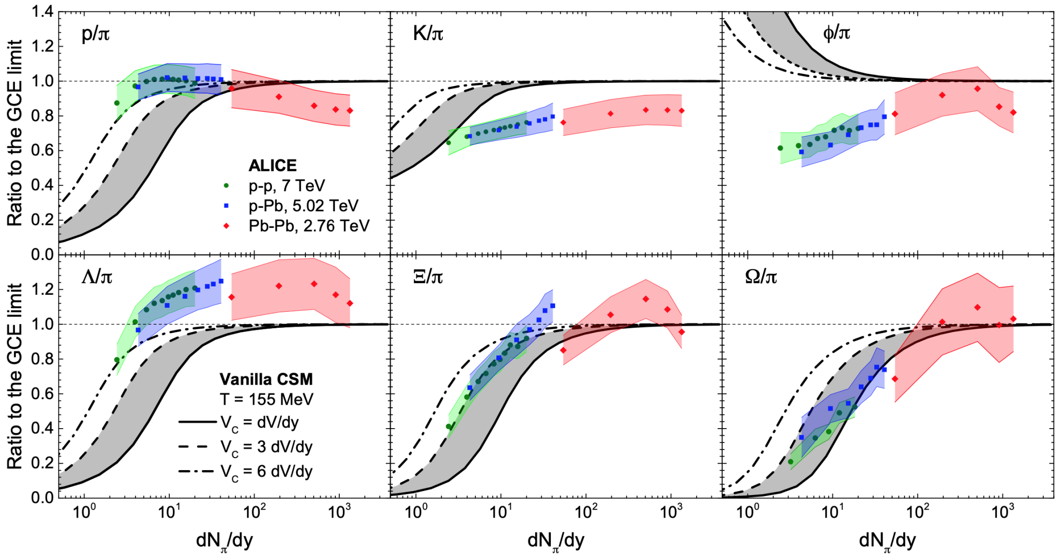

FIGURE 1.11: The ratios of various final hadron-to-pion yields are plotted versus the charged pion multiplicity as evaluated in the vanilla CSM with exact conservation of baryon number, electric charge, and strangeness. The green circles, blue squares, and red diamonds depict the corresponding ratios as measured by the ALICE Collaboration at the LHC in p-p (7 TeV), p-Pb (5.02 TeV), and Pb-Pb (2.76 TeV) collisions, respectively. Both the calculated results and the data are scaled by the grand-canonical limiting values as evaluated in the CSM at T = 155 MeV for μ_B = 0. [19]

Core-Corona Model

The Core-Corona model stipulates that the experimental results observed in heavy-ion collisions are due to the superimposition of the two components: the Core and the Corona [23]. That is, it distinguishes between nucleons fully participating in the collision and subsequent plasma formation, and peripheral nucleons scattering only once.

The assumption is that core nucleons will reach the equilibrium completely, whilst corona nucleons will essentially evolve as a pp collision. The superposition of the two components will depend on a geometrical function describing the dynamics of the event as in

$$M^i(N_{part}) = N_{part}\left[f(N_{core})\cdot M^i_{core} + (1 - f(N_{core}))\cdot M^i_{corona}\right] \tag{1.27}$$

being i the nuclear species. A graphical view of EPOS, a core-corona model, is shown in Figure 1.14. In Figure 1.15 [22] a simulation is performed to describe the recent results at the LHC on Strangeness Enhancement.

Lund String Model

The Lund String Fragmentation Model is based on a simple concept: the strong force creates a string between two quarks, that can eventually break generating new quarks on the loose ends.

The basic idea is that the linear strong potential between quarks will eventually store enough energy to produce a $q\bar{q}$ pair if initial quarks are provided with sufficient energy. Their interaction can be modeled by a string between them, and their motion

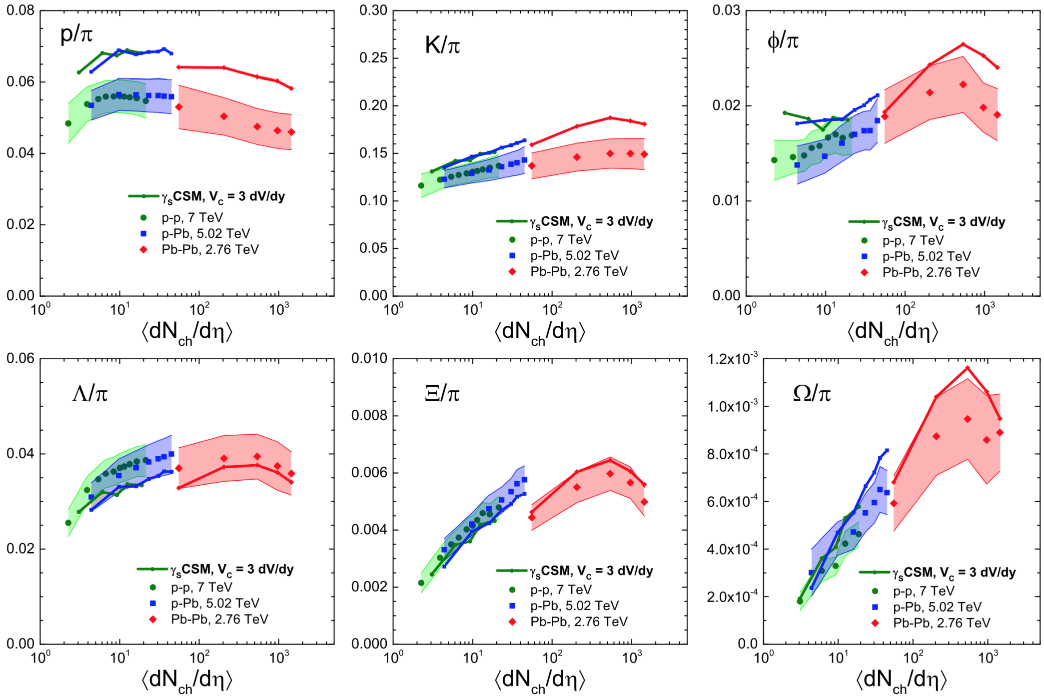

FIGURE 1.12: The dependence of yield ratios (a) $p/\pi, (b)K/\pi, (c)\phi/\pi, (d)\Lambda/\pi, (e)\Xi/\pi$, and (f) Ω/π on the charged particle multiplicity $\langle dN_{ch}/d\eta\rangle_{|\eta|<0.5}$, evaluated in the γ_sCSM with Vc = 3dV/dy for the thermal parameters extracted for each multiplicity bin through the 2 minimization. The green circles, blue squares, and red diamonds depict the corresponding ratios measured by the ALICE Collaboration in p-p (7 TeV), p-Pb (5.02 TeV), and Pb-Pb (2.76 TeV) collisions, respectively; the bands depict the corresponding experimental uncertainties. [19]

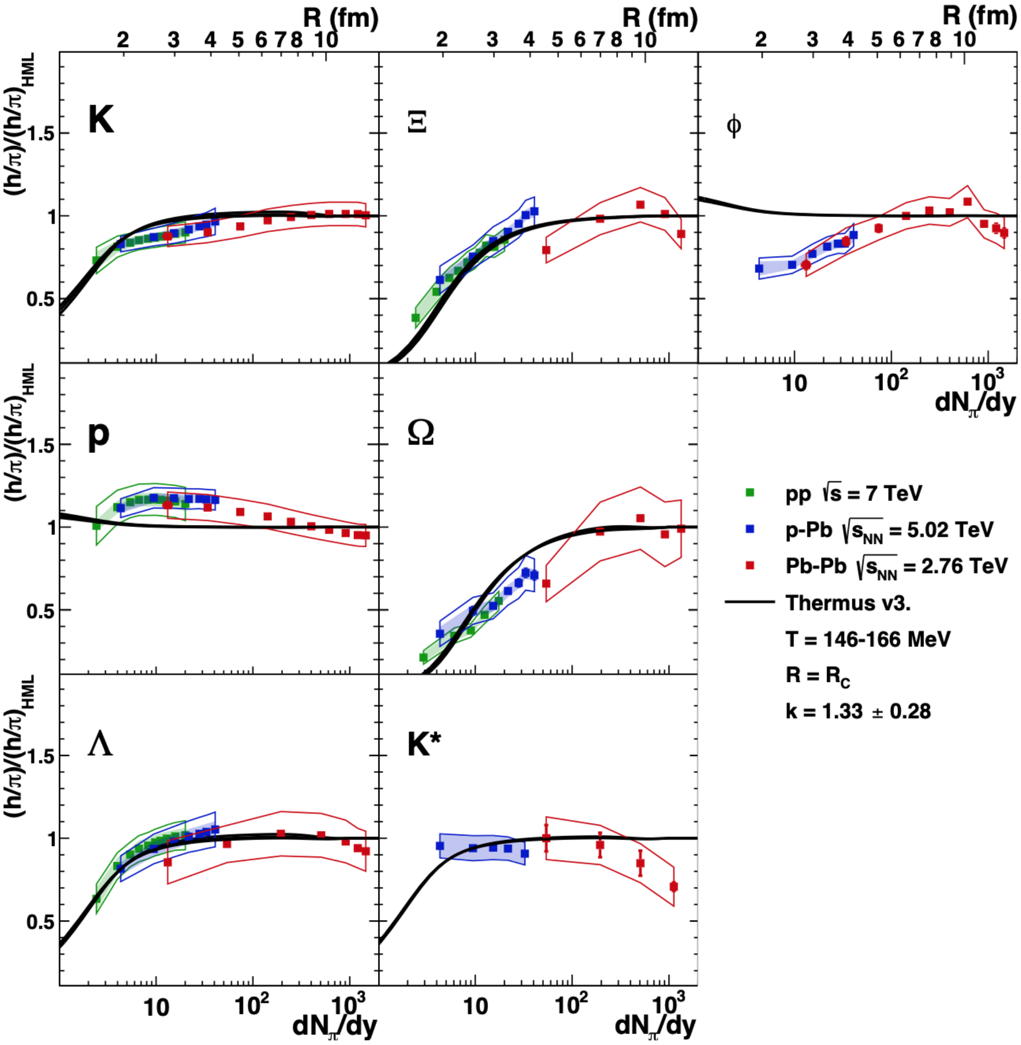

FIGURE 1.13: (colour online) Ratios of several particle species to pions as measured by the ALICE collaboration as a function of the midrapidity pion yields for pp, p-Pb and Pb-Pb colliding systems compared to the THERMUS strangeness canonical suppression model prediction (black line), in which only the system size is varied. All values except for the K^{0*} are normalised to the high multiplicity limit (see text for details). Note that $2 \cdot K^0_S$ are used for kaons in pp collisions, while $K^{\pm}$ are used for p-Pb and Pb-Pb collisions. The upper axis shows the radius R of the correlation volume V = R^3 which corresponds to the predicted particle ratios. The width of the model prediction line corresponds to a variation of the chemical freeze-out temperature between 146 MeV and 166 MeV. [20]

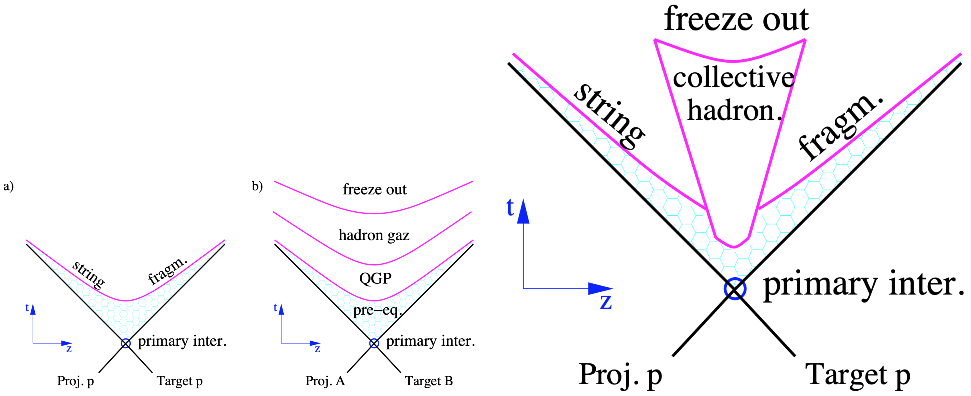

(A) (B)

FIGURE 1.14: Schematical representation [21] of (A) hadronisation in the Lund and Statistical Model (B) their combination in the Core-Corona Model

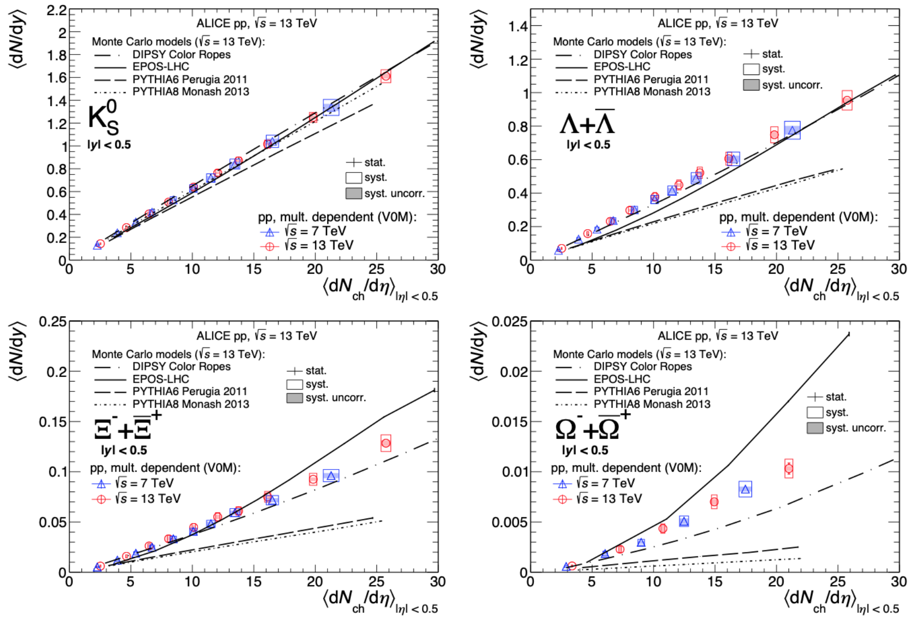

FIGURE 1.15: Integrated yields of K0$_S$, Λ, Ξ, and Ω as a function of ⟨dN$_{ch}$/dη⟩ in V0M multiplicity event classes at $\sqrt{s}$ = 7 and 13 TeV. Statistical and systematic uncertainties are shown by error bars and empty boxes, respectively. Shadowed boxes represent uncertainties uncorrelated across multiplicity. The results are compared to predictions from several Monte Carlo models, among them EPOS LHC, a Core-corona Model. [22]

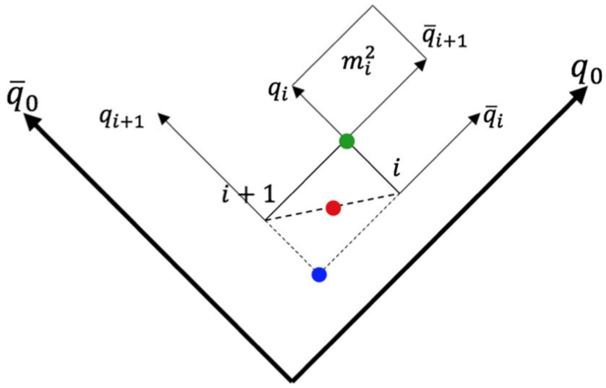

FIGURE 1.16: Hadron formation in a $q\bar{q}$ system. The blue, red and green dots represent the "early", "middle" and "late" definitions of hadron production points, respectively

as a back-and-forth along their connecting axis. In this simple terms, the further they drift apart, the more energy will be stored in the string and if the energy is high enough a new pair of $q\bar{q}$ will be produced, generating two particles [24]. This kind of approach can be described by a parametrisation of the strong potential as:

$$V_{QCD}(r) \approx -\frac{4}{3}\frac{\alpha_s}{r} + kr \tag{1.28}$$

Where $k \approx 1$ GeV/fm and r is the distance between a quark and an anti-quark, and kr is the dominant term.

As an example, if the oscillating quarks are $\overline{u}d$, a $s\overline{s}$ string breaking will result in the production of two kaons, if the string breaks twice and a double $s\overline{s}$ breaking occurs, two kaons and a ϕ meson are produced. In the case where the string breaks with a triple $s\overline{s}$ breaking, two kaons and two ϕ-mesons are produced. This mechanism is the key ingredient for the purpose of this thesis, as the inclusive production yield of ϕ mesons and the correlated production of ϕ-meson pairs are expected to be both linked to the more fundamental $s\overline{s}$ string breaking probability.

The key to this phenomenological approach is the assumption of *jet universality*, i.e. the idea that the fundamental hadronisation process and strength are unchanged from e^+e^- to pp collisions. After being tuned on the "clean" events at LEP, the LUND string fragmentation model is able to describe a large variety of hadronic collisions systems and energies. This is a direct consequence of the assumption that the string tension, responsible for the breaking probabilities, is constant. This means that all strings break in the same way, and e^+e^- annihilation provides a benchmark of a single string fragmentation to tune our parameters.

The fragmentation, illustrated in Figure 1.16, is a process where all breakings are causally disconnected; this gives the possibility to arbitrarily calculate the probability of fragmenting left to right or right to left as:

$$f(z) = N\frac{(1-z)^a}{z}e^{-bm^2/z} \tag{1.29}$$

where a, b are free parameters that need tuning to reflect the data. In the physical problem quarks need to escape the strong field and they do so by quantum tunneling. We supposed quarks were created in the same space-time point, if they were to have mass or transverse momentum they must be created virtual and then tunnel to become real particles. This effect can be encode in a suppression factor:

$$\lim_{m^2 \gg k/\pi} \mathrm{Prob}(m^2, p_T^2) \to \exp\Big(-\frac{\pi m_\perp^2}{k}\Big) = \exp\Big(-\frac{\pi m^2}{k}\Big)\exp\Big(-\frac{\pi p_\perp^2}{k}\Big), \tag{1.30}$$

That can be evaluated as $u\bar{u} : d\bar{d} : s\bar{s} : c\bar{c} \approx 1 : 1 : 0.3 : 10^{-11}$, which indicates that the soft hadronisation problem cannot be responsible for the production of heavy quarks, that are all formed in the initial hard scattering.

From equation 1.29 we can infer a piece of information about the multiplicity:

$$\frac{\mathrm{d}N}{\mathrm{d}y} \approx \sqrt{\frac{1+a}{bm^2}} \tag{1.31}$$

colour ropes colour ropes are formations arising from the interaction of colour charges in a limited area in transverse space acting coherently, assuming the total system is a colour singlet. Lattice calculation show that in such a situation if the endpoints charges correspond to a specific SU(3) multiplet, the tension of the rope is different than the string one [25].

To evaluate the differences introduced by this additional consideration we can see its effects on the parameters a and b, and on new parameters we will introduce to quantify modifications. All modified parameters will be indicated with a tilde ($\tilde{a}$, $\tilde{b}$,$\tilde{k}$,$\tilde{\rho}$, $\tilde{\xi}$) and h will represent the proportionality factor for the string tension enhancement.

$$k \mapsto \tilde{k} = hk \qquad \frac{n_s}{n_u} = \rho \mapsto \tilde{\rho} = \rho^{1/h} \qquad \frac{n_{di}}{n_q} = \xi \mapsto \tilde{\xi} = \tilde{\alpha}\beta\Big(\frac{\xi}{\alpha\beta}\Big)^{1/h} \tag{1.32}$$

n_s, n_u, n_{di}, n_q are respectively the number of s quarks, u quarks, di-quarks and quarks produced by the string; k is the string tension and h its enhancement w.r.t. nominal value, α, β are di-quark production parameters. Specifically α encloses all the parameters for all the different types of di-quark, whereas β is the popcorn fluctuation probability.

The most interesting in the Strangeness Enhancement picture is of course the ρ parameter. To get visually a sense of how a change in the string tension could affect these parameters we can turn to Figure 1.17.

Moreover, recalling the multiplicity in Equation 1.31 we can see how these changes affect it, lowering the raw yield by $\approx 5\%$ in high multiplicity pp, and up to $15-20\%$ in heavy-ion collisions. It should be noted that pp collisions are responsible for enhancement up to $h = 1.5$, the higher values are in the heavy collisions domain; $h = 1$ is the simple string tuned on the LEP data.

When evaluating the string tension enhancement it comes handy to understand that the tension in an isolated static rope is proportional to the quadratic Casimir operator C_2; furthermore in SU(3) the multiplets can be specified by two quantum numbers p, q. A specific state then corresponds to p coherent triplets (e.g. all red) and q coherent anti-triplets (e.g. all anti-green) with multiplicity $2N = (p+1)(q+1)(p+q+2)$. With this knowledge we can turn to how C_2 changes with the multiplet state:

$$\frac{C_2(\{p,q\})}{C_2(\{1,0\})} = \frac{1}{4}(p^2 + pq + q^2 + 3p + 3q) \tag{1.33}$$

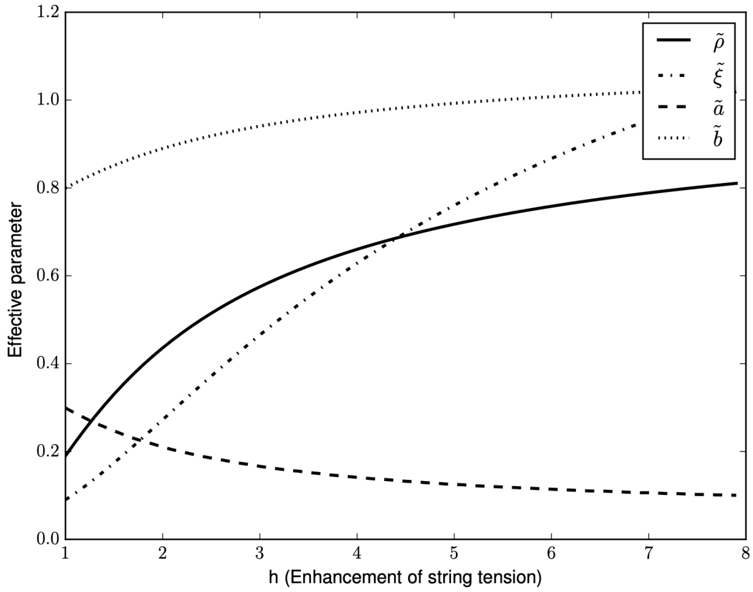

FIGURE 1.17: Effective parameters of the string model as a function of effective string tension. The parameters ρ and ξ control the strangeness content and baryonic content respectively, a and b are related to multiplicity. A modified string tension has a sizeable effect on ρ and ξ in particular. The range of h shown is much larger than relevant for pp collisions, which typically have h < 1.5. Larger values of h are, however, relevant for heavy-heavy-ion collisions. The values of the parameters for h = 1 comes from a tune to LEP data.

From this, we can infer how a change $\{p, q\} \mapsto \{p-1, q\}$ can affect the effective string tension ($\tilde{k}$):

$$\tilde{k} = \frac{2p+q+2}{4} k \tag{1.34}$$

Although this does not capture the full picture it can give a sense of how the tension might change. For a practical example we can turn to the simple case of two parallel strings in a {2,0}-state; their string tension during the first break-up would be $\tilde{k} = 3/2\ k$ whilst the second break-up would be happening at the usual string tension.

Without going into further detail a last picture of how the ropes can change the model predictions can be seen in Figure 1.18 (to compare with 1.4b)

1.3.2 Experimental overview

The history of Strangeness Enhancement starts, as mentioned before, from a paper back in 1982 [16] and in these some 40 years of life this signature has been proved to be a useful way to probe the QGP formation in heavy-ion collisions. Since its theoretical formulation, many experiments were devised to search for it, namely at CERN: an overview of these experiments can be seen in Figure 1.19 [4].

The first evidence of Strangeness Enhancement was found in the CERN-NA35 after being expanded in its experimental program for the search of strangeness. This opportunity came as the purposed experiment, CERN-NA36, was relying on new technologies which were proven to have some instrumental difficulties. The first of

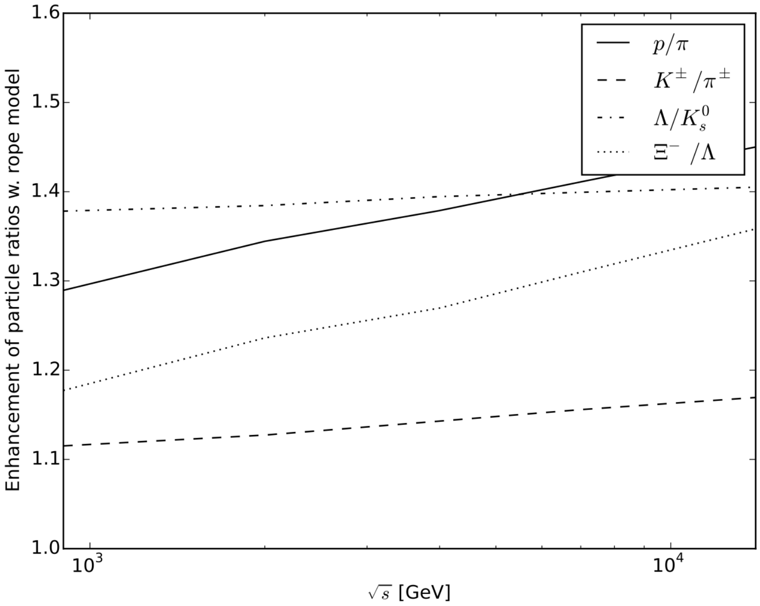

FIGURE 1.18: Enhancement of particle ratios of function of $\sqrt{s}$. Integrated ratios of $p^{\pm}$ and $K^{\pm}$ to $\pi^{\pm}$, $\Lambda\overline{\Lambda}$ to K_s^0 and Ξ^- to $\Lambda\overline{\Lambda}$ with the rope model (dipole approach) applied, normalised to the same ratio with ordinary string hadronisation. All particles with p_{T}> 200 MeV are included.

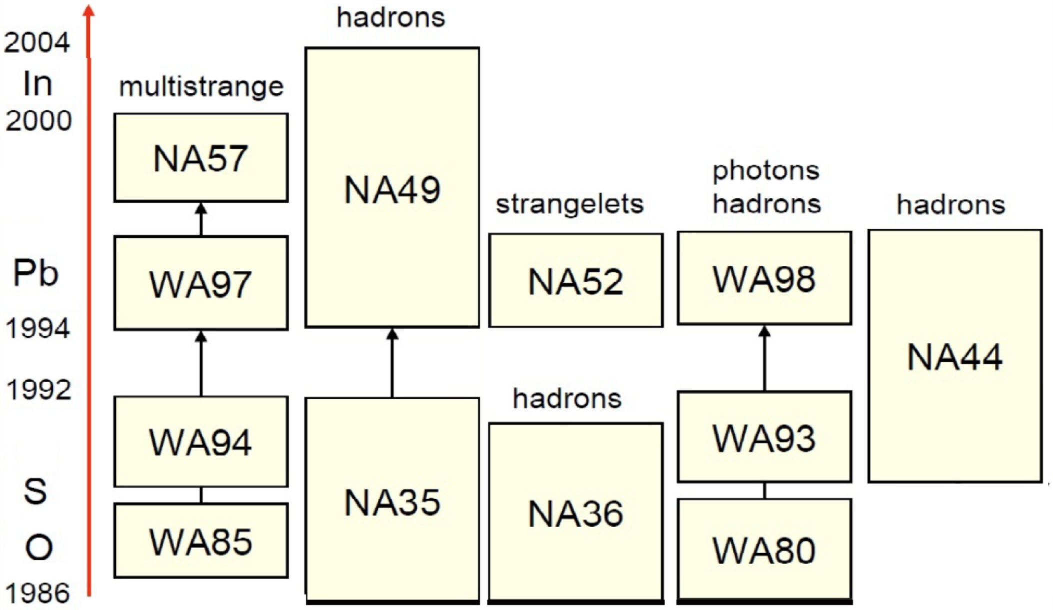

FIGURE 1.19: The multitude of CERN experiments measuring hadron production on line prior to the year 2000 QGP announcement

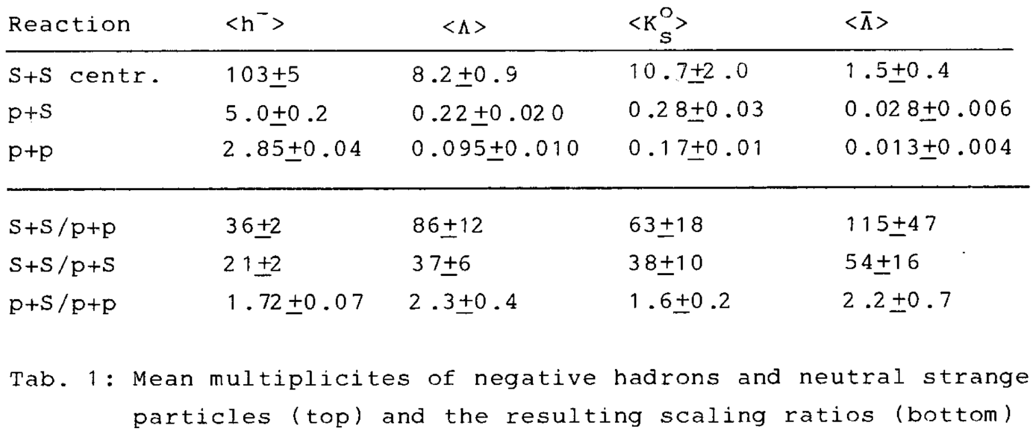

Reaction	$\langle h^{-} \rangle$	$\langle \Lambda \rangle$	$\langle K^{0}_{S} \rangle$	$\langle \bar{\Lambda} \rangle$
S+S centr.	103±5	8.2±0.9	10.7±2.0	1.5±0.4
p+S	5.0±0.2	0.22±0.020	0.28±0.03	0.028±0.006
p+p	2.85±0.04	0.095±0.010	0.17±0.01	0.013±0.004
S+S/p+p	36±2	86±12	63±18	115±47
S+S/p+S	21±2	37±6	38±10	54±16
p+S/p+p	1.72±0.07	2.3±0.4	1.6±0.2	2.2±0.7

Tab. 1: Mean multiplicites of negative hadrons and neutral strange particles (top) and the resulting scaling ratios (bottom)

FIGURE 1.20: First experimental results from the NA35 Collaboration [26]

the discoveries made by NA35 were reported at Quark Matter 1988, final and extended results were published in 1991 [26] (Figure 1.20). Even though their research pointed to Strangeness Enhancement, they operated Oxygen and Sulfur ions at 60 and 200 GeV/A, which was thought to be insufficient to produce QGP in the collision. Because of this the collaboration never explicitly claimed the findings as related to QGP formation. The consensus was that this primate would go to the RHIC experiments, which would have a ten fold energy scale.

Another dedicated experiment at CERN was the WA85: it made use of the repurposed Ω-spectrometer and used proton and Sulfur beams against a Tungsten target. They observed Strangeness Enhancement and, in spite of what was made in NA35, immediately hinted it might be proof of QGP formation. In 1991 the collaboration went as far as claiming the QGP discovery, although the general consensus was not reached.

The two groups continued to work on the Strangeness Enhancement, NA35/ NA49/ NA61 and WA85/ 94/ 97/ NA57. For example, the NA35 collaboration presented in 1995 results for the ratio $\overline{\Lambda}/\overline{p} \approx 1.4$, in accordance with the first predictions for QGP, while the WA85/94 focused on multi-strange baryon and anti-baryon ratios, such as $\overline{\Xi}/\overline{\Lambda}$. The Pb-Pb program following these experiments continued to strengthen the results in favor of the Strangeness Enhancement and other experiments made contemporarily were finding supportive data for the QGP formation hypothesis. This led to the CERN announcing the QGP discovery in 2000, although, once again, the general consensus was not settled on the claim, and many flaws were pointed out.

The NA61 Collaboration then focused on understanding the threshold for the Strangeness Enhancement phenomenon, after the claims of CERN. In this context a thorough study of the K^{+}/π^{+} ratio the Marek's horn was discovered (Fig. 1.21b). The interpretation for this feature was that a new mechanism of creation for strange pairs was activated. In particular it is believed that gluon production is starting above $\approx \sqrt{s_{NN}} = 7$ GeV. This new activation can come from the QGP generation, indicating that it can be made above such energies.

Combining the results from SPS and RHIC another item could be settled: canonical strangeness suppression. The ratio between $\Xi(ssq)/\phi(s\bar{s})$, two double strange particles, is an energy independent: this indicates that the data correlates the multi-strange production yields to the strangeness content of the hadron but not to the

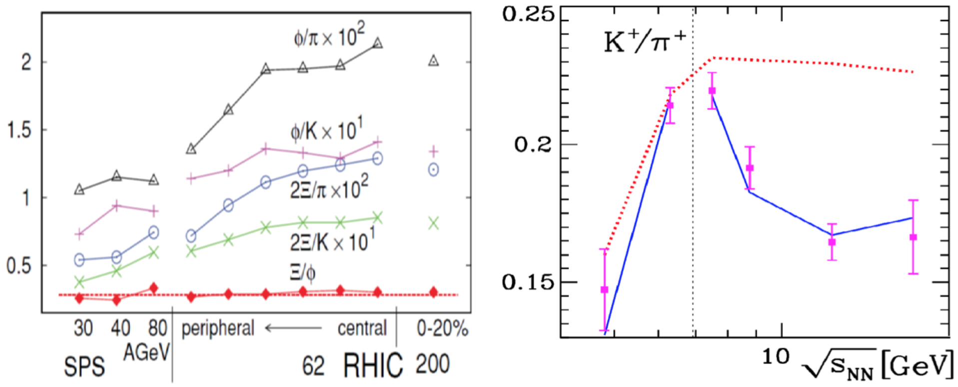

(A)

(B)

FIGURE 1.21: (colour online) Left: K^+/π^+-ratio; AGS (lowest $\sqrt{s_{NN}}$) and NA49-SPS energy range results are connected by the (blue) line indicating at the edges the theoretical fit result within chemical non-equilibrium model, the dotted line shows best chemical equilibrium result.
Right: Cost in fireball thermal energy of a strangeness pair, E/s as a function of CM collision energy $\sqrt{s_{NN}}$. 4π results (black) are estimates for RHIC, line guides the eye; RHIC domain (blue) shows (dE/dy)/(ds/dy)

strangeness quantum number. This is in contrast with the canonical suppression picture, a volume dependent model. Moreover, the universal value of the ratio is indicating that irrespective of how the fireball is formed there is no significant alteration in the final state of the yields of these double strange particles.

Recent results have confirmed that the Strangeness Enhancement is not restricted to heavy-ion collisions, but at sufficiently high energies it shows up in high multiplicity pp collisions [6] (Fig. 1.22a). The effect smoothly pours into the proton-ion and ion-heavy-ion collisions data (Fig. 1.22b) when considering the multiplicity of the event $\mathrm{d}N_{ch}/\mathrm{d}\eta$. The saturation at high multiplicity is a sign of complete thermal and chemical equilibrium of the formed QGP.

Some final thoughts on the matter are that the data clearly shows the onset of deconfinement at energies above $\approx \sqrt{s_{NN}} = 7\,\mathrm{GeV}$, and that the hadronisation of the QGP is solely dependent on the entropy content. The strangeness signature would then depend on the lifetime and/or volume of the fireball rather than on the collision system or energy. Across the experiments we have reviewed, up to LHC, strangeness in the QGP saturates and hadronises in nearly identical fashion, as shown by the ratios of particles, with absolute yields depending on the final geometric size.

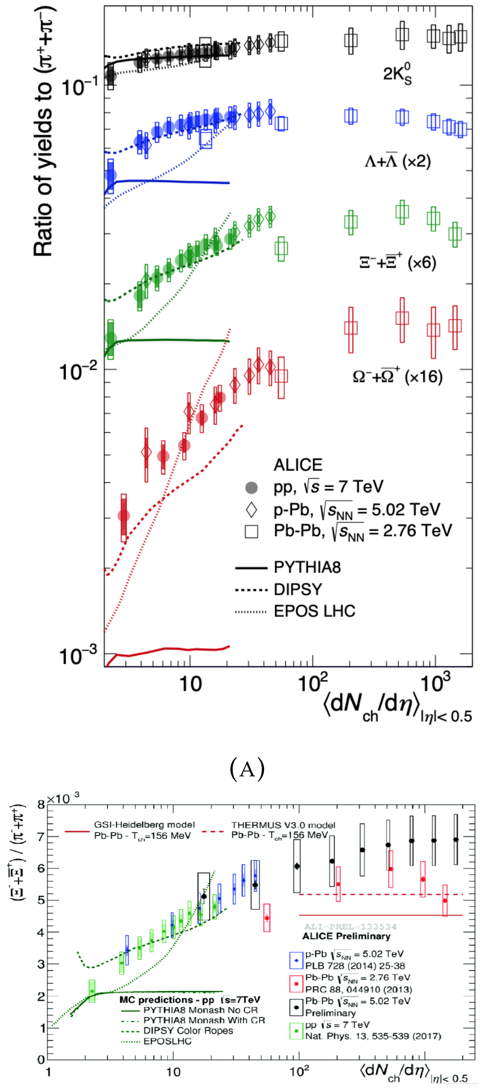

(A)

(B)

FIGURE 1.22: (A) Overview of results for strangeness signature of QGP from ALICE published Spring 2017 [6]. (B) The results of July 2017 SQM meeting, QCD Monte Carlo simulations are not able to reproduce the observed results (curves marked PYTHIA8, DIPSY, EPOS LHC)

Chapter 2

A Large Ion Collider Experiment

ALICE (A Large Ion Collider Experiment) is one of the four major experiments located on the Large Hadron Collider (LHC) ring at CERN (Figure 2.1). The ALICE Collaboration aims at studying the Physics of strongly interacting matter at high energy densities. At the energy densities reached in ultra relativistic collisions of heavy ions a new state of matter emerges: the Quark-Gluon Plasma (QGP) which is one of the main topics of research of the Collaboration [1].

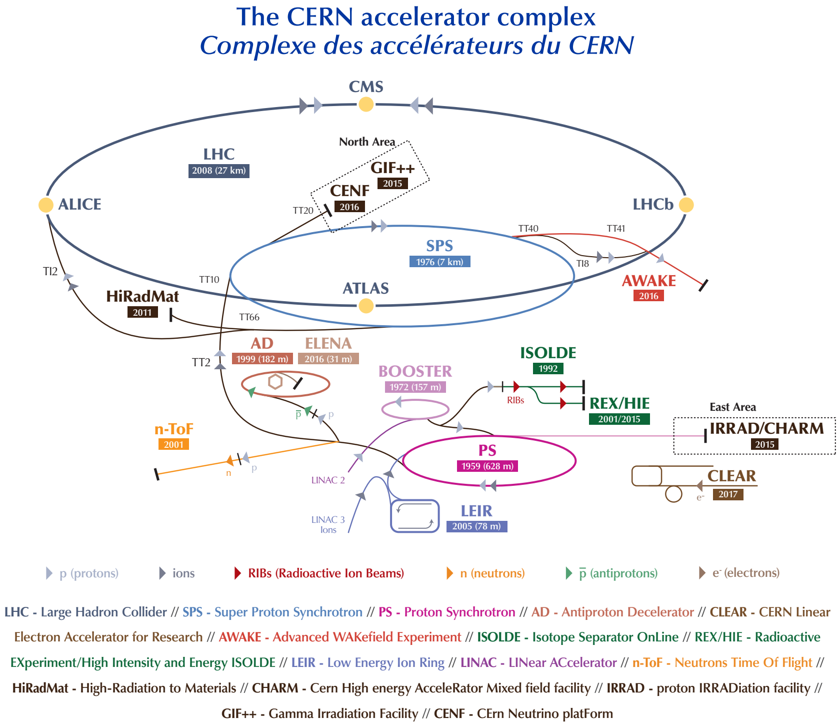

FIGURE 2.1: Schematic view of the CERN accelerator complex in 2018. Figure taken from [27].

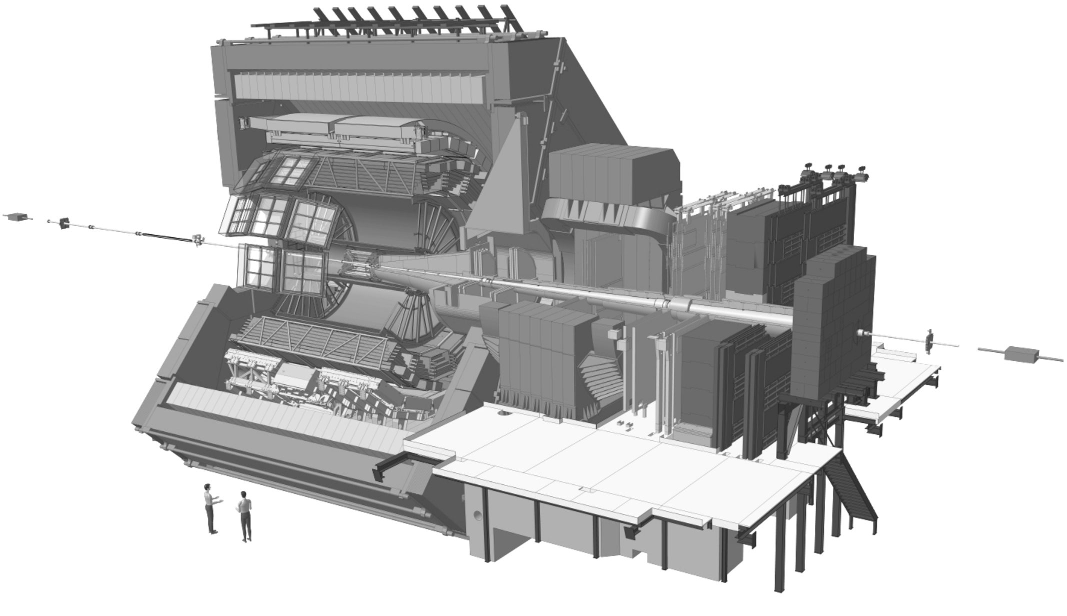

FIGURE 2.2: The ALICE detector structure.

In the following sections we will briefly overview the ALICE sub-detectors, with special emphasis on those that play a key role in the analysis presented in this thesis, such as the Time Of Flight Detector and the Time Projection Chamber. After that an overview of the ALICE tracking and Particle Identification techniques and performance will be carried out to explain the methodological choices made in the analysis.

2.1 ALICE Detectors

The ALICE experiment is a heavy-ion, general purpose detector and consequently consists in a large variety of sub-detectors devoted to specific tasks aimed at characterizing the events produced at the interaction point. Generally all sub-detectors are devoted to determine, to various degrees, the particle identity and its trajectory, but some are more focused on characterizing the event as a whole or to discern events based on the Physics involved.

The central barrel part of the experiment develops in a cylindrical structure around the beam pipe, centered at the nominal interaction point (Fig. 2.2). Overall, the experiment weighs around $10\,\mathrm{kt}$, occupying a volume of $16 \times 16 \times 26\,\mathrm{m}^3$. The cylindrical structure develops around the beam pipe, layering a set of sub-detectors covering the full azimuthal angle as a core multipurpose detection system, accompanied by more specific detectors, with limited acceptance; these are usually aimed at dedicated Physics. The experiment also extends with detectors located in the forward region, perpendicularly to the beam pipe. In this region lay the majority of detectors devoted to event characterization (event luminosity, pile-up, effective energy, etc.) and the Muon Spectrometer, devoted specifically to muon detection.

The central barrel is made, starting from the beam pipe, by the Inner Tracking System (ITS), devoted to measure the effective vertex position and particle tracking, the Time Projection Chamber (TPC), devoted to particle tracking and identification, the Transition Radiation Detector (TRD) and the Time Of Flight (TOF), both devoted

to particle identification. These sub-detectors cover the full azimuthal angle. All the central barrel detectors mentioned above are embedded in the L3 solenoidal magnet which has field of $0.5\,\mathrm{T}$, to bend charged particles and provide information on their momentum and charge. A mixture of multiple detectors share the subsequent outer region: the Electro-Magnetic Calorimeter (EMCal), Photon Spectrometer (PHOS) and the High-Momentum Particle Identification Detector (HMPID). The Forward regions host the Forward Muon Spectrometer (FMS) together with: T0, V0, Forward Multiplicity Detector (FMD), Photon Multiplicity Detector (PMD), Zero Degree Calorimeters (ZDCs). The Muon Spectrometer is equipped with its own dipole magnet, generating a field integral of B = $3\,\mathrm{T\,m}$.
This very complex setup manages to achieve excellent performance in the challenging environment of heavy ions collisions, both in precision measurements and particle identification. The next sections will be focused on each detector to describe their main features and uses. Even though the focus will be on the Run 1 and Run 2 equipment, used to record the data used in the analysis presented in this thesis, a brief overview of the main upgrades that ALICE is undergoing for the upcoming Run 3 will be given.

2.1.1 Inner Tracking System (ITS)

The Inner Tracking System is a key element of the experiment, providing the first pieces of information from the event and determining the effective interaction vertex with a resolution below $100\,\mu\mathrm{m}$. Together with the primary vertex, the ITS provides an excellent capability for the reconstruction for secondary vertices, as those from short-lived hadrons, such as hyperons, D and B hadrons. Even though the main tracking sub-detector is the TPC, the ITS proves useful to assess with enhanced precision the tracks found in the TPC and expanding the detection momentum range at the lower limit: in fact many material effects compromise the reconstruction of low momentum tracks, that are usually well recovered by the ITS. Moreover the combination of multiple detectors helps to reconstruct tracks that would be lost in dead regions of other detectors. For its privileged position, multiple tasks and tracking capabilities the ITS is a key detector for almost any analysis performed on ALICE data.

This system covers the pseudo-rapidity region spanning $-0.9 < \eta < 0.9$ and consists of six cylinders layered inside of one another. The first two layers, the Pixels, have been chosen to discern the tracks in the high multiplicity density that arises in the regions close to the beam pipe. The outer layers, where the tracks density decreases, use technology that gives information on the energy loss on top of position, thus allowing to perform a particle identification, especially for particles with low momentum. Given that low momentum tracks are dominated by multiple scattering effects, the material budget must be kept to a minimum, and it has been reduced to roughly $\approx 1\% X_0$ for each layer, giving a total of $\approx 8\% X_0$ for the whole system. Moreover, the outer cylinder is located as close as possible to the TPC, to create a continuum in the tracking.

Silicon Detectors (SPD-SDD-SSD) Silicon Pixel Detectors (SPD) are the detectors used in the two innermost layers of the ITS. They extend from $3.9\,\mathrm{cm}$ to $7.6\,\mathrm{cm}$ radially and cover $28.2\,\mathrm{cm}$ longitudinally. The main purpose of this detector is the determination of the primary vertex and of the impact parameter of secondary tracks from the decay of short-lived particles. Its operations have to work with a particle density as high as 50 per cm^2, that indicates the detector has to withstand a high dose,

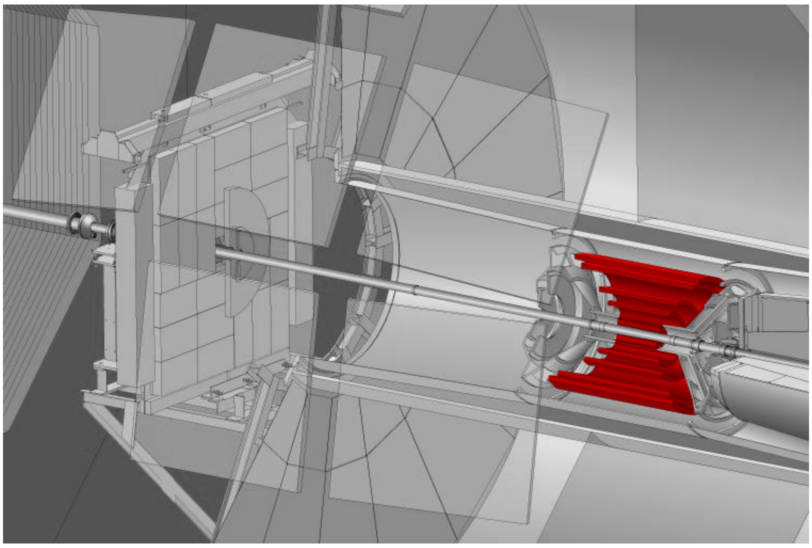

FIGURE 2.3: The ITS position inside the ALICE experiment, highlighted in red.

estimated for a 10y run in $2.7\,\mathrm{kGy}$. This detector has the greatest pseudo-rapidity coverage ($-1.98 < \eta < 1.98$) of the ITS sub-detectors to provide, together with the FMD, a multiplicity measurement over a large pseudo-rapidity range. Silicon Drift Detectors (SDD) are the detectors used in the two intermediate layers. They extend from $15.0\,\mathrm{cm}$ to $23.9\,\mathrm{cm}$ radially and cover up to $59.4\,\mathrm{cm}$ longitudinally. Silicon micro-Strip Detectors (SSD) are the detectors used in the two outermost layers. They extend from $38.0\,\mathrm{cm}$ to $43\,\mathrm{cm}$ radially, and cover up to $97.8\,\mathrm{cm}$ longitudinally. The last four layers give the possibility to read the analog output to determine the energy loss of the particle, giving leverage for particle identification within this system.

ITS Upgrade for Run 3 and 4 The upgraded Inner Tracking System (ITS2) will use the new silicon pixel detectors known as CMOS Monolithic Active Pixel Sensors (MAPS)[28]: the innovation comes from the integration of sensible volume with read-out electronics, that will be possible in a thin silicon sheet of roughly 50-$100\,\mathrm{\mu m}$. Such a thin detector allows to further reduce the material budget down to 0.3% in the inner layers and the flexibility of the structure reduces greatly the need of overlapping detectors to cover the full azimuthal angle. Another important achievement is the proximity to the beam pipe, down to $2.3\,\mathrm{cm}$ for the innermost cylinder, that will allow for more precise measurements of primary and secondary vertices.

2.1.2 Time Projection Chamber (TPC)

The Time Projection Chamber is the main tracking device of ALICE. Together with the ITS, it provides a way to achieve a good two-track separation, momentum measure and vertex determination. The acceptance for the TPC is $-0.9 < \eta < 0.9$ when combined with the outer detectors (ITS, TRD, TOF) and $-1.5 < \eta < 1.5$ when used stand-alone, and has a good p_T resolution in a wide range, from 0.1 GeV/c to 100 GeV/c.

The most stringent requirement for the TPC was to sustain the very high multiplicity in Pb-Pb central collisions, up to $\mathrm{dN}_{ch}/\mathrm{d}\eta = 8000$. Such a high multiplicity come at the cost of space charge distortions in the TPC drift volume and consequent loss of resolution on the tracks, that nevertheless can be partially recovered offline;

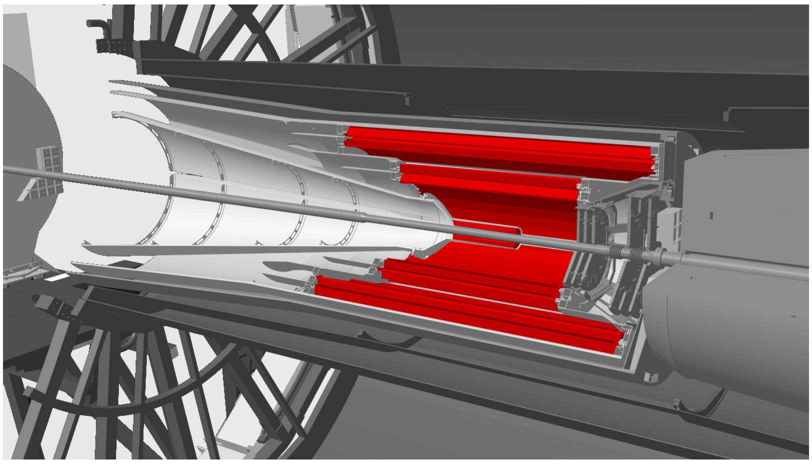

FIGURE 2.4: The ITS upgrade position inside the ALICE experiment, highlighted in red.

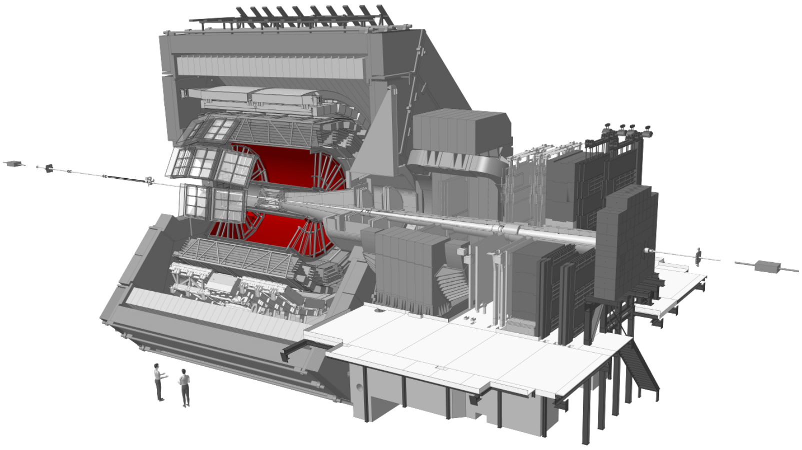

FIGURE 2.5: The TPC position inside the ALICE experiment, highlighted in red.

this is the main limit in Pb-Pb collisions. In pp collisions the experiment main constraint comes from the electrons drift time of $\approx 90\,\mu s$ ($v = 2.7\,\frac{cm}{\mu s}$) in the TPC, so that the pile-up of tracks reaches up to 60 pp events. Track distinction may be achieved by looking at the vertex the track points to.

TPC Upgrade for Run 3 and 4 The upgraded TPC will make use of Gas Electron Multiplier (GEM) Detectors for the read-out planes. GEM detectors are Micro-Pattern Gas Detectors (MPGD), and thus have an intrinsically low ion back-flow and their use will make the gating grid superfluous for the ion leakage control in the drift volume, thus allowing for a faster data acquisition and running with higher instantaneous luminosity.

2.1.3 Transition Radiation Detector (TRD)

The transition radiation detector's main purpose is to identify electrons with momenta higher than 1 GeV/c, which is the upper limit for identification by energy loss with the TPC. The identification of electrons depends on their discrimination against pions [29].

The principle of operation of the TRD is the Transition Radiation (TR), an electromagnetic radiation released as the result of the crossing of a charged particle through a separation plane between two materials having different dielectric constants. For the radiation to be detected the particle relativistic factor should be about $\gamma \approx$1000, making it hard for any particle except for $e^{\pm}$ to reach this threshold. The radiation is indeed always emitted when crossing the separation surface, but this threshold refers to an emission in an efficiently detectable spectrum. The detector is equipped with a radiator made of alternated foils of polypropylene fiber mats of $3.2\,\mathrm{cm}$ and Rohacell foam sheets of $0.8\,\mathrm{cm}$. The drift chamber to detect the TR is filled with a mixture of Xe/CO_2 (85%/15%).

2.1.4 Time of Flight Detector (TOF)

The Time Of Flight system main purpose is Particle identification. It is made of 1593 glass Multi-gap Resistive Plate Chamber (MRPC) detectors, each with a sensitive area of $7.4{\times}120\,\mathrm{cm}$. The TOF covers the pseudo-rapidity interval $-0.9 < \eta < 0.9$ and the full azimuthal angle, for a total active area of $141\,\mathrm{m}^2$. Each MRPC is segmented into 96 read-out pads of area $2.5{\times}3.5\,\mathrm{cm}^2$, for a total of over 150,000 channels [30].

The main purpose of this detector is the identification of low and intermediate momentum particles: it provides an excellent identification efficiency for π and K up to around 2.5 GeV/c and up to 4 GeV/c for the protons. In addition to its PID capabilities, the TOF system provides a dedicated trigger for cosmic rays and for J/Ψ production in ultra-peripheral heavy-ion collisions. The intrinsic particle detection efficiency is $\approx 99\%$, that must be coupled with geometrical acceptance and tracking capabilities of the ALICE experiment, which lowers the reconstruction efficiency to $\approx 80\%$ for p-Pb collisions. Because of this very favorable performance the analysis will make use of this detector for the identification of kaons. In Pb-Pb collisions, in the centrality range 0-70% the overall TOF resolution is $80\,\mathrm{ps}$ for pions with a momentum around 1 GeV/c. At the start of the Run 2 the data collected was used to make a refined channel by channel calibration, rather than the previous 8-channel group calibration, being able to reach an overall resolution of $\approx$60 ps The timing information is key, as every enhancement of the Time Of Flight resolution for a particle allows to extend the momentum range where the separation power between species is possible (usually at the level of 3 or 5 σ). The measurement if the start time can be performed with the T0 detector and/or with the TOF detector itself; in the latter case using a combination of all arrival times of the tracks, minimizing the χ^2 testing different combinations of the mass hypothesis. This process is performed if at least three particles reach the TOF; if more than 30 reach it the resolution on the event timing can be as low as $30\,\mathrm{ps}$. This method proves useful when the T0 start signal is missing, if neither are available the time from the LHC internal clock is used.

2.1.5 High-Momentum Particle Identification Detector (HMPID)

The High-Momentum Particle Identification Detector's main purpose is particle identification exploiting the emission of Cherenkov radiation.

The principle of operation is based on a proximity focusing Ring Imaging Cherenkov (RICH), using C_6F_{14} as a radiator. The proximity focusing means that the cone of light is projected onto a "screen" (i.e. detector plane) from a thin radiator, after a small gap, called the proximity gap. This configuration differs from the focusing

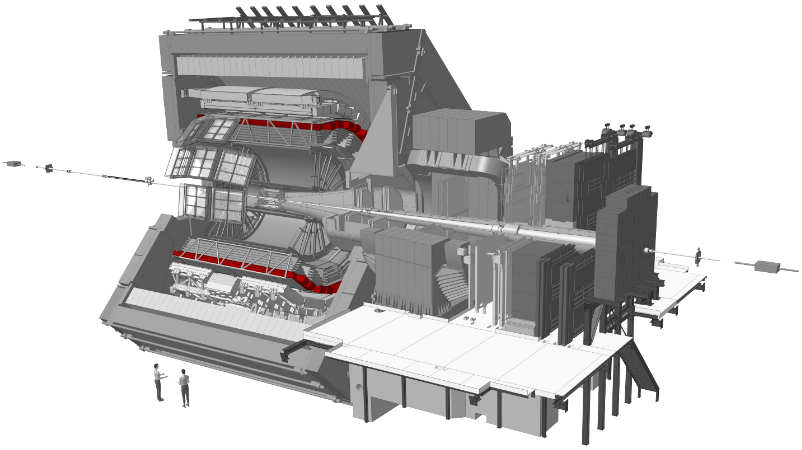

FIGURE 2.6: The TOF position inside the ALICE experiment, highlighted in red.

RICH configuration where the radiation is reflected by spherical mirrors before being collected by the photo-detector. The radiation photons are detected using a CsI thin layer deposited onto the pad cathode of a Multi Wire Proportional Chamber (MWPC) [31]. The detector provides a 3σ separation power, for π/K up to $p_T = 3$ Gev/c and for K/p,$\overline{\text{p}}$ up to $p_T = 5$ Gev/c. The PID process requires informations on the track extrapolated in the central barrel. When coupled with the other central barrel detectors, the HMPID data has provided inclusive charged hadron spectra for π,K in the range 1.5 Gev/c < p_T < 4 Gev/c, for p,$\overline{\text{p}}$ in the range 1.5 Gev/c < p_T < 6 Gev/c, for deuteron in the range 3 Gev/c < p_T < 8 Gev/c for the most central Pb-Pb collisions.

2.1.6 Photon Spectrometer (PHOS)

The Photon Spectrometer is designed to measure spectra, collective flow, correlations of direct photons and of neutral mesons in ultra-relativistic nuclear collisions at LHC energies; having excellent performance for the low energy photons coming from the initial phase of QGP formation and the high momentum photons, decay products of high p_T π_0 [32]. It is a homogeneous high granularity calorimeter, meaning that all the material is both active and passive: whilst it stops the particle to acquire all of its energy, the material also detects and measures this energy loss via the produced scintillation light. To further enhance the scintillation efficiency and yield, the detector is cooled at a constant temperature of $-25\,^{\circ}\mathrm{C}$. At this temperature the light yield is increased by a factor of 3 with respect to room temperature together with a reduction of the electronic noise in the photon detector, thus improving the resolution. It consists of 17920 detection channels made from $\mathrm{PbWO_4}$ (PWO) as little as $2.2 \times 2.2 \times 18\,\mathrm{cm}^3$. It is one of the sub-detectors not covering the full azimuthal angle, spanning $250^{\circ} < \phi < 320^{\circ}$ and $-0.12 < \eta < 0.12$. The detector consisted of 3 and 1/2 modules[1], with the plan to expand its acceptance to a cover 5 and 1/2 modules for Run 3 operations.

---

[1] A module is a 1/5 of a sector, that is 1/18 of the cylindrical space-frame supporting the experiment detectors, meaning it is equal to $\approx 20^{\circ}$ coverage in azimuthal angle, and ≈ 0.35 in pseudo rapidity coverage

2.1.7 Electro-Magnetic Calorimeter (EMCal)

The Electro-Magnetic Calorimeter is dedicated to the measurements of electrons from heavy flavor decays and the electromagnetic component of jets, spectra and correlations of isolated direct photons and spectra of neutral mesons [32]. It is a sampling calorimeter, meaning it layers active material on top of passive material: whilst it stops the particle to deplete all of its energy in the passive material (foils of Pb $\approx 1.44\,\mathrm{mm}$), the active material (foils of scintillator $\approx 1.76\,\mathrm{mm}$) detects and measures the energy loss with scintillation light. It consists of 12,288 towers pointing to the interaction vertex, resulting in each tower covering roughly 2°in η and 5°in ϕ. It is one of the sub-detectors not covering the full azimuthal angle, spanning $80^\circ < \phi < 180^\circ$ and $-0.12 < \eta < 0.12$.

2.1.8 Forward Muon Spectrometer

The main purpose of the Forward Muon Spectrometer is the study of vector meson production through their decays in $\mu^+\mu^-$ and of muons from decays of heavy-flavor hadrons and W$^\pm$ [33].

The principle of operation is the tracking of muons in a forward region (Fig. 2.7). The detector starts with a block of absorber made of concrete and carbon, to minimize multiple scattering and energy loss of the incoming muons while all the same filtering all particles except muons, to clean the signal. The detector, positioned in the forward region, is also subject to possible background from the beam pipe, which is coated in tungsten, lead and stainless steel to shield it, either for particles emitted in the collision or showers produced in the shield. After the shield there are 5 stations of high-granularity tracking systems, each station having 2 detection planes of cathode pad chambers providing a resolution greater than $100\,\mathrm{mm}$. The 5 stations are set-up to be 2 before, 2 after, and 1 inside a dipole magnet, positioned about $7\,\mathrm{m}$ from the interaction vertex, generating an integrated field of B = $3\,\mathrm{T\,m}$. After the tracking system, another filter block is placed followed by 4 planes of RPCs (Resistive plate chambers), divided in two stations, forming the Trigger system for the decay of heavy quark resonances. In fact the second filter is to stop low momentum muons coming from lighter particle decays.

This detector covers a pseudo-rapidity region of $-4.0 < \eta < 2.5$ and provides a good acceptance for J/Ψ detection down to $p_T = 0$, with a low occupancy even in central Pb-Pb collisions of just 2%. After unfolding the charge clusters in the tracking system using the Maximum Likelihood Expectation Maximization (MLEM), a tracking algorithm based on the Kalman filter reconstruct the trajectories of the muons, that are then extrapolated to the reconstructed vertex to account for multiple scattering and energy loss in the shields. To further improve the purity of the sample spatial cuts are applied to reject fake tracks, notably a pseudo-rapidity cut outside the acceptance range $-4.0 < \eta < 2.5$ and geometrical acceptance range at the absorber entrance ($17.6\,\mathrm{cm}$ < R_{abs} < $89\,\mathrm{cm}$).

2.1.9 Other Forward Detectors

The other forward detectors are devoted to determine general information on the event, such as centrality for heavy-ions collisions, timing of the interaction to be used by the TOF, etc. They are also employed to perform measurements of the luminosity.

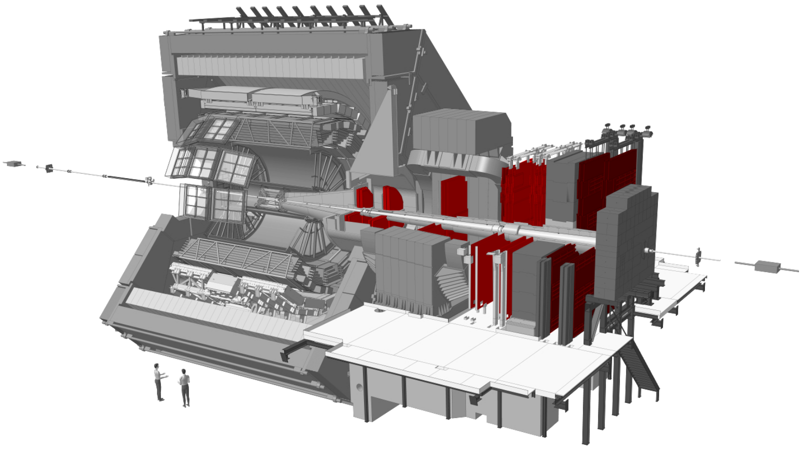

FIGURE 2.7: The Forward Muon Spectrometer position inside the ALICE experiment, highlighted in red.

V0 The detector consists in quartz scintillator counters, divided in two groups: V0A and V0C. The two detectors are set as close to the beam pipe as possible, one in proximity of the nominal interaction point at a distance of $90\,\mathrm{cm}$ (V0C) and the other outside the central barrel, at a distance of $340\,\mathrm{cm}$ (V0A) in the opposite direction. They both have the same dimensions but given they are located asymmetrically from the interaction point they cover different pseudo-rapidity ranges: V0A covers $2.8 < \eta < 5.1$, whilst V0C covers $-3.7 < \eta < -1.7$.

Their main purpose is to evaluate the multiplicity of the event and to generate a trigger on pp and heavy-ions collisions, in the latter case giving also information on the centrality of the event. During normal operations the detectors are run in AND mode and provide multiple triggers: Minimum Bias Trigger (MB), Multiplicity Trigger (MT), semi-Central Trigger (CT1) and Central Trigger (CT2). Moreover a Minimum Bias p-Gas Trigger (PG) can be used to reject interactions of the beam with the residual gas in the vacuum pipe.

T0 The detector consists in Cherenkov counters coupled with photo-multipliers, divided in two groups: T0A and T0C. The two detectors are set close to the beam pipe, one in proximity of the nominal interaction point at a distance of $72.2\,\mathrm{cm}$ (T0C) and the other outside the central barrel, at a distance of $375\,\mathrm{cm}$ (T0A) in the opposite direction. Their dimension is a little less than $40\,\mathrm{cm}^2$. T0A covers $4.61 < \eta < 4.92$, whilst T0C covers $-3.28 < \eta < -2.97$ in pseudo-rapidity.

Their main purpose is to give timing information on the event, setting the t_0, the real time of collision, for the TOF detector with a precision of $\approx 20\,\mathrm{ps}$ for heavy-ion collisions and $\approx 40\,\mathrm{ps}$ for pp collisions. The T0 detectors can also measure the position of the vertex along the beam axis with a $1.5\,\mathrm{cm}$ precision. Their efficiency is 40% for minimum bias pp collisions, combining a 50% and 59% single efficiency, that scales up to roughly 100% for central heavy-ion collisions thanks to the higher multiplicities.

FMD The Forward Multiplicity Detector is a silicon strip detector with 51,200 strips arranged in 5 rings, covering the range $3.4 < \eta < 5.1$. It is placed around the beam pipe at small angles to extend the acceptance of ALICE into the forward regions for charged particle multiplicity measurements. Combined with the SPD, they provide continuous coverage for this kind of measurements.

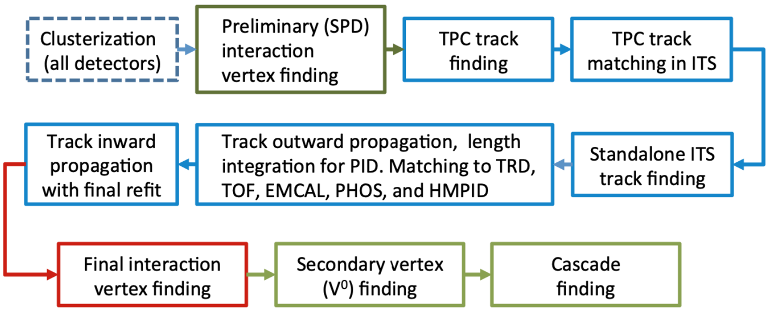

FIGURE 2.8: Event reconstruction flow. [1]

PMD The Photon Multiplicity Detector is a particle shower detector which measures the multiplicity and spatial distribution of photons produced in the collisions. It uses as a first layer a veto detector to reject charged particles. Photons pass through a converter, initiating an electromagnetic shower in a second detector layer where they produce large signals on several cells of its sensitive volume. Hadrons on the other hand normally affect only one cell and produce a signal representing minimum-ionizing particles.

ZDC The ZDCs are calorimeters which detect the energy of the spectator nucleons, i.e. the nucleons that do not interact in the heavy-ion collision, in order to determine the overlap region of the two colliding nuclei. It is composed of four calorimeters, two to detect spectator protons (ZP) and two to detect neutrons (ZN). They are located 115 meters away from the interaction point on both sides, along the beam line. The ZN is placed at zero degree with respect to the LHC beam axis, between the two beam pipes. The ZP is positioned externally to the outgoing beam pipe. The spectator protons are separated from the ion beams by the optics of the LHC. The ZDCs are "spaghetti calorimeters", made by a stack of heavy metal plates grooved to allocate a matrix of quartz fibers. Their principle of operation is based on the detection of Cherenkov light produced by the charged particles of the shower in the fibers.

2.2 Central Barrel Tracking

Tracking is the process by which tracks and vertices (primary and secondary) are reconstructed to be used as particle trajectories with physically relevant attributes such as charge, momentum, etc. Firstly, data from detectors are separately clustered, associating positions, signal amplitudes, signal times, etc., with their errors.

2.2.1 Preliminary Interaction Vertex

Preliminary Vertex finding uses the first two layers (SPD) of ITS. The two clusters in the layers are combined to form "tracklets", that are used as seeds that point toward a vertex candidate, the candidate with most convergent tracklets is taken as preliminary vertex.

When dealing with pp collisions with pile-up, subsequent searches are made, excluding tracklets pointing to established vertices up to when all tracklets are associated. When multiplicity is too low to have a sufficient resolution, and thus no vertex is found, a 1-dimensional search for a peak in z-distribution of the points of closest approach (PCA) to the nominal beam axis is made.

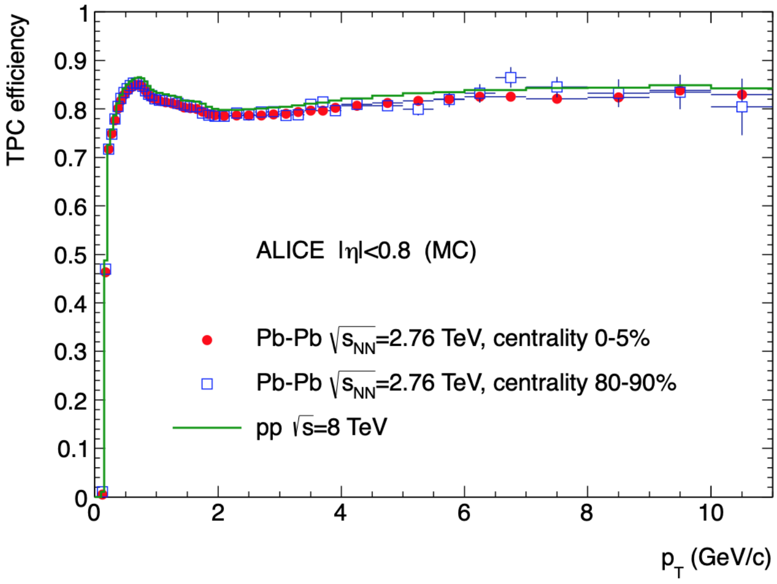

FIGURE 2.9: TPC track finding efficiency for primary particles in pp and Pb-Pb collisions (simulation). The efficiency does not depend on the detector occupancy. [1]

2.2.2 Track reconstruction

The mechanism follows a inward-outward-inward scheme.

The first step starts at the outer boundary of the TPC, where tracks are expected to be more resolved as the track density is lower. In the TPC there are 159 tangential pad rows, giving a track in principle the ability to leave as many clusters. The track seeds are first generated with two TPC clusters and the vertex. The mechanism then propagates inward, adding to the track the closest cluster (i.e. in trajectory) or none if the available ones are too far away (there is a cut on the distance from the track a cluster can have), without requiring a cluster to be uniquely used in a track. This makes it possible that the same track be reconstructed more than once: this problem is solved by an algorithm that checks overlap of tracks (25% to 50% same clusters used) and sort them by quality, discarding all but the the first. Only those tracks that have at least 20 clusters (out of maximum 159 possible) and that miss no more than 50% of the clusters expected for a given track position are accepted Passing these cuts implies the tracks are propagated further to the ITS. At this stage a first PID is performed based on the specific energy loss and a mass hypothesis is assigned to the track.

Continuing in the ITS, the propagations of the TPC tracks are used as seeds, updated at each layer with all clusters within a proximity range, saving each new fit as a new seed. If the track misses an expected hit on a layer, it is penalized on the χ^2, (the reduced χ^2) used to determine the track goodness. Once all the seeds have been found, a procedure similar to that performed on the TPC is carried-out, firstly constraining on the preliminary vertex, secondly loosing this requirement. All the candidate tracks are sorted by quality, discarding all but the first, except when two different tracks share a cluster. In this case the resolution of this conflict is performed by searching for good alternatives among other candidates: if the conflict cannot be resolved, the tracks are flagged as possibly mismatched. The final tracks are added to the TPC tracks in the reconstructed event. The efficiency of prolongation in the ITS for a track depends on the number of hits it has on the ITS itself: if only one

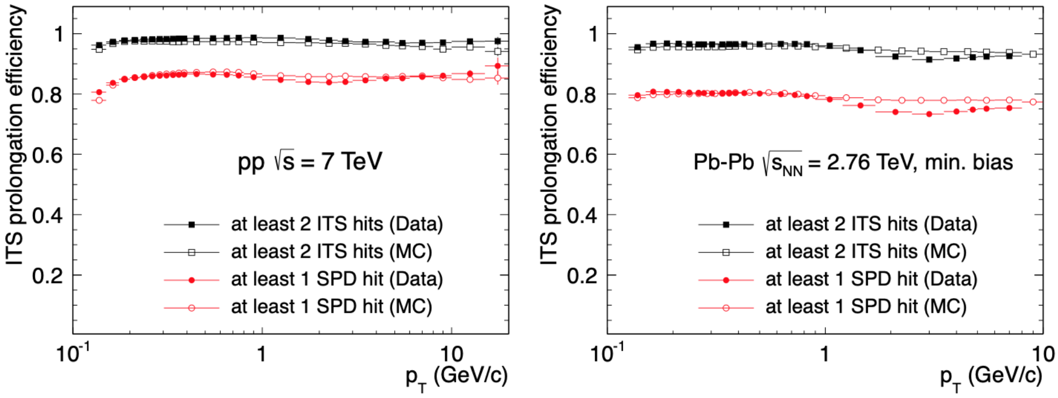

FIGURE 2.10: ITS-TPC matching efficiency vs. p_T for data and Monte Carlo for pp (left) and Pb-Pb (right) collisions [1].

hit is recorded a high (≈80%) efficiency is achieved, whereas if two hits are present, the efficiency is approaching unity at ≈95%. This efficiency slightly worsen in Pb-Pb collisions, as can be seen in Figure 2.10

One aspect to consider is the fall of reconstruction efficiency in the TPC for low transverse momentum (Fig. 2.9). The cut-off value is around 200 MeV/c for pions and 400 MeV/c for protons, and is caused by energy loss and multiple scattering in the detector material together with the bending of the magnetic field. This means a stand-alone ITS search for tracks is performed with those clusters not used to prolongate TPC tracks and account for these missing particles. The seeds are made using the vertex and the clusters of the first three layers, propagated in a similar fashion as for the TPC prolongation track searching. This procedure is able to find tracks down to 80 MeV/c transverse momentum.

Once the ITS propagation is finished, all tracks are propagated up to their PCA to the preliminary vertex. From there the tracks are re-fitted using a Kalman filter in the outward direction using the clusters that were assigned to it. During this outward path all track properties are updated at each step, such as track integrated length and expected time of flight for each particle species for use in the TOF detector for PID. The tracks are then propagated out of the TPC to the TOF, TRD, EMCal, PHOS, HMPID and an attempt to match their signals is made. This additional information are not used to update track information but is stored for PID purposes. Subsequently, a new fit is made starting from the outer radius of the TPC, determining the track's position, direction, inverse curvature, and its associated covariance matrix. This ends the procedure to find and fit the tracks coming from the primary vertex. To suppress the presence of secondary tracks a cut on the distance of closest approach (DCA) of the track to the interaction vertex is made. The DCA is the distance between the interaction point and the PCA. This cut can greatly improve the already good primary tracks identification efficiency: not asking for a tight DCA, ≈93% efficiency is achieved, after the asking for it, a ≈98% efficiency is achieved, as is seen in Figure 2.11.

The resolution of the measured momentum of a given particle is extracted form the covariance matrix of the track. As mentioned before, tracks can be reconstructed using the TPC stand-alone or combining it with the ITS. In ALICE this resolution is expressed as the resolution on the inverse transverse momentum, as:

$$\frac{\sigma_{p_{\mathrm{T}}}}{p_{\mathrm{T}}} = p_{\mathrm{T}}\sigma_{1/p_{\mathrm{T}}} \tag{2.1}$$

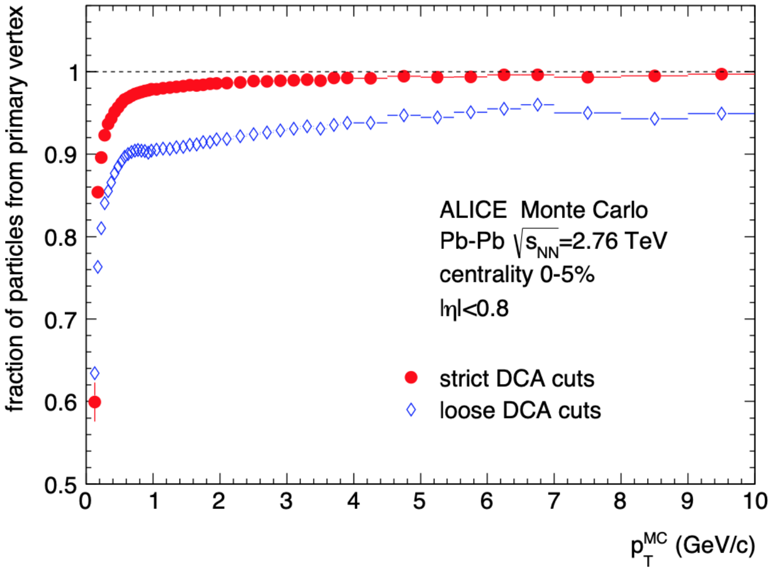

FIGURE 2.11: Fraction of reconstructed tracks coming from the primary interaction vertex. Two sets of cuts on the track distance of closest approach (d_0) to the primary vertex are shown: "loose" with $|d_{0,z}| < 3\,\mathrm{cm}$, $d_{0,xy} < 3\,\mathrm{cm}$ and "strict" with $|d_{0,z}| < 2\,\mathrm{cm}$, $d_{0,xy} <$ (0.0182 + 0.0350 GeV/c p_T) cm.[1]

The performance of the ALICE apparatus in terms of inverse transverse momentum in various configurations is shown in Figure 2.12. A clear improvement is obtained by constraining the tracks to the vertex, and by extending the TPC tracks to the ITS. On top of this, a deterioration of performance of $\approx 10 - 15\%$ should be expected in central heavy-ion collisions due to cluster overlap and fake clusters in tracks. Even thought the best configuration comprehend the ITS measurements, its acceptance has been reduced to $\approx 25\%$ for the years 2010/11 due to the inactivity of certain areas of the two innermost layers. A good approximation for its performance is provided by the TPC standalone constraining to the vertex up to 10 GeV/c, with a significant worsening at higher momenta.

2.2.3 Final primary and secondary vertices finding

The final primary vertex is found using fully reconstructed tracks in TPC and ITS, making a first selection to eliminate outliers and weighting the track contributions to further prevent smearing from any remaining outliers. If the event has low multiplicity the nominal vertex position is added to the fit.

After the primary vertex is pinned to its final position and all possible tracks are found, the search for secondary vertices starts. Secondary vertices are the spatial points were short-lived particles decay producing either a deflection of the ongoing track (decay in one charged and neutral particles), a split of the ongoing track into multiple tracks (decay of a charged particle in charged and neutral particles) or the apparition of multiple tracks (decay of a neutral particle into charged ones). Firstly a pool of possible decay products is determined requiring a DCA to the vertex to be over a threshold ($0.5\,\mathrm{mm}$ in pp and $1\,\mathrm{mm}$ in Pb-Pb collisions), then secondary vertices candidates (V∅) are chosen coupling unlike-sign pairs of tracks, determining their mutual PCA. This starting set of candidates is then subjected to multiple cuts: (a) The distance between the tracks and the V∅ candidate must be below $1.5\,\mathrm{cm}$; (b)

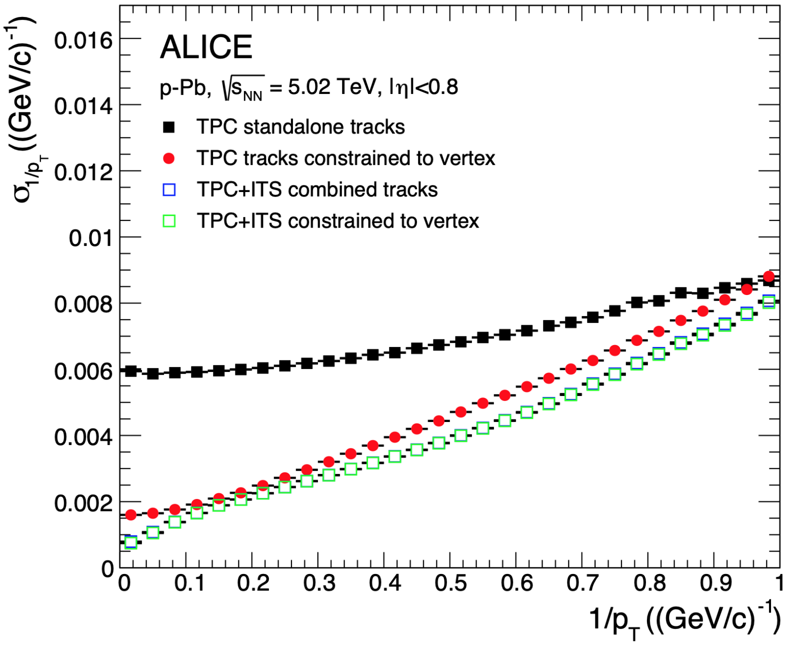

FIGURE 2.12: The p_T resolution for standalone TPC and ITS-TPC matched tracks with and without constraint to the vertex. The vertex constrain significantly improves the resolution of TPC standalone tracks. For ITS-TPC tracks, it has no effect (green and blue squares overlap).[1]

PCA is requested to be closer to the interaction vertex than the innermost hit of either of the two tracks; (c) Taking as θ the angle between the straight line connecting the V0 to the Vertex and the total momentum of the two candidate tracks $\overrightarrow{p}_{\text{pair}}$, $\cos(\theta)$ must be above 0.9. This last requirement is relaxed if the candidate has a momentum below 1.5 GeV/c. A schematic illustration of the secondary vertices search is shown in Figure 2.13.

2.3 Charged Particle Identification (PID) in ALICE

The ALICE experiment, despite being designed for heavy-ion collisions Physics in particular, is a general purpose experiment: this means that along with specific goals of studying established phenomena there is the will to explore previously unaccessible areas of high-energy Physics, both in pp, p-Pb, Pb-Pb collisions environments. This wide range of goals requires an excellent capability of reconstructing the full event and most of all, assign an identity to each track: that is the task of the particle identification. To this end a wide range of detectors are devoted to various degrees to the PID effort. A brief graphical summary is shown in Figure 2.14.

As it will be clearer further on, the main constraint on the particle identification for almost all methods is the detector resolution: an ideally perfect detector would provide a separation power over a practically infinite momentum span. The separation power is intended as the statistical power with which one can confirm or reject an identity hypothesis for a certain track. This is the main reason why all detectors aim at maximum precision in their measurements and that is ultimately a very relevant parameter for the detector goodness.

Most of our current technology is based on the understanding of electromag-

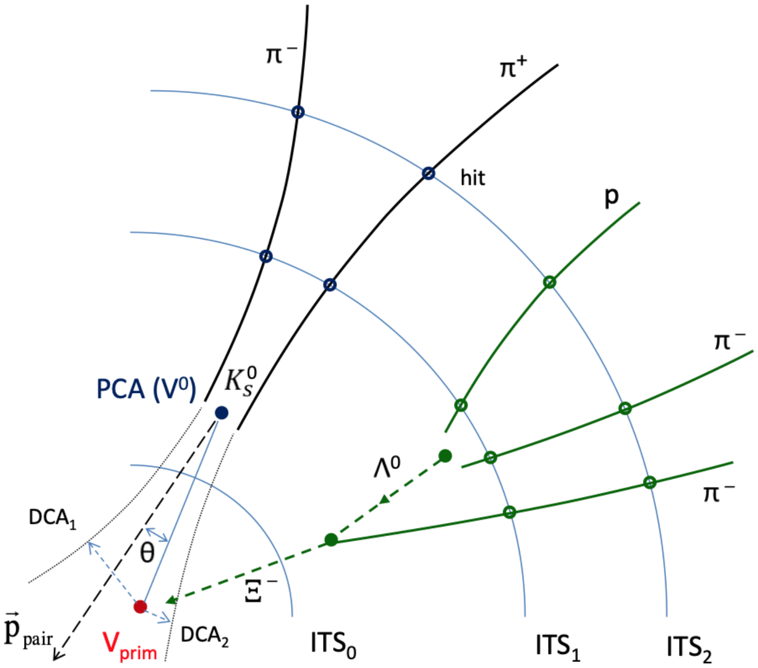

FIGURE 2.13: Secondary vertex reconstruction principle, with K^0_S and Ξ^- decays shown as an example. For clarity, the decay points were placed between the first two ITS layers (radii are not to scale). The solid lines represent the reconstructed charged particle tracks, extrapolated to the secondary vertex candidates. Extrapolations to the primary vertex and auxiliary vectors are shown with dashed lines. [1]

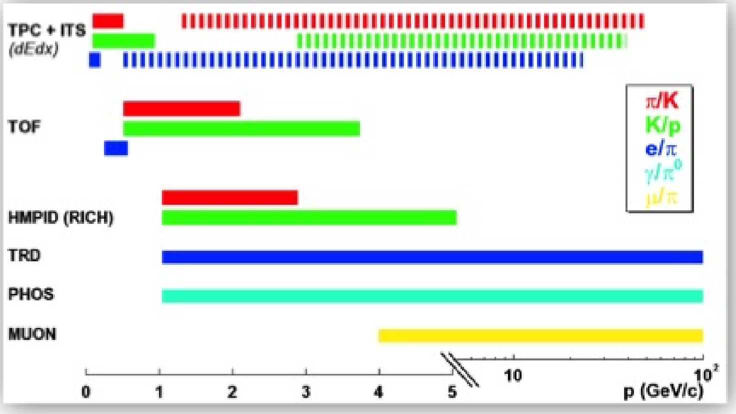

FIGURE 2.14: Particle Identification momentum ranges for various detectors

netic interactions and phenomena, thus giving a somewhat privileged status to the identification of charged particles. Because of this, a number of possible ways to detect charged particles have been developed and refined over the years and the ALICE experiment is an instance where almost every possible identification method is employed.

The three main methods are the energy loss through ionisation (ITS, TPC), Time Of Flight (TOF) and Cherenkov Radiation (HMPID). Each of these specialise in a certain range of momentum and/or particle species depending on the characteristics of the interaction that is used to perform the measurement and/or the detector location.

Energy Loss This method of particle identification is based on the measurement of energy lost by a charged particle by ionisation in a medium (dE/dx).

The basic principle is that a charged particle traversing a medium will ionize the material atoms, freeing an electron that can later be collected. The amount of electrons collected is directly proportional to the amount of energy lost in the medium by the particle through the first ionisation energy, that will determine the measurement resolution. Once the electrons are freed, a voltage can be applied to collect them, resulting in a change in the overall potential that can be measured through the electronics. The energy loss is dependent on the particle $\beta\gamma$ and charge: the assumption is that the $\beta\gamma$ does not vary throughout the particle path so each measurement can be used to derive the mean specific energy loss of the track.

Once the energy loss has been measured, the Bethe-Bloch formula is used to identify the particle:

$$-\frac{\mathrm{d}E}{\mathrm{d}x} = 4\pi N_e r_e^2 m_e c^2 \frac{z^2}{\beta^2}\left(\ln\frac{2m_e c^2\beta^2\gamma^2}{I} - \beta^2 - \frac{\delta(\gamma)}{2}\right) \tag{2.2}$$

where r_e,m_e are the electron classical radius and mass, c is the light speed, N_e is the mean electron density in the medium, β,γ are the relativistic factors of the particle, z is the particle charge, I is the mean excitation energy of the medium, $\delta(\gamma)$ is a high energy densities correction.

For the sake of simplicity and convenience, ALICE uses a different empirical parametrisation:

$$f(\beta\gamma) = \frac{P_1}{\beta^{P_4}}\Big(P_2 - \beta^{P_4} - ln(P_3 - \frac{1}{(\beta\gamma)^{P_5}})\Big) \tag{2.3}$$

where P_{1-5} are fit parameters and β, γ the relativistic factors. The energy loss found by this formula expresses the energy lost in a unit length. Once the $\beta\gamma$ of the track has been measured, combining it with the expectations from Bethe-Bloch formula with the measured dE/dx will allow one determine the most probable particle identity. The curves shown in Figure 2.15 are those of a typical energy loss for single charge particles in the ITS and TPC. The main limitation of this approach is that the separation power quickly reduces at high momentum, because of the shape of the Bethe-Bloch formula. As can be inferred by Equation 2.2 the ionisation depends both on the particle and on the medium. The effect of the relativistic rise of dE/dx is more pronounced for gaseous detectors such as the TPC, and negligible for silicon detectors such as the ITS. This difference is evident in their dE/dx spectra in Figure 2.15. The ITS has little room for separation over a few GeV/c, whilst the TPC can still achieve a moderate separation in the range of the tens of GeV/c.

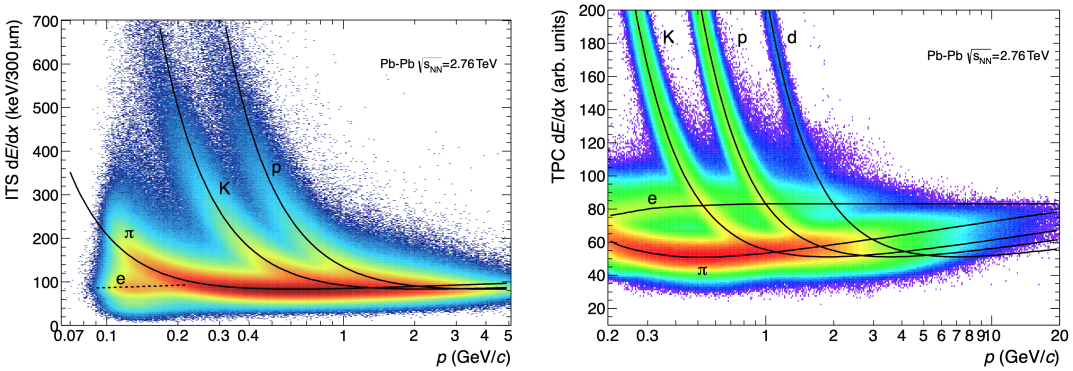

(A) Distribution of the energy-loss signal in the ITS as a function of momentum. Both the energy loss and momentum were measured by the ITS alone. [1]

(B) Specific energy loss in the TPC vs. particle momentum in Pb-Pb collisions at $\sqrt{s_{NN}}$ = 2.76 TeV. The lines show the parametrisation of the expected mean energy loss. [1]

FIGURE 2.15: Particle Identification by energy loss in TPC and ITS

ITS In the ITS only the outer four layers are able to provide information about energy loss. The cluster charge (derived by the ionisation of the crossing passing) is normalized to the track length found from the final track fit parameters, to retrieve a value of dE/dx for each layer. These measurements are then combined: if all four layers are available a mean of the lowest two values is performed, if three layers are available a weighted mean of the lowest (weight 1) and second lowest (weight $^{1}/_{2}$) is performed. A plot of the results of this procedure is shown in Figure 2.15a.

TPC In the TPC a large variety of physical properties are measured: momentum, charge, energy loss. This multiplicity of information gives the TPC the capability of making a stand-alone PID. In the low momentum range, up to 1 GeV/c, the PID can be performed on a track-by-track basis, whereas above that multi-Gaussian fits can still statistically separate particles with long tracks (over 130 samples) and with the truncated mean method (the one used in the ITS) the dE/dx peak has a Gaussian shape. The dE/dx precision is roughly $\approx 5\%$ (pp collisions) and $\approx 6.5\%$ (central Pb-Pb collisions). A plot of the results of this process are plotted in Figure 2.15b.

Time Of Flight This method of particle identification is based on the particle kinematics.

The basic principle is that if the particle velocity is measured together with its momentum, its mass can be recovered univocally identifying it through:

$$p = m\beta\gamma \rightarrow m = \frac{p}{\beta\gamma} \tag{2.4}$$

where p is the momentum, β is the particle velocity $\beta = v/c$ and γ is the relativistic factor. Here again the detector itself cannot identify the particle, but adds useful information onto the previous detectors measurements that can lead to PID. Specifically, the detector measures the time the particle takes to arrive at the TOF detector from the interaction point and uses the information about the momentum and track length from the reconstructed tracks.

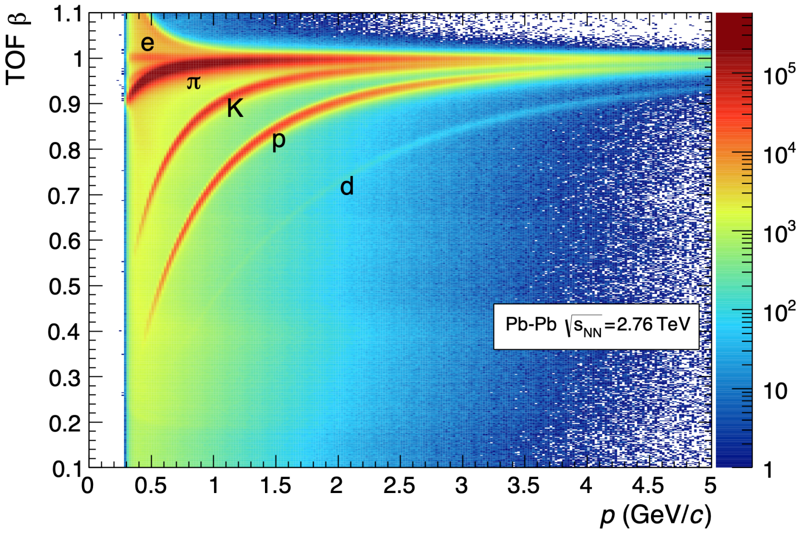

FIGURE 2.16: Distribution of β as measured by the TOF detector as a function of momentum for particles reaching the TOF in Pb-Pb interactions. [1]

TOF Detector A plot of the results of TOF measurements against the momentum measurement in the TPC are shown in Figure 2.15b, where the separation power can be appreciated. The majority of the background comes from mismatching of tracks to TOF hits in the high multiplicity environment of Pb-Pb collisions, showing that it is not related to the detector timing performance but rather it is related to track density. In fact for tracks above 1 GeV/c in Pb-Pb collisions the TOF pad occupancy is $\approx 6.7\%$ whereas the mismatch fraction is $\approx 6.5\%$.

Cherenkov Light This method of particle identification is based on a threshold phenomenon of light emission in a medium.
The Cherenkov phenomenon happens when charged particles speeding through a medium at velocities above the light speed in the medium itself: the result is a typical light emission. The emission happens with a typical refractive distribution centered around a certain angle θ defining the resulting cone of light, related to the speed of the particle (β) and the refractive index of the medium (n) by:

$$\cos(\theta) = \frac{1}{n\beta} \tag{2.5}$$

The goal of the detector is then to measure the angle θ, to be combined with the refractive index to find the particle speed and eventually with the particle momentum to determine the mass, as is the case with the TOF. In the Ring Imaging Cherenkov this is made by having the particle cross a layer of medium, to minimize velocity changes resulting in angle smearing, and then collecting the resulting photons on a "screen" (i.e. a detector plane) placed at some distance from the radiator. The collected photons are then grouped to reconstruct a ring on the screen and a fit is performed to measure the circle radius. The radius is then combined with the distance from the radiator to the screen to determine the angle θ.

HMPID The detector is a collection of 7 identical proximity-focusing RICH modules, with a refractive index for the radiator of $n \approx 1.289$ at $175\,\mathrm{nm}$. The PID

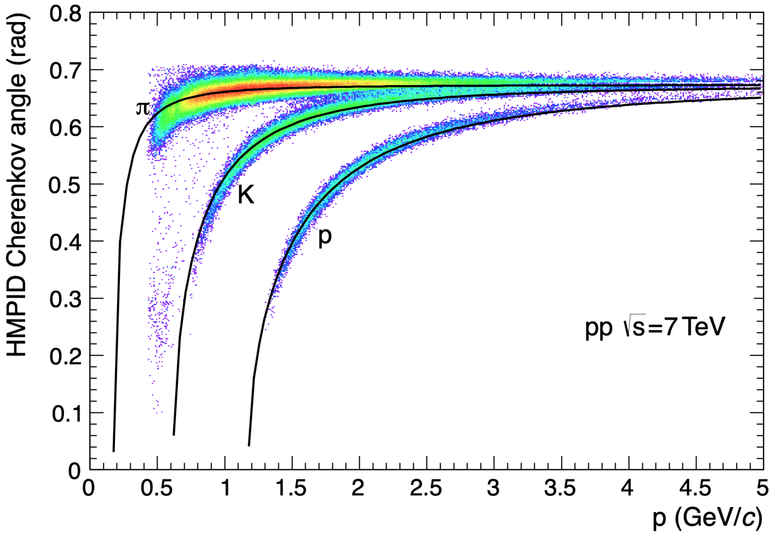

FIGURE 2.17: Particle Identification in the HMPID

is performed track-by-track. The detector contribution to the PID effort is strongly suppressed by the geometrical acceptance: the matching ratio to the TPC tracks is roughly 5%. A plot of the measurement of the Cherenkov angle contribution by the HMPID against the TPC momentum are reported in Figure 2.17.

Combined methods As mentioned throughout the methods, particle identification requires a number of measurements on the particle to be achieved, often performed by other detectors. This kind of "collaboration" can be extended to the results of the PID, comparing what the detectors predict for a certain track, to achieve a stronger statistical separation between species or a good separation over a wider momentum interval. Given for most analyses the relevant parameter is the p_T, rather than the more natural p for PID performance, the results and discussions in this sections have been converted to transverse momentum averaging the contributions at mid-rapidity $(-0.5 < \eta < 0.5)$.

Figure 2.18b provides a useful visualization of the concept of combining multiple detectors to efficiently identify particles over a large momentum range. The low p_T region is covered by the TPC and ITS, providing excellent separation power below 0.5 GeV/c. The intermediate p_T region is covered by the TOF, providing excellent separation power up to 3 GeV/c; in this region there is also the contribution of the HMPID, that nonetheless is limited by its small geometrical acceptance. In the high momentum range a combination of all detectors, depending on the particle species, can be used.

Figure 2.18a provides a visualization of the concept of combining multiple detector to enhance the separation power for a given particle species. The map combines TOF and TPC PID expected response for the pion hypothesis. On the X axis the expected energy loss for pions in the TPC is subtracted to the measurement for the energy loss of the incoming particle. On the Y axis the expected time of arrival for pions at the TOF is subtracted to the measurement for the time of arrival of the incoming particle. The combination of the two gives a clear peak at 0 representing the best pions candidates. This kind of combination can (and was) used to enhance the separation power up to 5 GeV/c in Pb-Pb. A statistical approach can also be implemented, using Bayesian methods based on the known yields to further enhance the

PID capabilities.

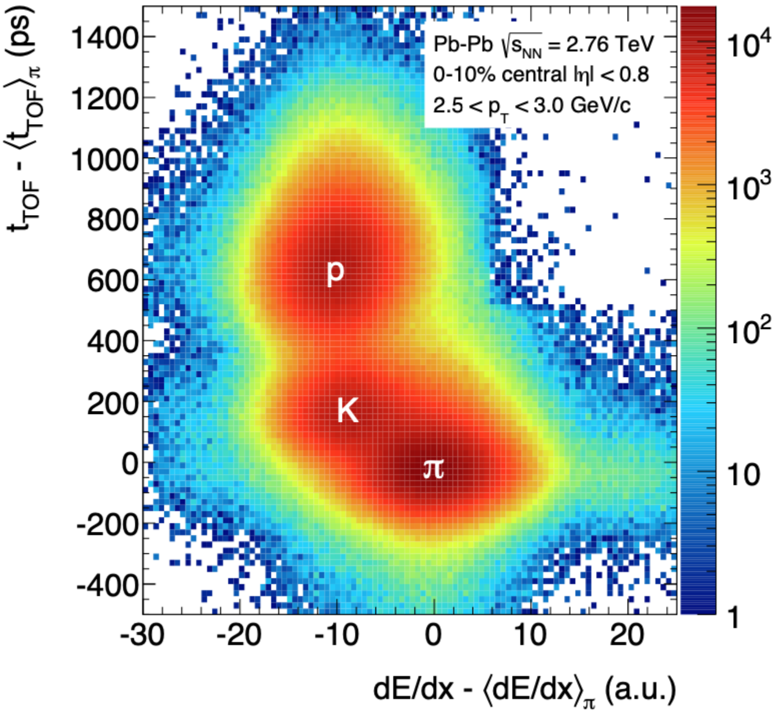

(A) Combined pion identification with TOF and with dE/dx in the TPC. [1]

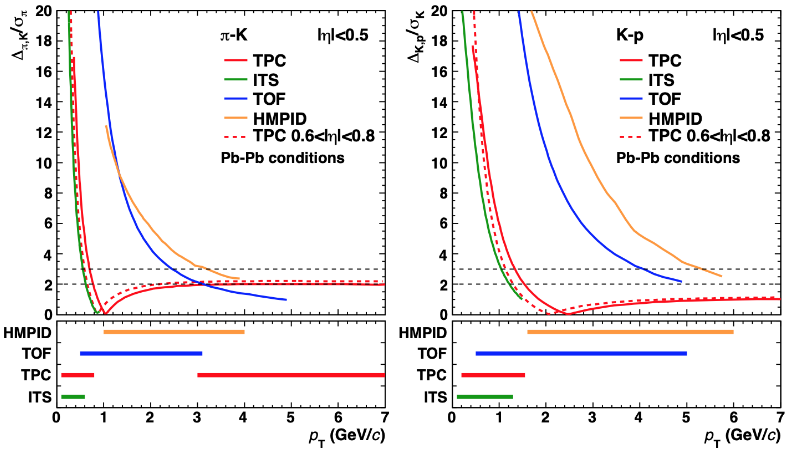

(B) Separation power of hadron identification in the ITS, TPC, TOF, and HMPID as a function of p_T at mid-rapidity. The left (right) panel shows the separation of pions and kaons (kaons and protons), expressed as the distance between the peaks divided by the resolution for the pion and the kaons, respectively, averaged over $-0.5 < \eta < 0.5$. For the TPC, an additional curve is shown in a narrower η region. The lower panels show the range over which the different ALICE detector systems have a separation power of more than 2σ. [1]

FIGURE 2.18: Particle Identification strategies combining multiple detectors. (A) Combination is used to enhance PID (B) Combination is used to extend p_T range over which the PID is satisfying.

Chapter 3

The Analysis Technique

The focus of the analysis is the measurement of the yield of ϕ-mesons *pairs*. The analysis starts by measuring the inclusive ϕ-meson yield, as was already performed by ALICE in 2012 [34] and uses the information given in the publication as a starting point and check for the performance of the analysis technique discussed in this chapter for the measurement of the yield of ϕ-meson pairs. After this step, the technique for the measurement of the inclusive yield undergoes a process of generalization to implement the technique for the measurement of ϕ-mesons pairs.

The generalization of the standard invariant-mass analysis technique for the signal extraction of inclusive resonance production consists in an extension of the concept in a multi-dimensional invariant-mass analysis. In this work we will use the 2-Dimensional generalization aimed at the measurement of the yield of ϕ-meson pairs using this novel methodology and tools that have developed specifically for this purpose in this work.

In this chapter we will discuss the core methods of the technique and how it has been validated with a Pythia 8 Monte Carlo sample of generated events. Before the discussion an introduction to the physical motivation of the analysis is outlined.

3.1 Motivation

The motivation of this analysis lays in the concept of Strangeness Enhancement.

Strangeness Enhancement (SE) is a phenomenon, as has been discussed in the first chapter of this thesis, consisting in an enhancement of the yield of particles that have a strange-quark content. The enhancement of the yield is proportional to the strangeness content, the higher the strangeness content of the particle the greater the enhancement. The first observations of this phenomenon were made in the heavy-ion collisions domain, making the corresponding pp collisions a natural benchmark to use as comparison. Nevertheless recent results at the LHC [6] have shown that SE is also present in high multiplicity pp collisions: a quite unexpected outcome. This discovery adds to a series of searches and studies highlighting the possible formation of a deconfined QCD phase in small systems, identifying typical heavy-ion collisions behaviors.

All of these considerations point toward our lack of a complete understanding of the underlying mechanisms in particle production in hadronic collisions, and are thus a goldmine of new information. In fact, albeit unexpected, these kind of new findings are always a good way to update our understanding and further improve our knowledge. To this goal, the presence of these new phenomena in the context of small systems is truly good news. The heavy-ion environment is generally very challenging and does not benefits from many eases the pp collisions environment does such as lower backgrounds, cleaner channels, simpler collision dynamics, etc.

This difference is quite evident when comparing the number of Monte Carlo models describing the two: heavy-ion physics is essentially relying on multiple models and steps to fully describe the evolution of the collision, whilst proton physics benefits from the use of simpler approaches implemented in multiple models for the description of the underlying physics: for example the Lund String Model. The extension of these phenomena in small systems makes it possible to try to explain their nature with different mechanism previously unaccessible.

To this end the present analysis poses itself as a start for a search for a more thorough characterization of strangeness production in pp collisions. The basic idea is that the measurement of the production of hadrons in pairs (as is the case for the ϕ-meson in this work) will enable to compare it to the inclusive yield of the hadron to extract novel information. Depending on the model taken as reference, in our case the Lund String Model, their mutual relation will differ. As we explained in the first chapter, there exists a probability $p_{s\bar{s}}$ of the string breaking into a $s\bar{s}$ quark pair, when this happens twice there is the possibility to produce a ϕ-meson with the s quark from the first and $\bar{s}$ from the second string breaking pair; if the string spanned between, as an example, $u\bar{u}$ quarks, the other strange quarks will contribute to forming kaons. If one more $s\bar{s}$ breaking occurs, a pair of ϕ-meson is formed from the fragmentation of the same string, hence bearing some degree of correlation due to the common formation. In this scenario we can expect the probability of producing a single meson P(ϕ) should relate to the probability of forming a pair P($\phi\phi$) as P(ϕ)^3 = P($\phi\phi$)^2; on the other hand for a purely statistical picture one would simply expect P(ϕ)^2 = P($\phi\phi$). This is the meaning behind our search for a way to measure the yield of pairs, as it can be used as a discriminant against different physical models. One convenient way to test the models in this context is to take the ratio P($\phi\phi$)/P(ϕ)^2 to determine wether it will be higher or lower. We will not be able to directly measure this quantity, but can manage to build something similar that can nonetheless help us understand the underlying mechanism. The ratio of the inclusive yields should be a good indicator.

3.2 Definition

This section will be devoted to introduce the main aspects and terminology of the analysis. We can start by the former, going through the process of recovering the simple integrated yield, which will also be instructive to understand how the technique to measure the yield of ϕ-meson pairs has been developed. The results in this section were achieved using a set of $\approx 400 \times 10^6$ events generated in the Pythia 8 Monte Carlo event generator. We used the default parameter settings, only activating the *SoftQCD:nonDiffractive* and *ParticleDecays:limitTau0* options. These options allow to switch on only QCD non-diffractive processes and allow the decay of particles whose proper lifetime do not exceed $c\tau$ = $10\,\mathrm{mm}$

Before diving into the analysis procedures, an introduction on general concepts can be worth taken. Ultimately our goal is to measure the number of ϕ meson produced in pp collisions with the ALICE detector, and we must take this fact into account. The first thing to know about the ϕ meson is that it cannot be directly detected: its proper lifetime is too short (cτ $\approx$$10\,\mathrm{pm}$) for the particle to reach the ITS and its decay vertex cannot be experimentally distinguished from the primary-collision vertex. This means that we need to choose a decay channel and use reconstruction techniques to infer the yield. This choice can easily come from examining the possible decay channels of the meson:

$$48.9\% \ \ \phi \rightarrow \mathrm{K}^+\mathrm{K}^-$$

$$34.2\% \ \ \phi \rightarrow \mathrm{K}^0_L\mathrm{K}^0_S$$

$$15.3\% \ \ \phi \rightarrow \rho\pi + \pi^+\pi^-\pi^0$$

$$\dots$$

$$\approx 0.03\% \ \ \phi \rightarrow \ell^+\ell^-$$

The first candidate to be discarded is the $\phi \rightarrow \rho\pi + \pi^+\pi^-\pi^0$ decay: the branching ratio is relatively low and the final state is extremely difficult to reconstruct, suffering from high background of pions coming from the underlying event.

The second candidate to be discarded is the $\phi \rightarrow \mathrm{K}^0_L\mathrm{K}^0_S$ decay: even though the branching ratio is fairly high, the neutral nature of the daughter particles complicates the analysis. Moreover the K^0_L has a long proper lifetime, and mostly decays outside of the detector making it impossible to reconstruct.

The third candidate to be discarded is the $\phi \rightarrow \mu^+\mu^-$ decay: it is a relatively clean, charged decay, but it suffers from a very low branching ratio and for the fact that in ALICE the number of actual candidates accepted by the detector would be minimal (ALICE only has dedicated muon detectors in the forward region), strongly limiting the analysis efficiency. The $\phi \rightarrow e^+e^-$ decay would be more reliable, as the central barrel region can efficiently reconstruct electrons, nevertheless the branching ratio still poses a concern.

The optimal choice is the $\mathrm{K}^+\mathrm{K}^-$ decay: it has the highest branching ratio available, the daughter particles are just two, charged, and it happens to be particles for which ALICE performs best, even in the low $\mathrm{p_T}$ region. Recalling Section 2.3 ALICE has an excellent PID performance for charged hadrons.

Now that we established a decay channel we need to examine our sensitivity to reconstruct the decay products. Again we must consider constraints of the detector that will be used to perform the measurement. To mimic detector dead regions and efficiencies a kinematic cut on the kaon tracks is performed. The kaon tracks are assumed to have perfect identification, but must have at least 0.15 GeV/c of transverse momentum and must be produced within $-0.8 < \eta < 0.8$ in pseudo-rapidity. These constraints are found to prevent ϕ candidates with $\mathrm{p_T}$ lower than 0.4 GeV/c from being efficiently reconstructed. This discussion will be extended and this choice justified once the technique is employed on real data. Moreover a cut in the rapidity of the ϕ-meson candidates reconstructed from K^+ K^- pairs is performed to define the region in which we are measuring, only accepting ϕ-meson in mid-rapidity interval, $-0.5 <\mathrm{y}< 0.5$.

Before starting with the inclusive yield analysis of ϕ-meson production we lay some notation that will be used throughout the next chapters, summarized in Table 3.1.

3.2.1 ϕ-meson inclusive yield analysis

The inclusive yield analysis is performed as a start, and it can be regarded as a way to get a first sense of the analysis methods and sources of concern. Throughout the text this part of the analysis technique will be referred to as the "1-Dimensional" analysis and the result will be regarded as the "1-Dimensional" yield.

The first step is the measurement of the inclusive yield *as is*, i.e only counting the ϕ mesons we are able to reconstruct. Here we encounter the first bump on the road: we mentioned the ϕ meson has a strong decay in the kaon pair, resulting in the impossibility of reconstruction for its decay vertex experimentally. The approach

Data notation	MC notation	Definition
Raw	Rec	Raw yield, equivalent to the recordable real candidates
Res	Tru	Corrected yield, equivalent to all real candidates

TABLE 3.1: Summary of the notation convention that will be used throughout the analysis.

to follow is then to pair all kaons that have opposite charge in an event as ϕ-meson candidates. This will produce a set of candidates that cannot be identified as true ϕ-meson decays *singularly*, but can be discriminated *globally*. This is performed via the use of an invariant mass histogram where the invariant mass (M) is:

$$M^2 = (E_1 + E_2)^2 - \|\mathbf{p}_1 + \mathbf{p}_2\|^2 = m_1^2 + m_2^2 + 2\left(E_1E_2 - \mathbf{p}_1 \cdot \mathbf{p}_2\right) \tag{3.1}$$

where E_1,E_2 are the particles energies and p_1,p_2 are the momenta of the particles. The invariant mass represents the mass of the hypothetical particle the kaons have decayed from. From this it is straightforward to understand that uncorrelated kaons will form a candidate with a combinatorial invariant-mass distribution invariant mass, creating an irreducible background we will need to get rid of, whereas the true ϕ-meson decay products will always populate the same region, following a relativistic Breit-Wigner distribution (natural units):

$$f(M) = \frac{k}{\left(M^2 - M_0^2\right)^2 + M_0^2\Gamma^2}; \quad k = \frac{2\sqrt{2}M_0\Gamma\gamma}{\pi\sqrt{M_0^2 + \gamma}}; \quad \gamma = \sqrt{M_0^2\left(M_0^2 + \Gamma^2\right)}; \tag{3.2}$$

where M is the invariant mass of the decay products, M_0 is the mass of the resonance and Γ is its width.

Signal extraction

Signal extraction is the practical procedure to measure the yield, applying the concept of invariant mass technique described above. The kaon pair candidates are filled in a histogram creating the typical peak around the resonance mass, clearly visible in Figure 3.1.

The goal is then to extract the signal component from the total distribution of the background and the signal. As mentioned before, the signal is the number of kaons pairs correctly combined in a true ϕ-meson candidate, and the background is the remaining group of accidental combinations of kaons. To do so, we set up a fit function that incorporates the two components and use it to evaluate the relative magnitude of the signal with respect to the background.

We already defined the shape of our signal (Eq. 3.2). Even though the most rigorous approach would require the use of the relativistic Breit-Wigner, for such a narrow resonance the difference is experimentally undetectable. Moreover the Pythia generator uses the non-relativistic version, giving more credit to the choice. Unfortunately the background does not posses such and elegant and known shape. For this reason it is often useful to use functions that can adapt to various shapes without *a priori* knowledge: polynomials are then a natural choice, as any useful function can always be expressed as a polynomial series. In this work we used Chebyshev polynomial of fourth degree to fit the background, that is a linear combination of the first four Chebyshev polynomials, defined as:

$$T_0(x) = 1; \qquad T_1(x) = x; \qquad T_{n+1}(x) = 2xT_n(x) - T_{n-1}(x); \tag{3.3}$$

The fit function is then:

$$f_{1\mathrm{D}}(M, \overrightarrow{a}, \overrightarrow{b}) = c^{sig} f^{sig}(M, \overrightarrow{a}) + c^{bkg} f^{bkg}(M, \overrightarrow{b}) \tag{3.4}$$

Where $\overrightarrow{a}, \overrightarrow{b}$ are the parameters of the functions, c^{sig}, c^{bkg} are the normalization coefficients, representing the integral of signal in the sample, and f^{sig}, f^{bkg} are the Breit-Wigner and Chebyshev polynomial respectively, with integrals normalized to unity.

Now that we have a general idea of the procedure we can start going into detail: the first thing to do is define the boundaries in which we search for our signal. We know the ϕ-meson has a mass of $\approx$ 1.019 GeV/c^2 and that will roughly be our histogram center. We now need to establish the lower and upper limit. The resonance width is $\approx$ 4 MeV, so a first approximation could be a range of mass 0.98 GeV/c^2 < $m_{K^+K^-}$ < 1.05 GeV/c^2 to include 8 widths, i.e. $m_{K^+K^-} \in [m_\phi - 8\Gamma_\phi, m_\phi + 8\Gamma_\phi]$. Nevertheless given we are reconstructing the ϕ-meson in the K$^+$K$^-$ decay channel, that have a mass of their own of about $\approx$ 0.495 GeV/c^2, it is kinematically impossible to reconstruct masses below 0.495×2 GeV/c^2, that is about 0.99 GeV/c^2, so we move our lower bound to this value.

This method will extract the inclusive yield for reconstructible ϕ-mesons, i.e. having transverse momentum over 0.4 GeV/c. This is the signal we are directly able to measure. To be able to extrapolate this yield to lower values of p_T we need to differentiate this value into bins of p_T to study the p_T spectrum shape and extrapolate down to p_T = 0 GeV/c. The results in some of the p_T bins are shown in Figure 3.1, and the changing background can be clearly seen, justifying the choice of an adaptable fit function.

The fit is performed using the RooFit statistical framework [35]. The default fit set up is taken to be:

1. The ϕ-meson mass and width are let free to vary within 10% of the PDG value [11].
2. The Chebyshev polynomials coefficients are let free to vary in [-1,+1].
3. The invariant mass fit region is taken to be [0.95,1.05] GeV/c^2.

Signal corrections

The yield extracted from the invariant mass histograms does not represent the actual production yield.

This discrepancy comes from the fact that we applied several cuts to our sample and thus we are missing a part of the total mesons produced in the collisions. We then need to estimate the inefficiencies and correct the yield accordingly. The first obvious correction is the Branching Ratio (BR): given we are measuring the yield of ϕ mesons decaying into charged-kaons pairs we need a correction to retrieve the original ϕ-meson yield. So a general rule would be:

$$\mathrm{N}^{\mathrm{RES}} = \frac{\mathrm{N}^{\mathrm{RAW}}}{\varepsilon_{\mathrm{T}}} \tag{3.5}$$

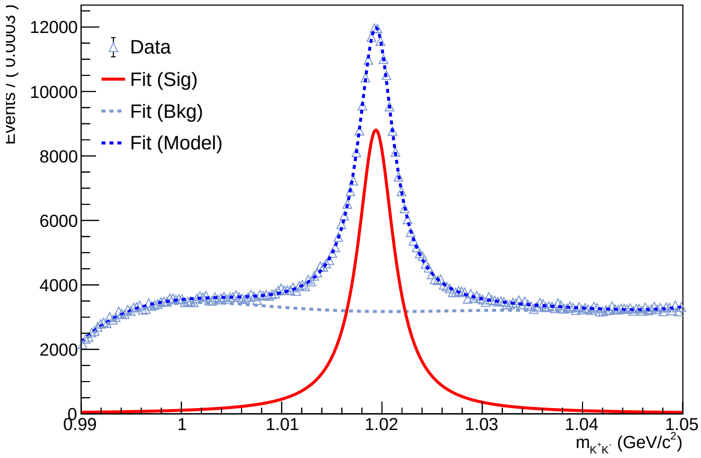

(A) 1-Dimensional K^+K^- Invariant Mass histograms with fit results highlighted, for ϕ-meson p_T in [0.4-0.5] GeV/c.

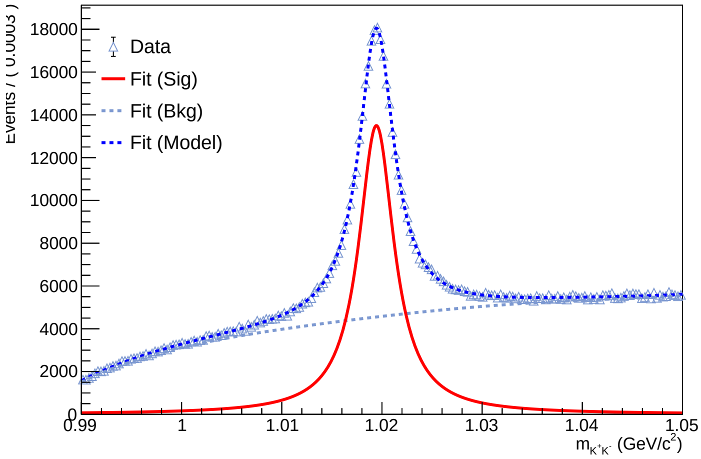

(B) 1-Dimensional K^+K^- Invariant Mass histograms with fit results highlighted, for ϕ-meson p_T in [1.0-1.1] GeV/c.

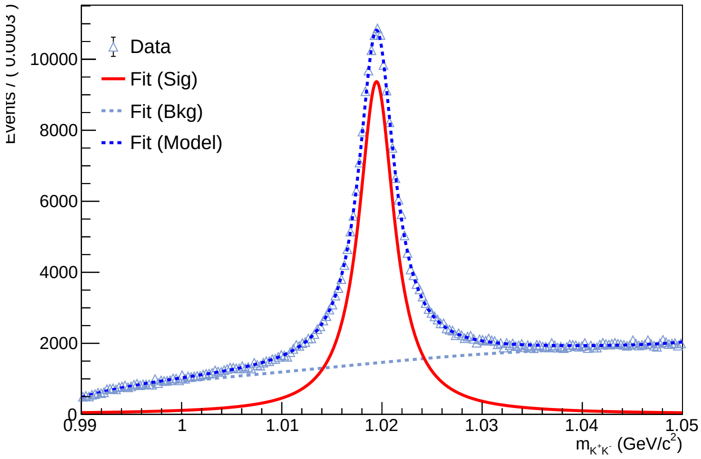

(C) 1-Dimensional K^+K^- Invariant Mass histograms with fit results highlighted, for ϕ-meson p_T in [2.0-2.2] GeV/c.

FIGURE 3.1: Examples of 1-Dimensional K^+K^- Invariant mass histograms with fit results highlighted: red line is the signal, dashed light blue line is the background and dashed blue line is the full model.

where we used the notation introduced earlier, N is the yield (in this case the differential yield in transverse momentum) and ε_T the overall efficiency accounting for all corrections.

In this Monte Carlo environment the only other correction required is that related to the acceptance of the tracks with respect to the cuts used in the selection. To this end we can use the Monte Carlo truth to count all the generated ϕ meson decaying in charged-kaons pairs (N^GEN) and all the generated ϕ meson decaying in charged-kaons pairs that have both decay tracks within the reconstruction constraints (N^REC). This is performed for all $\mathrm{p_T}$ bins and the bin-by-bin efficiency is then:

$$\varepsilon_{rec}(\mathrm{p_T}) = \frac{\mathrm{N}^\mathrm{REC}(\mathrm{p_T})}{\mathrm{N}^\mathrm{GEN}(\mathrm{p_T})} \tag{3.6}$$

the efficiency is measured considering only the ϕ meson generated at mid-rapidity, consistently with the analysis.

Accounting for these two factors one would get the Result yield (RES):

$$\mathrm{N}^\mathrm{RES}(\mathrm{p_T}) = \frac{\mathrm{N}^\mathrm{RAW}(\mathrm{p_T})}{\varepsilon_{rec}(\mathrm{p_T}) \times \mathrm{BR}} \tag{3.7}$$

Once N^RES is found, the differential yield can be found by dividing by the number of events ($\mathrm{N_{events}}$) and by the $\mathrm{p_T}$ bin width:

$$\frac{\mathrm{d}^2 N_\phi}{\mathrm{d}y\mathrm{dp_T}} = \frac{\mathrm{N}^\mathrm{RES}(\mathrm{p_T})}{\mathrm{N_{events}} \times \Delta y \times \Delta \mathrm{p_T}} \tag{3.8}$$

where Δy is 1, as the measurement is performed in mid-rapidity ($-0.5 < y < 0.5$). For the sake of simplicity when comparing the measured yields to the Monte Carlo truths the Raw yield is going to be corrected to be graphically similar to the inclusive differential yield. We can then define one more yield:

$$\frac{\mathrm{d}^2 N_\phi}{\mathrm{d}y\mathrm{dp_T}} = \frac{\mathrm{d}^2 N_\phi^\mathrm{RES}}{\mathrm{d}y\mathrm{dp_T}} = \frac{\mathrm{N}^\mathrm{RES}(\mathrm{p_T})}{\mathrm{N_{events}} \times \Delta y \times \Delta \mathrm{p_T}} \tag{3.9}$$

$$\frac{\mathrm{d}^2 N_\phi^\mathrm{RAW}}{\mathrm{d}y\mathrm{dp_T}} = \frac{\mathrm{N}^\mathrm{RAW}(\mathrm{p_T})}{\mathrm{N_{events}} \times \Delta y \times \Delta \mathrm{p_T}} \tag{3.10}$$

Signal extrapolation

We mentioned earlier the need to extrapolate down to $\mathrm{p_T}$ = 0 GeV/c introducing a binned histogram from $\mathrm{p_T}$ = 0.4 GeV/c to $\mathrm{p_T}$ = 10 GeV/c: formally we would also need an extrapolation beyond 10 GeV/c, but the contribution in this region is negligible (0.04% from Pythia 8 estimates). This need arises from our search for the total inclusive yield, which demand that we extrapolate in the region where our detectors do not provide us with measurement. The extrapolation process is fairly simple in principle: based on the measured yield and on some *a priori* knowledge, as the fact that the yield at $\mathrm{p_T}$ = 0 GeV/c must be zero, one makes an assumption on the shape of the $\mathrm{p_T}$ distribution. A fit is performed to the measured differential $\mathrm{p_T}$ distribution with a function that parametrises the distribution and the resulting fit function parameters are used to evaluate the yield in the unmeasured regions.

The function chosen to describe the shape of the spectrum is a Levy-Tsallis parametrisation that is usually used in high-energy physics to this purpose:

$$\frac{\mathrm{d}^2 N}{\mathrm{d}y\mathrm{d}\mathrm{p}_\mathrm{T}} = \frac{(n-1)(n-2)}{nT(nT+M_0(n-2))} \times \frac{\mathrm{d}N}{\mathrm{d}y} \times p_\mathrm{T} \times \left(1+\frac{m_T - M_0}{nT}\right)^{-n} \tag{3.11}$$

Where n, T are free parameters, $\mathrm{p_T}$ is the transverse momentum, $m_T = \sqrt{m^2+p_\mathrm{T}^2}$. The quantity we are interested in, the $\mathrm{p_T}$ integrated yield, is represented by $\mathrm{d}N/\mathrm{d}y$ and does not need any further corrections since the rapidity bin is exactly 1. Once the extraction has been performed, i.e. the fit, the unmeasured yield is obtained by integrating the fit function in the region of interest. The total inclusive integrated production yield is obtained by adding the the yields in the measured $\mathrm{p_T}$ region to the extrapolated ones:

$$\frac{\mathrm{d}N_\phi}{\mathrm{d}y} = \int_0^{0.4} f_{\text{L-T}}(\mathrm{p_T}, n, T, m)\mathrm{d}\mathrm{p_T} + \sum_{i=1}^{\mathrm{N_{bins}}} H(\mathrm{p}_{\mathrm{T},i})\Delta \mathrm{p}_{\mathrm{T},i} \tag{3.12}$$

where $f_{\text{L-T}}$ is the Levy-Tsallis function with the parameters set to the fit results on the measured region, $\mathrm{N_{bins}}$ is the number of bins in the differential yield histogram, $H(\mathrm{p}_{\mathrm{T},i})$ is the content of histogram i-th bin centered at the $\mathrm{p_T}$, $\Delta\mathrm{p}_{\mathrm{T},i}$ is the i-th bin width; the i index runs through all the histogram bins.

3.2.2 ϕ-meson pair analysis

The measurement of the production of ϕ-meson pairs generalise the inclusive case explained before with an extension to 2-Dimensional invariant mass analysis. This part of the analysis will be referred to as the "2-Dimensional" analysis and the yield of ϕ-meson pairs will be referred to as the "2-Dimensional yield" throughout the text.

Many aspects of this process will require a brief discussion to justify the choices we made, so the best approach is to follow the same step-by-step approach we used to describe the inclusive yield measurement.

The first instance of difference from the previous method is the building of the invariant mass histogram that is going to be fitted. Given that we want to measure the yield of ϕ-meson pairs, we need to extend the idea to a 2-Dimensional space and the simplest way is to think of a 2-Dimensional histogram that has the two candidates invariant mass projected onto each axis. This means that the x-axis will show the first candidate invariant mass and the y-axis will show the second candidate invariant mass. This way we need to search for a way to extract the signal, that accounts for combinations where both candidates are real ϕ-mesons.

Before proceeding to the signal extraction we need to think a bit more about the way we are filling this histogram. Whereas the 1-Dimensional fill basically only required that the kaons were from the same event and have opposite charge, the 2-Dimensional case needs a bit more careful considerations to avoid unphysical combinations. To avoid reducible background we associate to each kaon a unique number, to identify it. When combining them into pairs we keep track of such number, labelling the pair as $\{K^+_\mathrm{A}, K^-_\mathrm{B}\}$ to use when combining pairs, checking that there are no common kaons. For instance, combinations like $\{K^+_\mathrm{A}, K^-_\mathrm{B}\}$ and $\{K^+_\mathrm{C}, K^-_\mathrm{B}\}$ is forbidden. This automatically avoids all non-physical pair candidates. When we go through the list of physically acceptable pairs of ϕ candidates two approaches can be used:

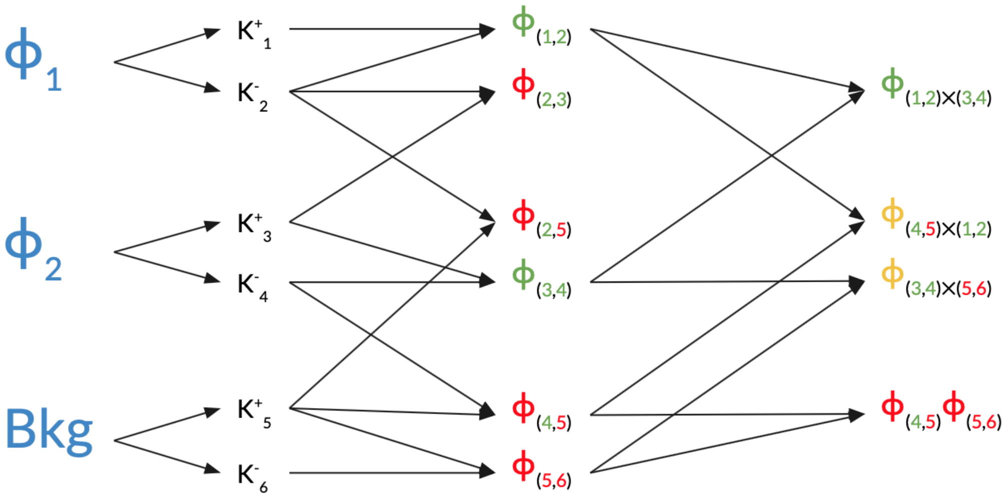

FIGURE 3.2: Schematic representation of 2-Dimensional Invariant Mass histograms build: red candidates represent *bkg* or *bkg*×*bkg*, yellow candidates represent *bkg*×*sig* (*sig*×*bkg*), and green candidates represent *sig* or *sig*×*sig*. In the kaons indices a green index represents a kaon from a ϕ decay and a red index otherwise.

1. We take the first candidate, compare it with the others except itself, fill the corresponding histograms. Then we take the second candidate, compare it with *the others except itself and the first*, fill the corresponding histograms.
2. We take the first candidate, compare it with the others except itself, fill the corresponding histograms. Then we take the second candidate, compare it with *all the others except itself*, fill the corresponding histograms.

In the second case we are imposing a symmetrical procedure, as the order by which we arrange the candidates has no effect on the final histogram shape, whereas the first generates a dependence on how the list is built. On the other hand, in the second case, we must take into account the fact that the same pair is used twice: we then fill weighting each entry as 1/2. We will be using the second approach as it has advantages from the imposed symmetry. A schematic representation of this procedure can be seen in Figure 3.2.

Next we can tackle the fit. This time the components are less straightforward:

- Our main goal is to measure the Signal component, that is a pair of real ϕ-mesons. This means that, in terms of 1-Dimensional components, our signal is the combination of two signal components, *sig*(M_1)×*sig*(M_2). M_i is the invariant mass of the i-th ϕ-meson candidate.
- Our background will be anything else. Speaking in terms of the 1-Dimensional components, the other three possible combinations are:
  1. *sig*(M_1)×*bkg*(M_2)
  2. *bkg*(M_1)×*sig*(M_2)
  3. *bkg*(M_1)×*bkg*(M_2)

  when coupling a real ϕ meson with background, or when pairing background candidates.

The presence of multiple components within the sample requires a more sophisticated fit procedure to correctly identify them. To this goal a product of the 1-Dimensional fit function (Eq. 3.4) is performed, and all the components are correctly described:

$$
\begin{aligned}
f_{\mathrm{2D}}(M_1, \overrightarrow{a}_1, \overrightarrow{b}_1 | M_2, \overrightarrow{a}_2, \overrightarrow{b}_2) = f_{\mathrm{1D}}(M_1, \overrightarrow{a}_1, \overrightarrow{b}_1) \times f_{\mathrm{1D}}(M_2, \overrightarrow{a}_2, \overrightarrow{b}_2) = \quad (3.13) \\
= \underbrace{c_1^{sig} f^{sig}(M_1, \overrightarrow{a}_1^j) \times c_2^{sig} f^{sig}(M_2, \overrightarrow{a}_2^j)}_{sig \times sig} + \\
+ \underbrace{c_1^{sig} f^{sig}(M_1, \overrightarrow{a}_1^j) \times c_2^{bkg} f^{bkg}(M_2, \overrightarrow{b}_2^j)}_{sig \times bkg} + \\
+ \underbrace{c_1^{bkg} f^{bkg}(M_1, \overrightarrow{b}_1^j) \times c_2^{sig} f^{sig}(M_2, \overrightarrow{a}_2^j)}_{bkg \times sig} + \\
+ \underbrace{c_1^{bkg} f^{bkg}(M_1, \overrightarrow{b}_1^j) \times c_2^{bkg} f^{bkg}(M_2, \overrightarrow{b}_2^j)}_{bkg \times bkg} +
\end{aligned}
$$

The measured range is still the same, but the 2-Dimensional differentiation in $\mathrm{p_T}$ will be less granular to have a reasonable number of counts in each 2-Dimensional bin in transverse momentum. An example of these histograms can be seen in Figure 3.3.

Signal extraction

The signal extraction procedure is similar to the one performed on the 1-Dimensional histogram.

Some consideration in performing it is nonetheless required. Indeed the straightforward generalization would require that a 2-Dimensional fit to be performed using the simple combination of fit functions described in Equation 3.13. This would be a very challenging procedure due to the low statistics of the histograms that are fitted compared to the number of free parameters of such a configuration; background parameters are 5×2, signal parameters are 2×2 and integral coefficients for each component are 4, giving a grand total of 18 free parameters. In an attempt to ease the burden on the fit algorithm, the fit procedure is divided in two steps.

We proceed to build 1-Dimensional histograms using the 2-Dimensional $\mathrm{p_T}$ bin scheme. These 1-Dimensional histograms represent the yield of ϕ-meson candidates within a certain $\mathrm{p_T}$ range. The assumption is that the background and signal shapes, i.e. their function parameters, would still be the same in a 2-Dimensional conditional yield, the only difference being that there would be a scale factor due to the matching to a given $\mathrm{p_T}$ candidate on the other axis. This can be clearer by looking at the expression:

$$
H(\mathrm{p_T}\phi_1, \mathrm{p_T}\phi_2, M_1, M_2) = H_1(\mathrm{p_T}\phi_1, M_1) \times H_2(\mathrm{p_T}\phi_2, M_2) \quad (3.14)
$$

where H_i is an invariant mass histogram, $\mathrm{p_T}\phi_i$ is the momentum of the ϕ-meson candidate. This means that we can fit H_1 and H_2 histograms independently, using the 1-Dimensional paradigm explained earlier, and the resulting parameters can be used to fix the shape of the signal and the background. This procedure greatly

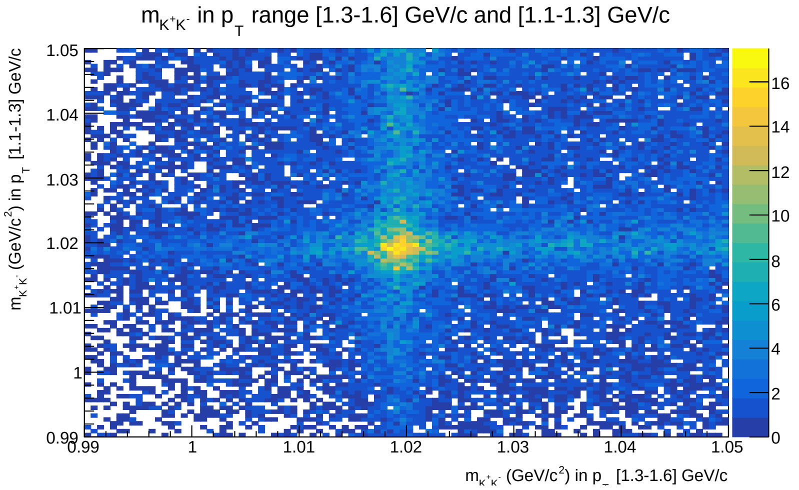

(A) An example of a 2-Dimensional invariant mass histogram represented through a color map.

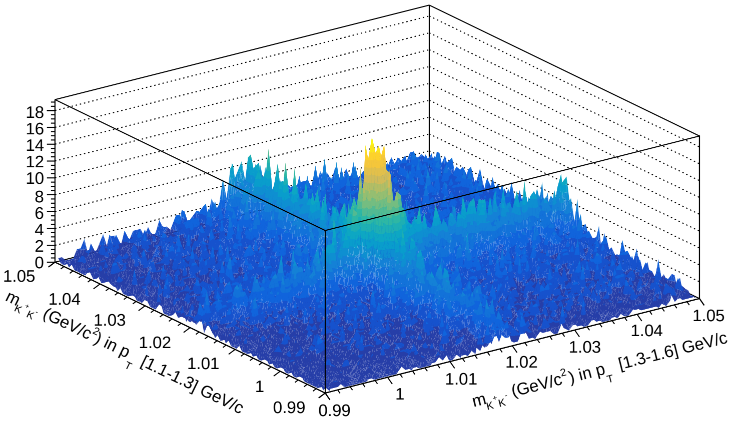

(B) An example of a 2-Dimensional invariant mass histogram represented through a surface map.

FIGURE 3.3: 2-Dimensional K^+K^- Invariant Mass histogram for $p_T\phi_1$ in [1.3-1.6] GeV/c and $p_T\phi_1$ in [1.1-1.3] GeV/c.

simplifies the fit algorithm, reducing the free parameters to the 4 normalization coefficients. The resulting yield for the $\mathrm{p_T}$ bin will be the integral coefficient for the $sig \times sig$ component only. A series of examples of the fit results are shown in Figure 3.4

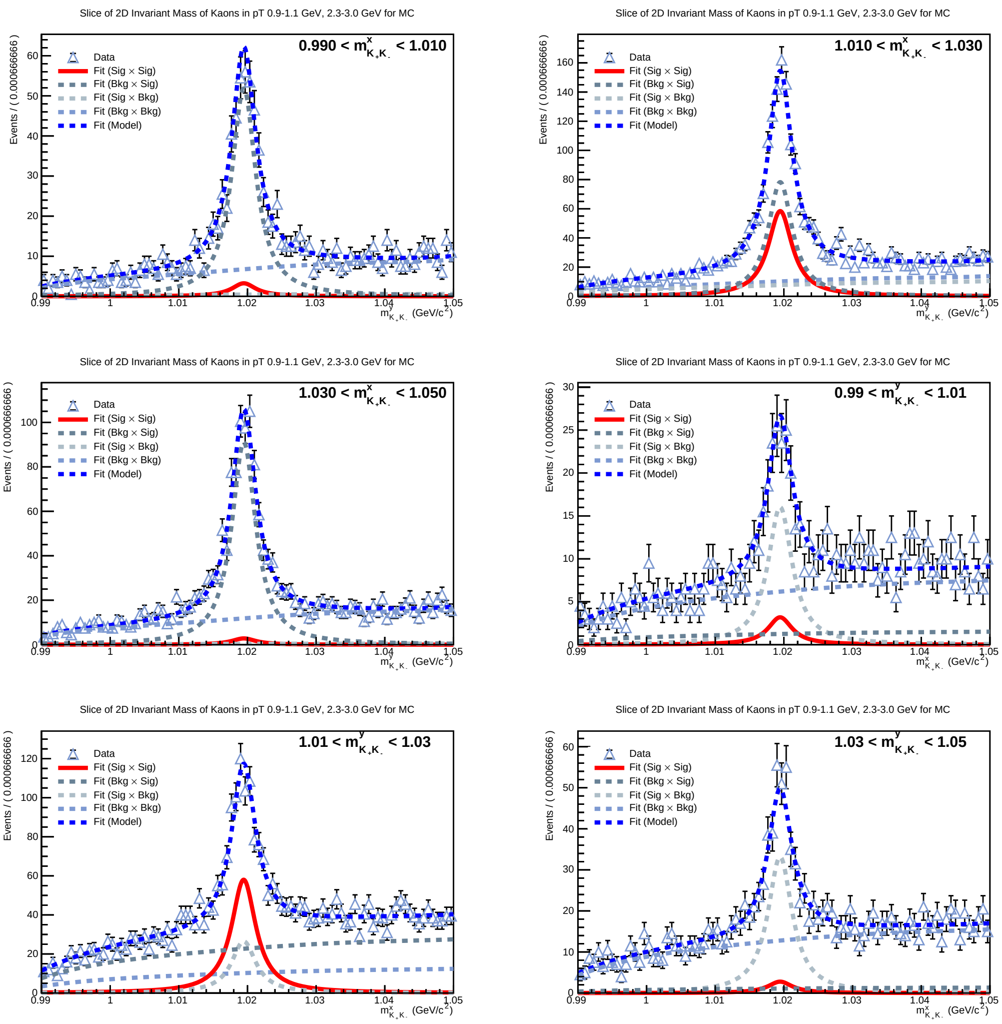

FIGURE 3.4: 2-Dimensional Invariant mass histogram fitted, with Fit components highlighted: red line is the signal, dashed light blue line is the background and dashed blue line is the full model. The data and fit are shown after an invariant mass cut to represent in 1-Dimension the 2-Dimensional histogram

Signal corrections

All discussions made in the previous sections are valid for the 2-Dimensional case, with some due reflections, and the generalization is quite straightforward. The reconstruction efficiency can be taken as was defined in Equation 3.6, generalizing the concept, introducing the conditional efficiency:

$$\varepsilon_{rec}(\mathrm{p_T}\phi_1, \mathrm{p_T}\phi_2) = \frac{\mathrm{N^{REC}}(\mathrm{p_T}\phi_1, \mathrm{p_T}\phi_2)}{\mathrm{N^{GEN}}(\mathrm{p_T}\phi_1, \mathrm{p_T}\phi_2)} \tag{3.15}$$

where $\mathrm{N}^{\mathrm{REC}}(\mathrm{p_T}\phi_1,\mathrm{p_T}\phi_2)$ is the number of all the generated ϕ meson decaying in charged-kaons pairs that have both decay tracks within the reconstruction constraints *that are produced in an event where a ϕ meson with momentum $p_T\phi_{1,2}$ was also produced.* Similarly, $\mathrm{N}^{\mathrm{GEN}}(\mathrm{p_T}\phi_1,\mathrm{p_T}\phi_2)$ is the number of all the generated ϕ meson decaying in charged-kaons pairs *that are produced in an event where a ϕ meson with momentum $p_T\phi_{1,2}$ was also produced.* This ratio gives a 2-Dimensional efficiency evaluated in a bin-by-bin fashion. This implies that the Monte Carlo dataset is unevenly split in a conspicuous number of bins and this might give rise to some considerable fluctuations in the less populated ones.

In an attempt to reduce the statistical uncertainty on the efficiency evaluation, a methodology is proposed. Given the conditional nature of the 2-Dimensional efficiency, the result can be achieved by a multiplication of 1-Dimensional efficiencies: the efficiency over the full $\mathrm{p_T}\phi_1$ spectrum is $\varepsilon(\mathrm{p_T}\phi_1)$. The more stringent requirement is for this ϕ_1 meson to be produced together with another ϕ_2 meson of transverse momentum $\mathrm{p_T}\phi_2$ that will have an efficiency of $\varepsilon(\mathrm{p_T}\phi_2)$. Thus it is straightforward to consider the 2-Dimensional efficiency as simply:

$$\varepsilon(\mathrm{p_T}\phi_1,\mathrm{p_T}\phi_2)=\varepsilon(\mathrm{p_T}\phi_1)\times\varepsilon(\mathrm{p_T}\phi_2) \tag{3.16}$$

This approach can be validated comparing the evaluated 2-Dimensional efficiency with the 1-Dimensional product (Fig. 3.5). The use of this method greatly enhances the precision of the acceptance and greatly reduces its associated error, and will be the evaluation method used in this analysis.

The generalization of the double differential pair Result yield is then straightforward:

$$\mathrm{N}^{\mathrm{RES}}(\mathrm{p_T}\phi_1,\mathrm{p_T}\phi_2)=\frac{\mathrm{N}^{\mathrm{RAW}}(\mathrm{p_T}\phi_1,\mathrm{p_T}\phi_2)}{\varepsilon_{rec}(\mathrm{p_T}\phi_1,\mathrm{p_T}\phi_2)\times\mathrm{BR}^2} \tag{3.17}$$

As is the generalization of the double differential ϕ-meson pair yield:

$$\frac{\mathrm{d}^3N_{\phi\phi}}{\mathrm{d}y\mathrm{d}\mathrm{p_T}\phi_1\mathrm{d}\mathrm{p_T}\phi_2}=\frac{\mathrm{N}^{\mathrm{RES}}(\mathrm{p_T}\phi_1,\mathrm{p_T}\phi_2)}{\mathrm{N_{events}}\times\Delta y\times\Delta\mathrm{p_T}} \tag{3.18}$$

As we introduced earlier, a notation for a more easy visualization of the validation results is introduced:

$$\frac{\mathrm{d}^3N_{\phi\phi}}{\mathrm{d}y\mathrm{d}\mathrm{p_T}\phi_1\mathrm{d}\mathrm{p_T}\phi_2}=\frac{\mathrm{d}^3N^{\mathrm{RES}}_{\phi\phi}}{\mathrm{d}y\mathrm{d}\mathrm{p_T}\phi_1\mathrm{d}\mathrm{p_T}\phi_2}=\frac{\mathrm{N}^{\mathrm{RES}}(\mathrm{p_T}\phi_1,\mathrm{p_T}\phi_2)}{\mathrm{N_{events}}\times\Delta y\times\Delta\mathrm{p_T}\phi_1\times\Delta\mathrm{p_T}\phi_2} \tag{3.19}$$

$$\frac{\mathrm{d}^3N^{\mathrm{RAW}}_{\phi\phi}}{\mathrm{d}y\mathrm{d}\mathrm{p_T}\phi_1\mathrm{d}\mathrm{p_T}\phi_2}=\frac{\mathrm{N}^{\mathrm{RAW}}(\mathrm{p_T}\phi_1,\mathrm{p_T}\phi_2)}{\mathrm{N_{events}}\times\Delta y\times\Delta\mathrm{p_T}\phi_1\times\Delta\mathrm{p_T}\phi_2} \tag{3.20}$$

Signal extrapolation

The extrapolation process is analogous to the one used in the inclusive ϕ-meson analysis, but as was the case of the signal extraction the best way forward is to break down the fit procedure into two steps.

The result of the signal extraction is a 2-Dimensional yield (Fig. 3.6). As was the case for the 2-Dimensional invariant mass fit, the number of free parameters is quite high, and does not relate favorably with the available points. A possible way

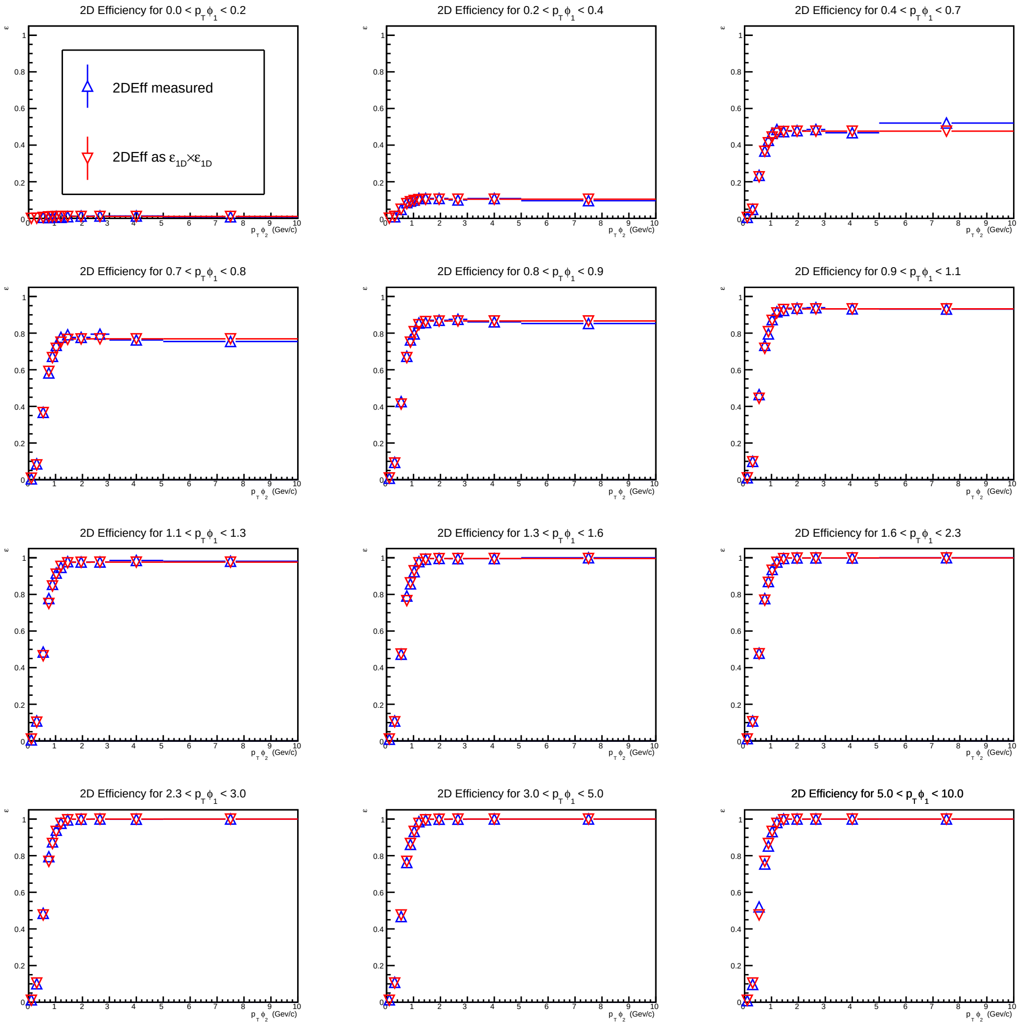

FIGURE 3.5: Comparison between the 2D acceptance and the composite 1D×1D acceptance (see text for reference).

forward is the introduction of the simple differential ϕ-meson pair yield, defined as:

$$\frac{\mathrm{d}^2 N_{\phi\phi}}{\mathrm{d}y\mathrm{d}\mathrm{p}_\mathrm{T}\phi_2} = \int_0^{0.4} f_{\text{L-T}}(\mathrm{p}_\mathrm{T}\phi_1, n, T, m)\mathrm{d}\mathrm{p}_\mathrm{T}\phi_1\Big|_{\mathrm{p}_\mathrm{T}\phi_2} + \sum_{i=1}^{\mathrm{N_{bins}}} H(\mathrm{p}_{\mathrm{T},i}\phi_1, \mathrm{p}_{\mathrm{T},j}\phi_2)\Delta \mathrm{p}_{\mathrm{T},i}\phi_1\Big|_{\mathrm{p}_{\mathrm{T},j}\phi_2} \tag{3.21}$$

where it is meant that the simple differential spectrum in $\mathrm{p}_\mathrm{T}\phi_2$ is, for each p_T bin, built from the measurement and extrapolation of the double conditional ϕ-meson pair yield fixing $\mathrm{p}_\mathrm{T}\phi_2$. After this new differential yield is obtained, the fit procedure can be reiterated as if this was the inclusive yield:

$$\frac{\mathrm{d}N_{\phi\phi}}{\mathrm{d}y} = \int_0^{0.4} f_{\text{L-T}}(\mathrm{p}_\mathrm{T}\phi_2, n, T, m)\mathrm{d}\mathrm{p}_\mathrm{T}\phi_2 + \sum_{j=1}^{\mathrm{N_{bins}}} H(\mathrm{p}_{\mathrm{T},j}\phi_2)\Delta \mathrm{p}_{\mathrm{T},j}\phi_2 \tag{3.22}$$

This methodology simplifies the fit procedure to obtain the extrapolated yield and is the one used in this analysis.

3.3 Validation

The validation process consists in feeding a Monte Carlo sample to the analysis program and comparing the results to the Monte Carlo truth. This is a way to establish the methods are working as they should and is a first quantifier of the goodness and precision of the analysis, together with the feasibility of the measurement. The relevant quantity for the analysis to be able to reproduce are the final yields for the inclusive production of ϕ mesons and the production of ϕ-meson pairs, nevertheless some more steps in the overall validation are a useful exercise to confirm the good performance of the overall technique.

Signal Extraction and Signal Correction To evaluate the goodness of the signal extraction alone, we can compare the integrated yield over the 0.4 GeV/c threshold in transverse momentum to the Monte Carlo truth (3.2).

A more thorough bin by bin comparison of both the yield (Res) and signal extraction can be found in Figures from 3.6a to 3.15. There, the yields of the whole 2-Dimensional spectra are compared, at the raw yield level and at the corrected yield level (Res). To better visualize this, the conditional yields are reported with their ratio to the Monte Carlo truth.

	Raw (Data)	Rec (MC Truth)	Ratio (Data/MC)
1D yield	$1.2440(17)\times10^{-2}$	$1.2395(6)\times10^{-2}$	1.0036(18)
2D yield	$8.157(10)\times10^{-4}$	$8.17(5)\times10^{-4}$	1.002(7)
	Res (Data)	Tru (MC Truth)	Ratio (Data/MC)
1D yield	$3.1115(9)\times10^{-2}$	$3.122(4)\times10^{-2}$	1.003(2)
2D yield	$1.787(5)\times10^{-4}$	$1.786(10)\times10^{-4}$	1.000(8)

TABLE 3.2: Yields for $p_\mathrm{T} \geq 0.4$ from the analysis and from the MC truth and their ratio.

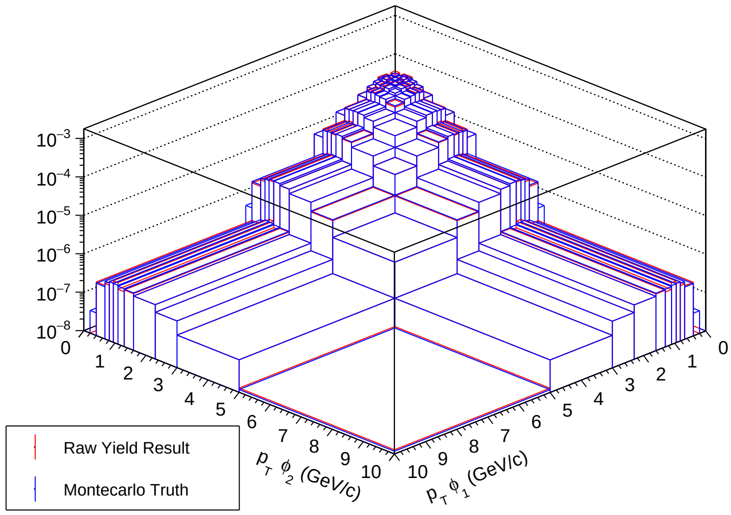

(A) Overlap of the 2-Dimensional Raw Measured Spectrum of results and Monte Carlo truth.

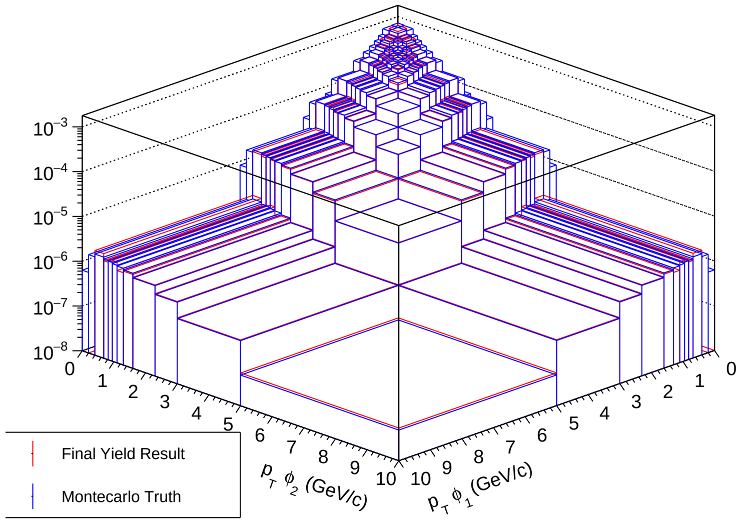

(B) Overlap of the 2-Dimensional Res Spectrum of results and Monte Carlo truth.

FIGURE 3.6: Overlap of the 2-Dimensional Raw and Res Spectra of results and Monte Carlo truth.

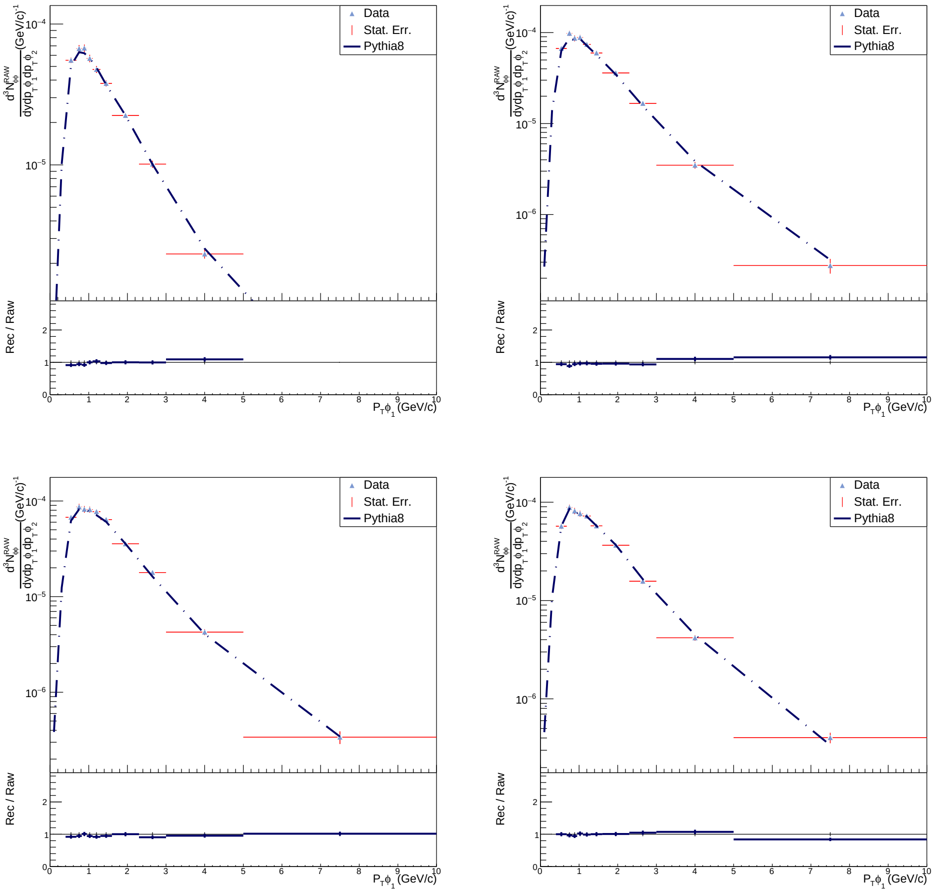

FIGURE 3.7: Comparison of Raw yields (Raw) with Pythia 8 Monte Carlo Truth, with their ratio. From top left to bottom right the results are the conditional yields for p_T [0.4-0.68], [0.68-0.82], [0.82-0.95]. [0.95-1.1]

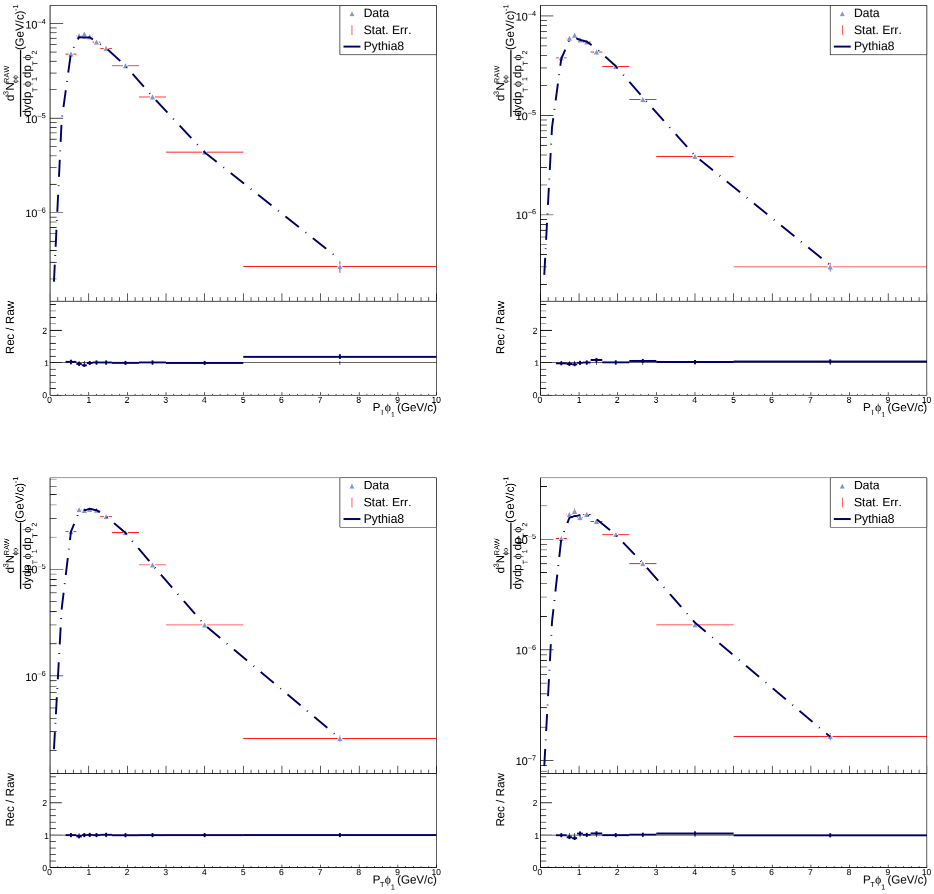

FIGURE 3.8: Comparison of Raw yields (Raw) with Pythia 8 Monte Carlo Truth, with their ratio. From top left to bottom right the results are the conditional yields for p_T [1.1-1.3], [1.3-1.6], [1.6-2.3]. [2.3-3.0]

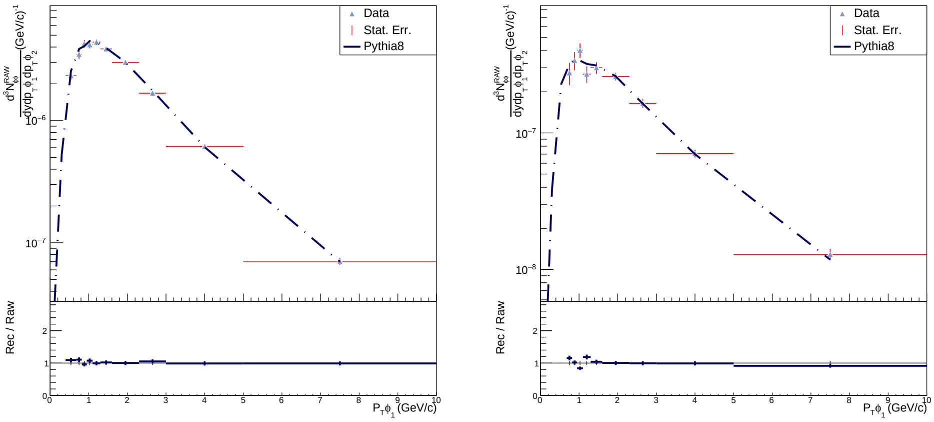

FIGURE 3.9: Comparison of Raw yields (Raw) with Pythia 8 Monte Carlo Truth, with their ratio. From top left to bottom right the results are the conditional yields for p_T [3.0-5.0], [5.0-10.]

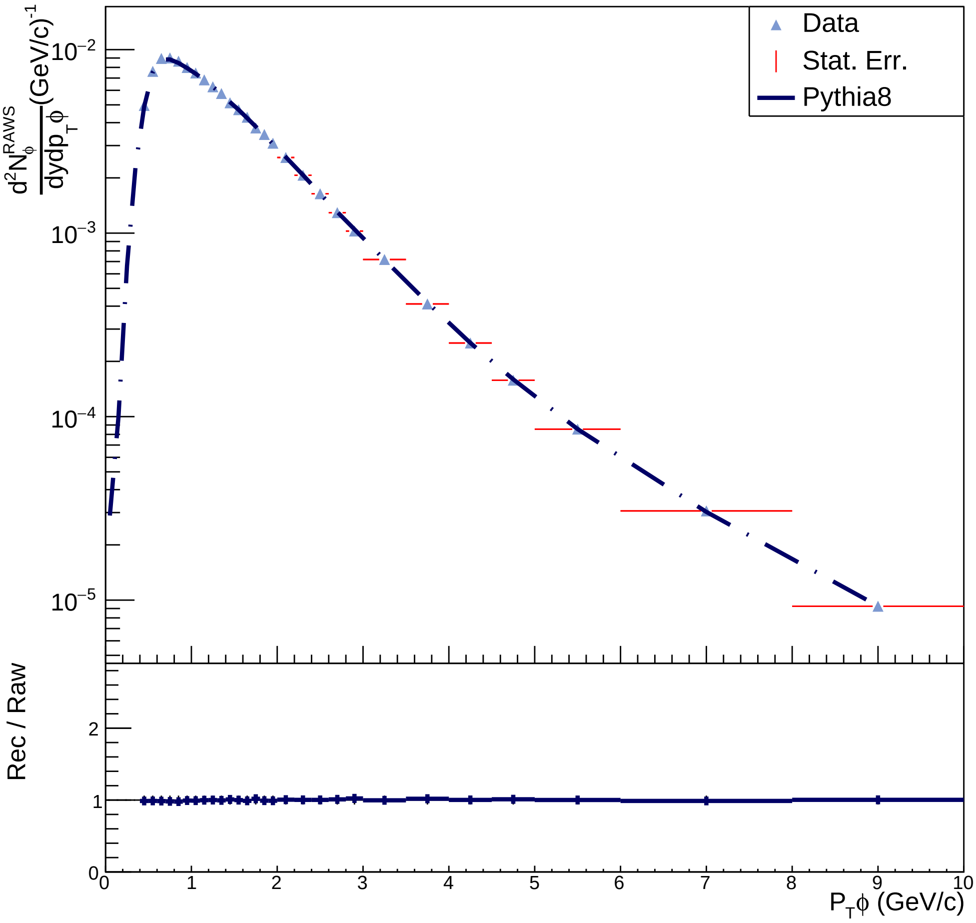

FIGURE 3.10: Comparison of Raw yields (Raw) with Pythia 8 Monte Carlo Truth, with their ratio for the 1-Dimensional yield

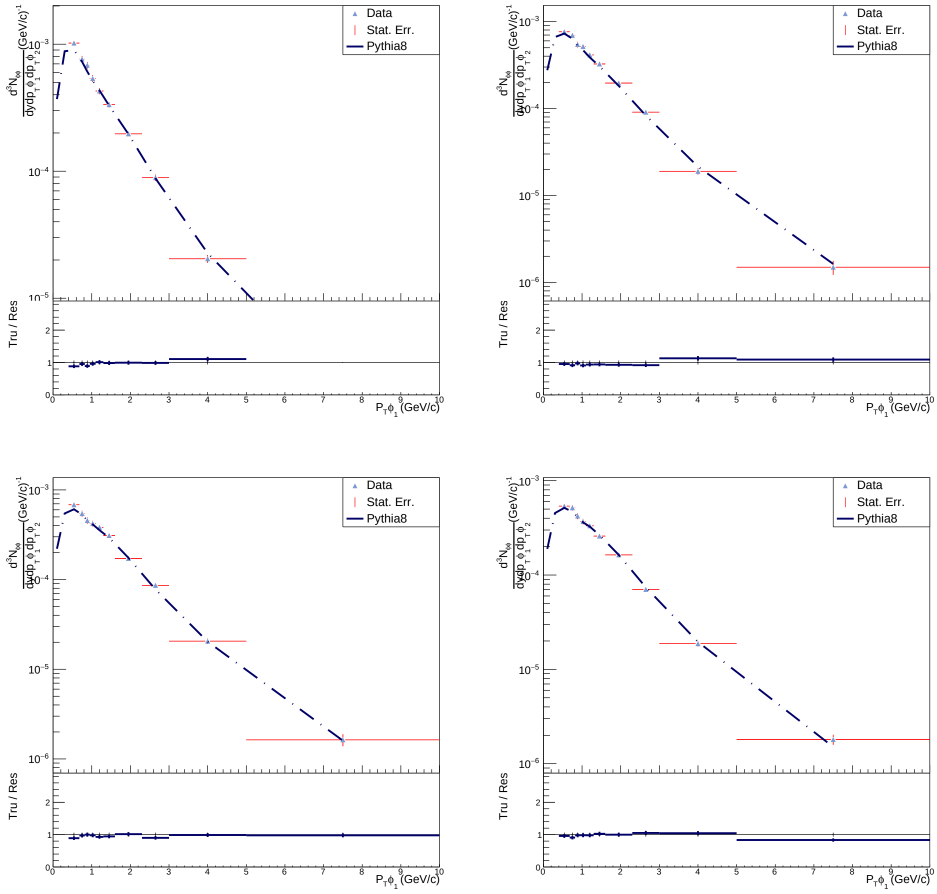

FIGURE 3.11: Comparison of Results (Res) with Pythia 8 Monte Carlo Truth, with their ratio. From top left to bottom right the results are the conditional yields for p_T [0.4-0.68], [0.68-0.82], [0.82-0.95]. [0.95-1.1]

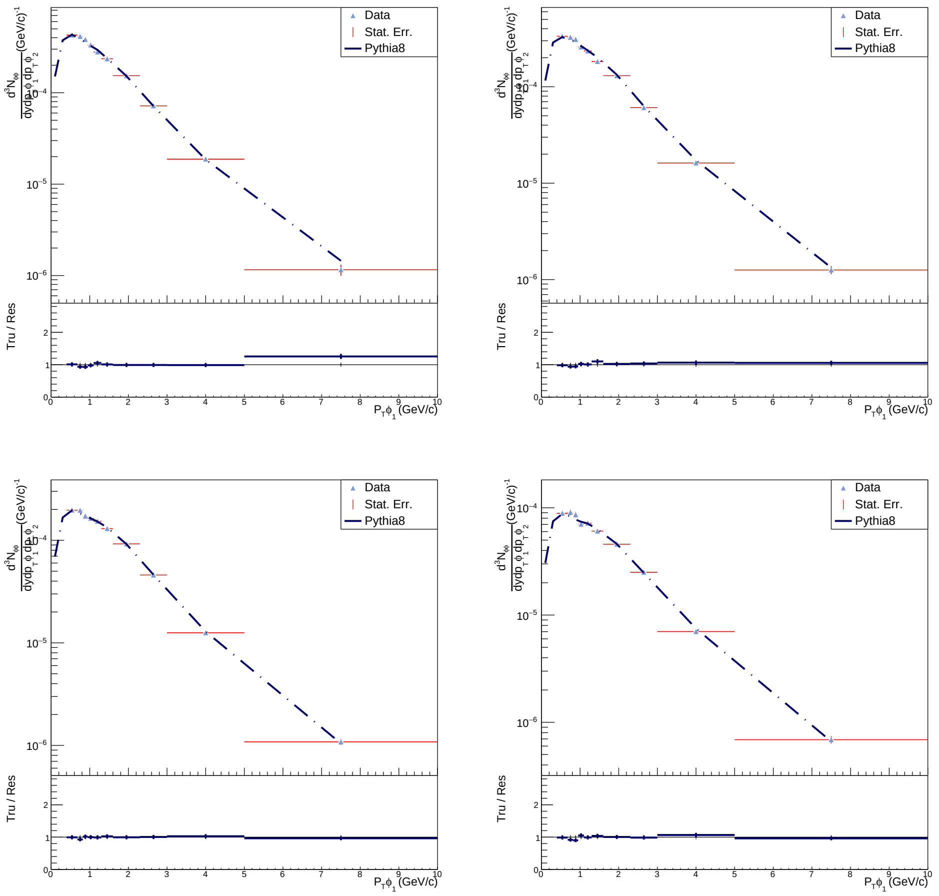

FIGURE 3.12: Comparison of Results (Res) with Pythia 8 Monte Carlo Truth, with their ratio. From top left to bottom right the results are the conditional yields for p_T [1.1-1.3], [1.3-1.6], [1.6-2.3]. [2.3-3.0]

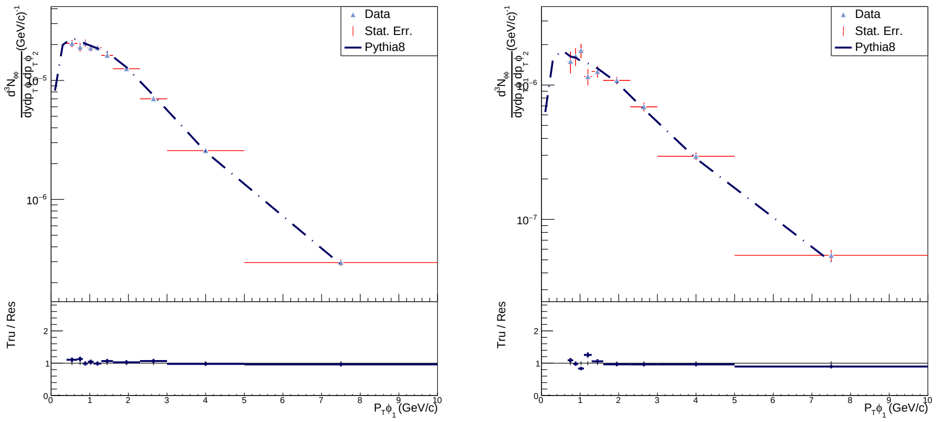

FIGURE 3.13: Comparison of Results (Res) with Pythia 8 Monte Carlo Truth, with their ratio. From top left to bottom right the results are the conditional yields for p_T [3.0-5.0], [5.0-10.]

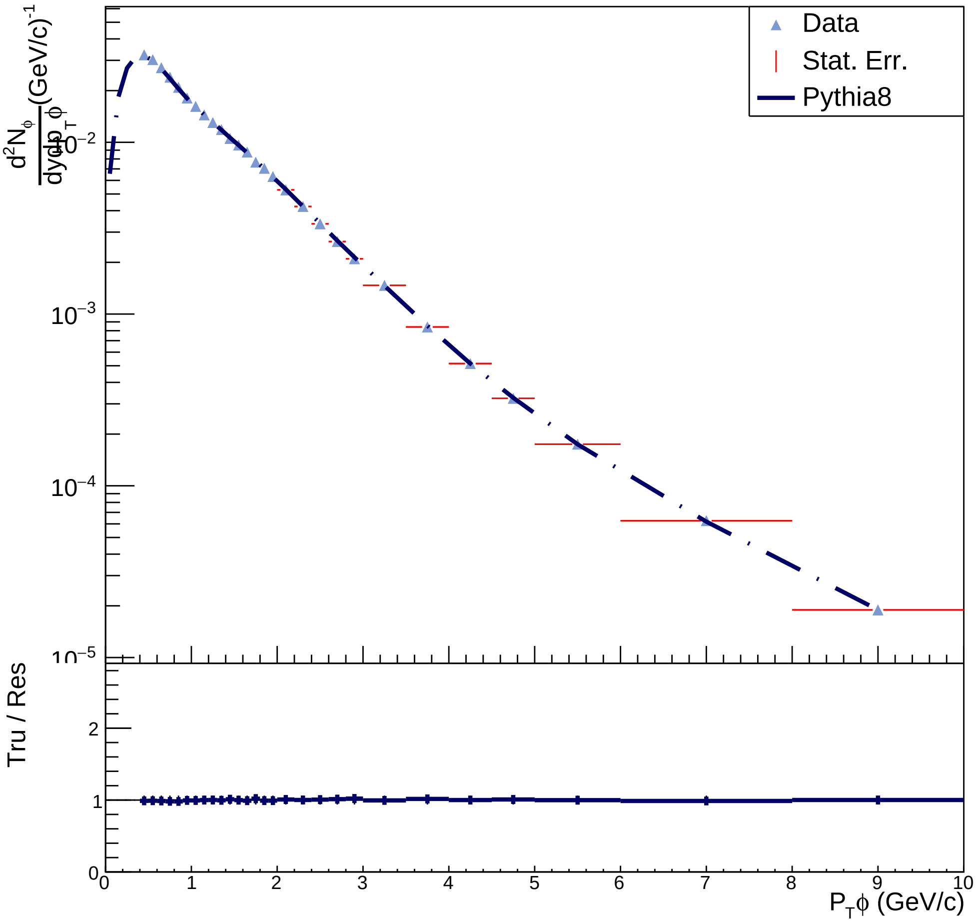

FIGURE 3.14: Comparison of Results (Res) with Pythia 8 Monte Carlo Truth, with their ratio for the 1-Dimensional yield

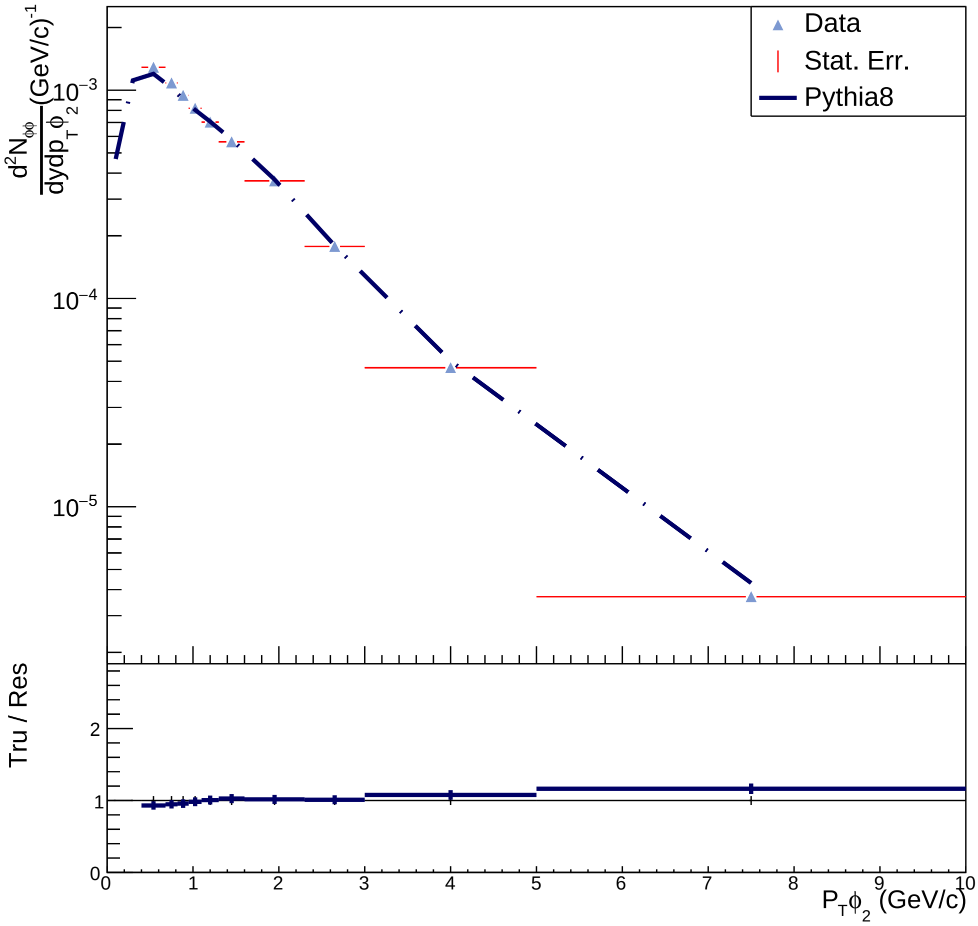

FIGURE 3.15: Comparison of Results with Pythia 8 Monte Carlo Truth, with their ratio. The results are the integrated 2D yields.

Signal Extrapolation To evaluate the goodness of the signal correction, extraction and extrapolation, i.e. of the full technique, we can compare the integrated yield over the full transverse momentum spectrum to the Monte Carlo truth (Tab. 3.3).

	Res	Tru	Ratio
	(Fit)	(MC Truth)	(Fit/MC)
1D yield	$3.945(10)\times10^{-2}$	$3.96(8)\times10^{-2}$	1.003(2)
2D yield	$18.6(4)\times10^{-4}$	$18.613(15)\times10^{-4}$	1.00(2)

TABLE 3.3: Yields from the analysis and from the MC truth and their ratio.

3.4 Final considerations on measured quantities

We have now reviewed the technique by which we can measure the yield of ϕ-meson pairs. Given we can now perform a novel measurement we can try to investigate the statistical properties of the production probability for a ϕ meson that can be inferred with this new information. We can elaborate the inclusive ϕ meson yield and the ϕ meson pair yield results to find the mean and variance of the production distribution. Intuitively, the inclusive production yield ($\mathrm{d}N_{\phi}/\mathrm{d}y$) is the average numbers of ϕ mesons produced per event ($< Y_{\phi} >$).

$$< Y_{\phi} >= \frac{1}{N_{events}} \times \Big(N_{1\phi} + 2N_{2\phi} + 3N_{3\phi} + ...\Big) \tag{3.23}$$

where N_{events} is the number of events and $N_{n\phi}$ is the number of events where n ϕ-mesons are produced. In a similar fashion, holding into account the permutations that come into play when talking about pairs[1]

$$\frac{\mathrm{d}N_{\phi\phi}}{\mathrm{d}y} =< Y_{\phi\phi} >= \frac{1}{N_{events}} \times \Big(N_{2\phi} + 3N_{3\phi} + 6N_{4\phi} + ...\Big) \tag{3.24}$$

Now we can recognize that the fractions $N_{n\phi}/N_{events}$ are indeed the probability to produce exactly n mesons, and we can call them $p_{i\phi}$. We can use this notation to write a more general approach:

$$< Y_{i\phi} >= \sum_{k=0}^{\infty} \binom{k}{i} \times p_{k\phi} = \sum_{k=0}^{\infty} \frac{k!}{i!(k-i)!} \times p_{k\phi} \tag{3.25}$$

The mean and variance of the distribution Mean and variance are two useful informations when talking about statistical distributions, so finding them is surely something desired. The power of this novel analysis is that, contrary to the standard inclusive analysis that can only provide access to the first moment of the distribution (the mean, μ_{ϕ}) of the number of ϕ mesons produced per event the simultaneous measurement of both the inclusive yield ($< Y_{\phi} >$) and of the yield of ϕ-meson pairs ($< Y_{\phi\phi} >$) provides direct information on the second moment of the distribution (the

---

[1] It's easy to imagine this if we have a production of 3 particles: we can measure the pair 1-2, 2-3 and 1-3, thus a weight of 3 is given to the term $N_{3\phi}$

variance, σ_ϕ^2). To this end we can re-arrange the two measured yields as:

$$
\begin{aligned}
< Y_{\phi\phi} > &= \sum_{k=0}^{\infty} \frac{k(k-1)}{2} \times p_{k\phi} = \sum_{k=0}^{\infty} \Big(\frac{k^2}{2} - \frac{k}{2}\Big) \times p_{k\phi} = \frac{1}{2} < Y_\phi^2 > - \frac{1}{2} < Y_\phi > \\
< Y_\phi^2 > &= 2 < Y_{\phi\phi} > + < Y_\phi > \\
< Y_\phi^2 > - < Y_\phi >^2 &= 2 < Y_{\phi\phi} > + < Y_\phi > - < Y_\phi >^2
\end{aligned}
$$

We then successfully found a way to extract the mean and variance of the distribution from the measured yields, as:

$$\mu_\phi =< Y_\phi > \tag{3.26}$$

$$\sigma_\phi^2 = 2 < Y_{\phi\phi} > + < Y_\phi > - < Y_\phi >^2 \tag{3.27}$$

The poissonian distribution hypothesis The poissonian distribution is a natural candidate to describe the statistics of the ϕ-meson production. It is the simple case for which the production is purely statistical without any further correlation. To get a better sense of the statical distribution of the ϕ mesons the poissonian distribution with the mean measured in this analysis, compared to the Pythia Monte Carlo generators is reported in Figure 3.16.

We are then interested in quantifying the deviation of the production probability variance with respect to the poissonian hypothesis. To this end we can introduce a new parameter (γ_ϕ) defined as:

$$\gamma_\phi = \frac{\sigma_\phi^2}{\mu_\phi} - 1 \tag{3.28}$$

$$\rightarrow \frac{\sigma_\phi^2}{\mu_\phi} = 1 = \frac{2<Y_{\phi\phi}>}{<Y_\phi>} + \frac{<Y_\phi>}{<Y_\phi>} - \frac{<Y_\phi>^2}{<Y_\phi>}$$

$$\rightarrow \frac{\sigma_\phi^2}{\mu_\phi} - 1 = \frac{2<Y_{\phi\phi}>}{<Y_\phi>} - < Y_\phi > \tag{3.29}$$

If this parameter can be measured with enough precision, it can certainly give a quantifiable measurement of the correlation or anti-correlation of the ϕ-meson production statistics. Another parameter that can help us define the statistics of the ϕ meson production is the ratio of yields, defined as:

$$\frac{<Y_{\phi\phi}>}{<Y_\phi>^2} \rightarrow \sigma_\phi^2 = \mu_\phi \rightarrow \frac{\sigma_\phi^2}{<Y_\phi>^2} = \frac{\mu_\phi}{<Y_\phi>^2} \tag{3.30}$$

$$\rightarrow \frac{2<Y_{\phi\phi}>+<Y_\phi>-<Y_\phi>^2}{<Y_\phi>^2} = \frac{<Y_\phi>}{<Y_\phi>^2} \rightarrow \frac{2<Y_{\phi\phi}>}{<Y_\phi>^2} + \frac{1}{<Y_\phi>} - 1 = \frac{1}{<Y_\phi>}$$

$$\rightarrow \frac{2<Y_{\phi\phi}>}{<Y_\phi>^2} = 1 \rightarrow \frac{<Y_{\phi\phi}>}{<Y_\phi>^2} = \frac{1}{2} \tag{3.31}$$

where the expectation value for a purely poissonian distribution is 1/2.

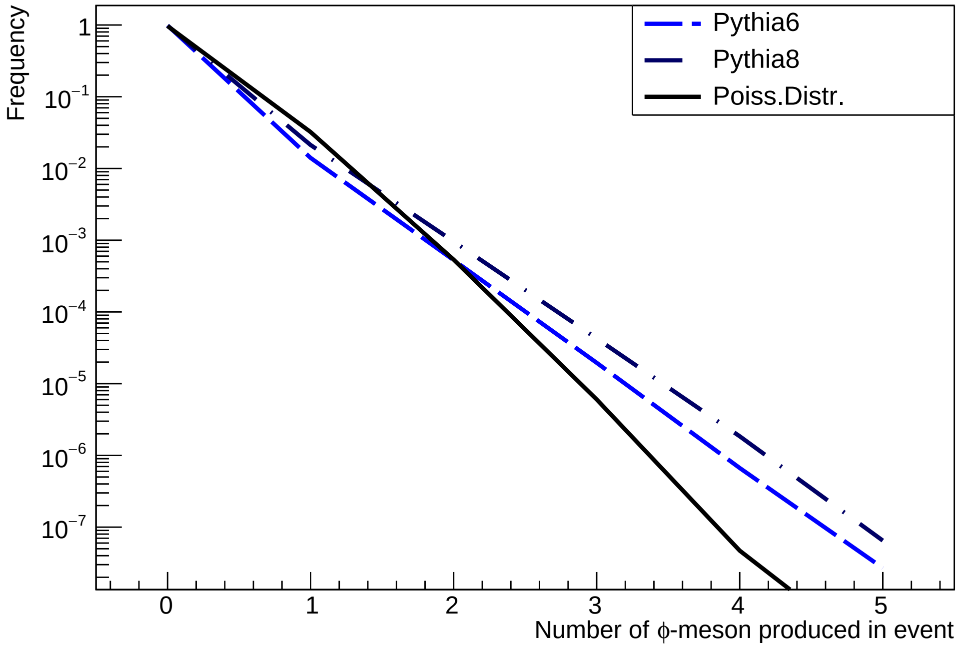

FIGURE 3.16: Comparison between the simple poissonian distribution, with the inclusive ϕ meson yield as mean, with Pythia generators

Chapter 4

Analysis on ALICE Data

This chapter describes the application of the analysis technique developed in this thesis. A limited dataset was used as a first sample to get preliminary results for the measurement of the production of the yield of ϕ-meson pairs in inelastic pp collisions at the LHC.
The approach for the analysis of the data collected by ALICE will follow the steps described in the previous chapter. The first results of the measurement on ALICE data collected in pp collisions at 7 TeV are presented, together with a first estimate of the associated systematic uncertainties.

4.1 Adapting the analysis to the real data

The application of the technique on a real dataset means there are a few considerations that need to be taken into account.

The core methodologies will essentially stay the same as the ones used on the Monte Carlo generated events, such as the signal extraction procedures. Nevertheless a number of steps must be taken to ensure that the real dataset is on target for the analysis. A first example of this concept is particle identification: the real dataset does not provide a perfect unique identification of the tracks, and thus one must decide how stringent the selection should be, finding a good balance between purity and an acceptable statistics. Even the event selection becomes an important matter, where the trigger must select real events and discard non beam-beam interactions or other types of non-relevant events, with some inefficiency that must be accounted for. In the next chapter we will describe the selections used in [34], that will also be used in our analysis:

1. Data selection:
   As we discussed in Chapter 2, the detector evolves in time, meaning that performance, acceptance and resolution may not be, and they are in no way so, perfectly constant in time. In this thesis the choice of the 2010 data taking period was done to follow the publication the analysis is based on.

2. Event selection:
   The event selection is performed for a number of reasons, such as the reconstructed vertex quality.

3. Track and PID selection:
   The track selection, correlated to the PID, is the part of the selection sensitive to the quality of the reconstructed properties and to the statistics available for the analysis. As mentioned before, here a balance is made between the two.

On top of these selections, we must consider that the detectors have another intrinsic efficiency represented by the geometrical acceptance. These selections greatly affect the results both in terms of corrections and in terms of systematic uncertainty.

4.1.1 Data Selection

The data taking process involves reading the data produced by the detectors that compose the experiment. Given the complexity of the ALICE experiment in terms of sub-detectors components, it is natural to expect variations in the performance over time. As an example dedicated measurements are made to determine temperature and pressure, both of which can affect the detector response. The online calibration, i.e. the one performed simultaneously with the data taking marks the first pass of the data calibration. Following passes are used to further calibrate offline the detectors. For this reason the datasets are clustered in Runs, that is periods of data taking originating from the same beams, circulating in the accelerator for several hours until they are too degraded and subsequently dumped.

These runs are characterised by numerous parameters that define their overall quality and the operational status of the detectors. For example a run may be recorded without the HMPID detector working because of a maintenance stop. Conversely a whole batch of runs may have lower resolution on the track reconstruction because the TPC had an electronics malfunction, recording data requiring an additional calibration to correct for possible distortions.

For these reasons a quality check tool is available at the ALICE collaboration. All runs are listed with their active detectors and overall qualities, together with comments indicating the status of the reconstruction and any problems that may have occurred or the corrections that were applied.

The analysis was performed on the Runs listed in Table 4.1, with the requirements specified in Table 4.2.

4.1.2 Event Selection

The analysis used a dataset recorded with a Minimum Bias Trigger, that requires a single hit in the SPD detector or in one of the two VZERO counters, i.e. at least one charged particle anywhere in 8 units of pseudorapidity, associated to the requirement of two proton bunches actually colliding at the same time.

Once the event is selected, a requirement on the position of the primary vertex is applied. As we have seen in Chapter 2, the information of vertex position greatly increase the momentum resolution (Fig. 2.12) and the primary track identification (Fig. 2.11). It is therefore important to select events for which the primary vertex is correctly reconstructed. The first requirement is that the SPD correctly reconstructed a vertex. Secondly the more general approach which uses fully-reconstructed tracks (Sect. 2.2) is taken into consideration. If no vertex is found with reconstructed tracks, the SPD reconstructed vertex is taken. Conversely, if the track-vertex is available, its location is compared to the one of the SPD vertex: if their z coordinate is more than $0.5\,\mathrm{cm}$ apart from each other, the event is discarded. If the distance is within the limit, the vertex reconstructed by the track method is considered.

Once the vertex candidate is available, a cut on its z coordinate is performed, to only accept events that are within $-10\,\mathrm{cm} < z < 10\,\mathrm{cm}$. This selection helps to keep the particles produced in the event in a fiducial acceptance region, as we are discarding the interactions that were furthest from the nominal interaction point along the beam pipe.

Data Taking period	Run List
LHC10b	117222, 117220, 117116, 117112, 117099, 117092, 117063, 117060, 117059, 117053, 117052, 117050, 117048, 116645, 116643, 116574, 116571, 116562, 116403, 116402, 116288, 116102, 116081, 116079, 115414, 115401, 115399, 115393, 115345, 115335, 115328, 115322, 115318, 115310, 115193, 115186, 114931, 114930, 114924, 114918, 114798, 114786
LHC10c	121040, 121039, 120829, 120825, 120824, 120823, 120822, 120821, 120758, 120750, 120741, 120671, 120617, 120616, 120505, 120503, 120244, 120079, 120076, 120073, 120072, 120069, 120067, 119862, 119859, 119856, 119853, 119849, 119846, 119845, 119844, 119842, 119841, 118561, 118560, 118558, 118556, 118518, 118506
LHC10d	126158 , 126097, 126090, 126088, 126082, 126081, 126078, 126073, 126008, 126007, 126004, 125855, 125851, 125850, 125849, 125848, 125847, 125844, 125843, 125842, 125633, 125632, 125630, 125628, 125296, 125134, 125101, 125100, 125097, 125085, 125083, 125023, 122375, 122374
LHC10e	130850, 130848, 130847, 130844, 130842, 130840, 130834, 130799, 130798, 130795, 130793, 130704, 130696, 130628, 130623, 130621, 130620, 130609, 130608, 130524, 130520, 130519, 130517, 130481, 130480, 130479, 130375, 130178, 130172, 130168, 130158, 130157, 130149, 129983, 129966, 129962, 129961, 129960, 129744, 129742, 129738, 129736, 129735, 129734, 129729, 129726, 129725, 129723, 129666, 129659, 129653, 129652, 129651, 129650, 129647, 129641, 129639, 129599, 129587, 129586, 129540, 129536, 129528, 129527, 129525, 129524, 129523, 129521, 129520, 129514, 129513, 129512, 129042, 128913, 128855, 128853, 128850, 128843, 128836, 128835, 128834, 128833, 128824, 128823, 128820, 128819, 128778, 128777, 128678, 128677, 128621, 128615, 128611, 128609, 128605, 128582, 128506, 128505, 128504, 128503, 128498, 128495, 128494, 128486

TABLE 4.1: List of the Runs used in the Analysis

Event selection	pass	Global Quality	Required Working detectors
	4	1 (Best)	TOF, TPC, V0, T0
Vertex selection	$-10\,\mathrm{cm} < z < 10\,\mathrm{cm}$		
Track selection	Detectors	Topology	Kinematics
	TPC+ITS	Tight DCA Filter 5	$p_T \leq 0.15$ GeV/c $-0.8 < \eta < 0.8$
PID selection	Status	Detector	PID cuts
	Available	TPC	$\Delta S^{\mathrm{K}}_{\mathrm{particle}} \leq 3\sigma_{\mathrm{TPC}}$
	Not Available	TOF	$\backslash$
	Available	TPC	$\Delta S^{\mathrm{K}}_{\mathrm{particle}} \leq 5\sigma_{\mathrm{TPC}}$
	Available	TOF	$\Delta S^{\mathrm{K}}_{\mathrm{particle}} \leq 3\sigma_{\mathrm{TOF}}$

TABLE 4.2: List of the requirements for the Analysis.

4.1.3 Track Selection

The track selection is used to ensure the quality of the reconstructed tracks and therefore enhance the precision of the analysis. The selection is performed to only keep the best quality tracks; firstly the Filterbit for the track is considered. The Filterbit is a preset filter that flags the track quality and properties. The one used in this analysis is the Filterbit 5, that indicates:

1. The track has passed standard TPC + ITS quality cuts, as mentioned in Section 2.2.2.

2. The track has passed the tight DCA cut for primary particles.

Moreover, the track is requested to have the same kinematic cuts we introduced in the Monte Carlo analysis (Ch. 3), namely $p_T \geq 0.15$ GeV/c and $-0.8 < \eta < 0.8$.

These cuts are necessary to exclude low transverse momentum tracks, that are likely compromised by material interactions or can be trapped in the magnetic field, even if they are measured they potentially have low efficiencies and precision (Fig. 2.10). Moreover the cut in pseudo-rapidity is applied in order to accept tracks that are well inside the TPC+ITS fiducial region for reconstruction ($-0.9 < \eta < 0.9$).

The tight DCA cut requires the distance between the vertex and the track PCA along z to be $|d_{0,z}| < 2\,\mathrm{cm}$, whereas their mutual distance on the $x-y$ plane is requested to be $d_{0,xy} <$ (0.0182 + 0.0350 GeV/c p_T cm. This cut is used to enhance (Fig. 2.11) the primary particle fraction of the reconstructed tracks, as we are looking for a meson with a short decay time, meaning it will not be distinguishable from primary particles that are promptly emitted from the primary interaction.

4.1.4 Particle Identification

Particle identification is a complex subject, the procedures and performance of the ALICE experiment were the subject of Section 2.3. For the presented analysis Particle Identification was performed using the TPC and TOF signals. First a check on the status of the PID for the track is done for both detectors, then the signal is compared to the expected signal for the kaon mass hypothesis and a related σ_{detector} is given. This quantity represents the standard deviation of the particle signal (S_{particle}) with respect to the expected signal for a track in the kaon mass hypothesis (S_K). The selection is then made using their difference ($|S_{\text{particle}} - S_K| = \Delta S^{K}_{\text{particle}} \leq n\sigma_{\text{detector}}$).

For the kaon identification we require that the TPC is working correctly and the signal is at least within $\Delta S^{K}_{\text{particle}} \leq 5\sigma_{\text{TPC}}$ (Fig. 4.1d). After this requirement is met, a check on the TOF is made to see if the time-of-flight measurement is available and is at least within $\Delta S^{K}_{\text{particle}} \leq 3\sigma_{\text{TOF}}$ (Fig. 4.1c). TOF signal may be lacking due to the distance of the detector from the vertex combined with the presence of a magnetic field: low p_T particles will be deflected and trapped in the typical helicoidal motion in the magnetic field. If the TOF signal is not available, the requirement for the TPC PID is made more stringent by requiring $\Delta S^{K}_{\text{particle}} \leq 3\sigma_{\text{TPC}}$ (Fig. 4.1d).

4.1.5 Signal Extraction

The signal extraction process used is the one described in Section 3.2.1 and 3.2.2. Even though the underlying process is analogous, some thought should be given approaching real data. Notably the signal function is a Voigtian rather than the previously used Breit-Wigner. This effect arises from the momentum uncertainties. The

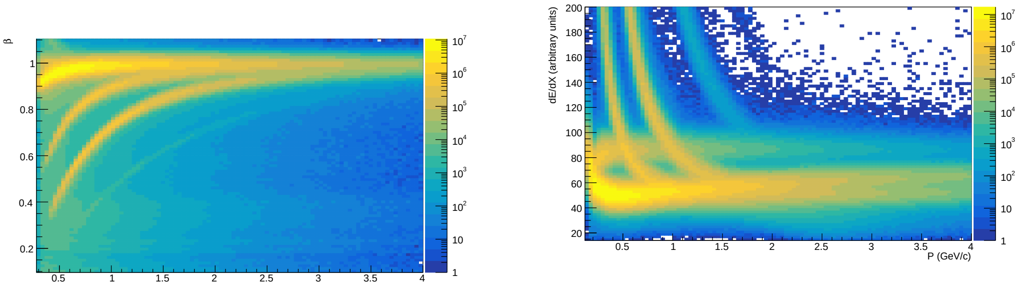

(A) Particle velocity measured by the TOF detector as a function of momentum

(B) Particle energy loss dE/dx (arbitrary units) measured by the TPC detector as a function of momentum

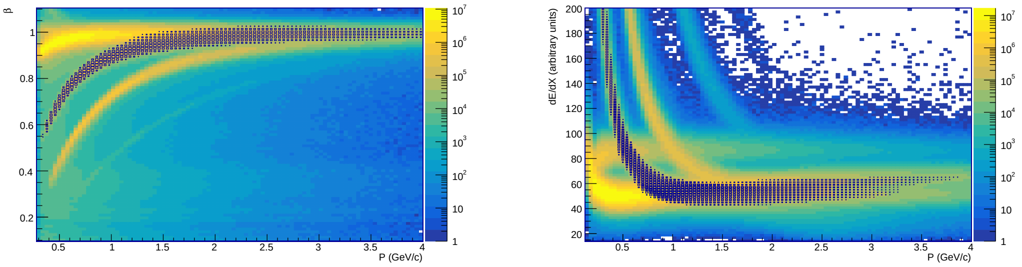

(C) Figure 4.1a (above) with a superimposition of the particles selected by this analysis PID cut on TOF signal.

(D) Figure 4.1b (above) with a superimposition of the particles selected by this analysis two PID cuts on TPC signal, combined.

FIGURE 4.1: Particle identification performance of the TOF and TPC detectors and kaon selections used in this analysis

Voigtian is indeed a convolution of a Gaussian and a Breit-Wigner., hence it represents a resonance signal affected by instrumental resolution effects. Some examples of the results of these fits can be found in Figure 4.2 for the 1-Dimensional spectra and in Figure 4.3 for the 2-Dimensional spectra.

4.1.6 Corrections to the Raw yield

The corrections to the raw yield used are the ones described in Section 3.2.1 and 3.2.2. In addition to those already discusse in the Monte Carlo analysis, we must add some others. The main guideline we follow is the one laid down in [34]. To measure the efficiencies and acceptances a Monte Carlo simulation with Pythia6 anchored to the selected runs was used. The anchored Monte Carlo is a simulation performed via an accurate Geant3 description of the detector and its precise conditions in the given run, to achieve a reliable measurement for the efficiency. The dataset used was the LHC14j4 b, c, d, e, f with the same runs listed in Table 4.1. The Result yield is calculated as was performed in Chapter 3, with the addition of the detector acceptance ($\varepsilon' = \varepsilon \times \mathrm{A}$). This is the first step toward a proper correction of the yield on real data. The combination of track efficiency and detector acceptance for the 1-Dimensional analysis and as a comparison for the 2-Dimensional analysis (see 3.2.2), can be seen in Figures 4.4 and 4.5. Secondly we must introduce other corrections [34] to account for:

$\varepsilon_{\mathrm{trg}}$ The correction for the trigger efficiency in terms of lost events.
This correction is evaluated to be 85.2%$^{+6.2}_{3.0}$.

$\varepsilon_{\mathrm{res}}$ The correction for the trigger efficiency in terms of lost resonances.
This loss is evaluated to be $\approx 1\%$, so the correction should be 99%.

$\varepsilon_{\mathrm{vrt}}$ The correction for the vertex acceptance, given we cut out vertices reconstructed outside a fiducial interval of $10\,\mathrm{cm}$. This loss is evaluated to be negligible.

These corrections redefine the differential yields as:

$$\frac{\mathrm{d}^2 N_\phi}{\mathrm{d}y\mathrm{dp_T}}(\mathrm{p_T}) = \frac{\mathrm{N^{RES}}(\mathrm{p_T}) \times \varepsilon_{\mathrm{trg}}}{\mathrm{N_{events}} \times \Delta y \times \Delta \mathrm{p_T} \times \varepsilon_{\mathrm{res}}} \tag{4.1}$$

and the double differential yields as:

$$\frac{\mathrm{d}^3 N_{\phi\phi}}{\mathrm{d}y\mathrm{dp_T}\phi_1\mathrm{dp_T}\phi_2}(\mathrm{p_T}\phi_1, \mathrm{p_T}\phi_2) = \frac{\mathrm{N^{RES}}(\mathrm{p_T}\phi_1, \mathrm{p_T}\phi_2) \times \varepsilon_{\mathrm{trg}}}{\mathrm{N_{events}} \times \Delta y \times \Delta \mathrm{p_T}\phi_1 \times \Delta \mathrm{p_T}\phi_2 \times \varepsilon_{\mathrm{res}}} \tag{4.2}$$

4.1.7 Signal extrapolation

Signal extrapolation is performed with the methodology described in the previous chapter. Some examples of fit results are shown in Figures 4.6-4.7 to highlight the good description of the Levy function in the measured region.

The main difference in this regard, when operating on the real data, is the extend extrapolation for the bins $\mathrm{p_T}\phi_{1,2}$ [5.0-10] and $\mathrm{p_T}\phi_{1,2}$ [0.40-0.68] GeV/c. In fact these do not have enough statistics to get a reliable signal extraction, and to account for the missing yield an extension of the extrapolation is performed.

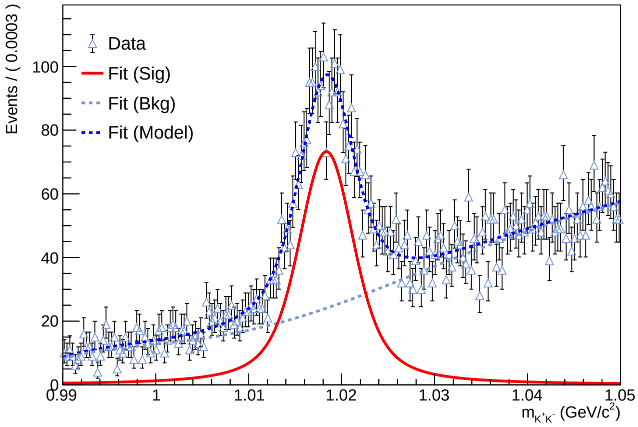

(A) 1-Dimensional K^+K^- Invariant Mass histograms with fit results highlighted, for ϕ meson p_T in [0.4-0.5] GeV/c.

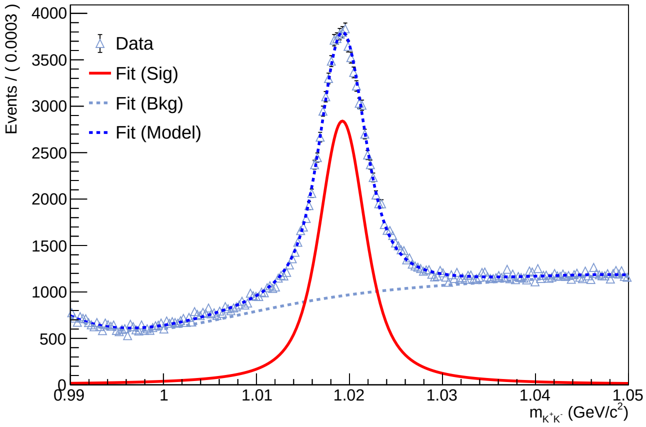

(B) 1-Dimensional K^+K^- Invariant Mass histograms with fit results highlighted, for ϕ meson p_T in [1.0-1.1] GeV/c.

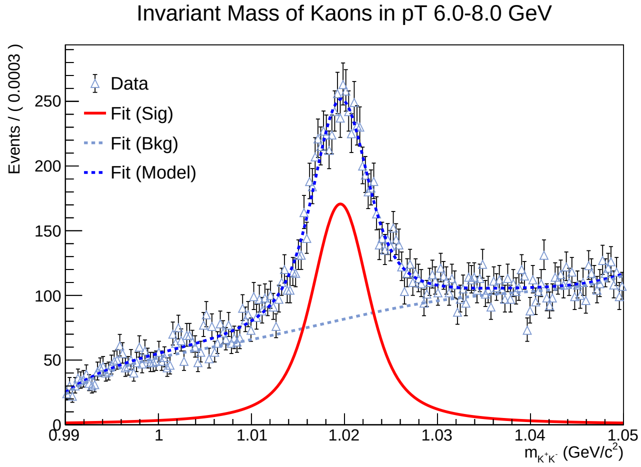

(C) 1-Dimensional K^+K^- Invariant Mass histograms with fit results highlighted, for ϕ meson p_T in [6.0-8.0] GeV/c.

FIGURE 4.2: Examples of 1-Dimensional K^+K^- Invariant mass histograms with fit results highlighted: red line is the signal, dashed blue line is the background and blue line is the full model.

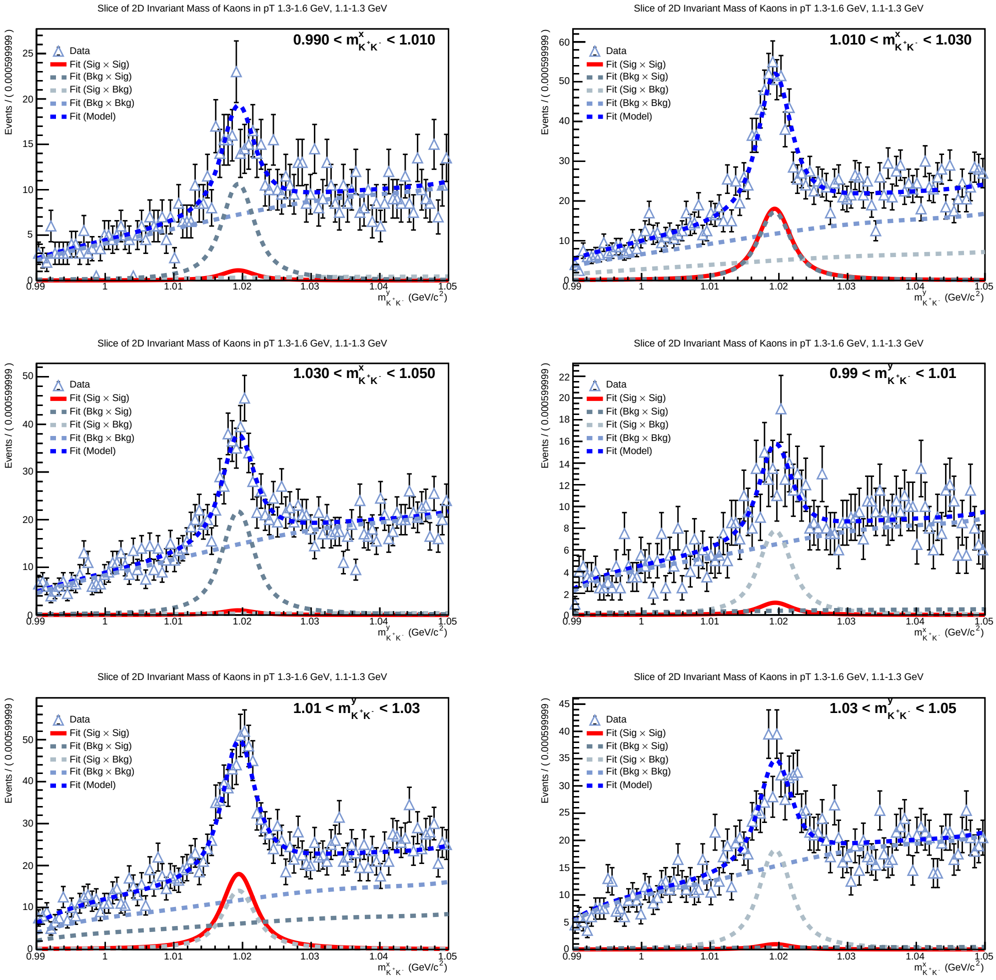

FIGURE 4.3: Projections of one 2-Dimensional Invariant mass histogram fitted, with Fit components highlighted. The lines show the corresponding projections of the 2D fits.

4.1.8 Systematic errors

Systematic errors are used to account for all the uncertainties that are not strictly statistical. In the present text we will rely on [34] for several contributions to this uncertainty. We can assume that the values for the systematic uncertainties estimated there can be inherited and used also for the presented analysis. This choice was made on the basis of the fact that this analysis follows closely the choices presented in the above publication. Moreover the data taking period is the same. In particular we will take from the publication their values for the systematic uncertainties:

1. Efficiency and Track selection: 8%.
2. Particle Identification: 1.5%.

These values are generalised in the 2-Dimensional analysis making the reasonable assumption that the matching of two ϕ mesons will simply multiply the uncertainty by a factor of 2.

It should be noted that the evaluation on the extrapolated yield is not performed in this work , nor it will be inherited by the publication.

As far as the signal extraction is concerned, we attempt a first estimate in the

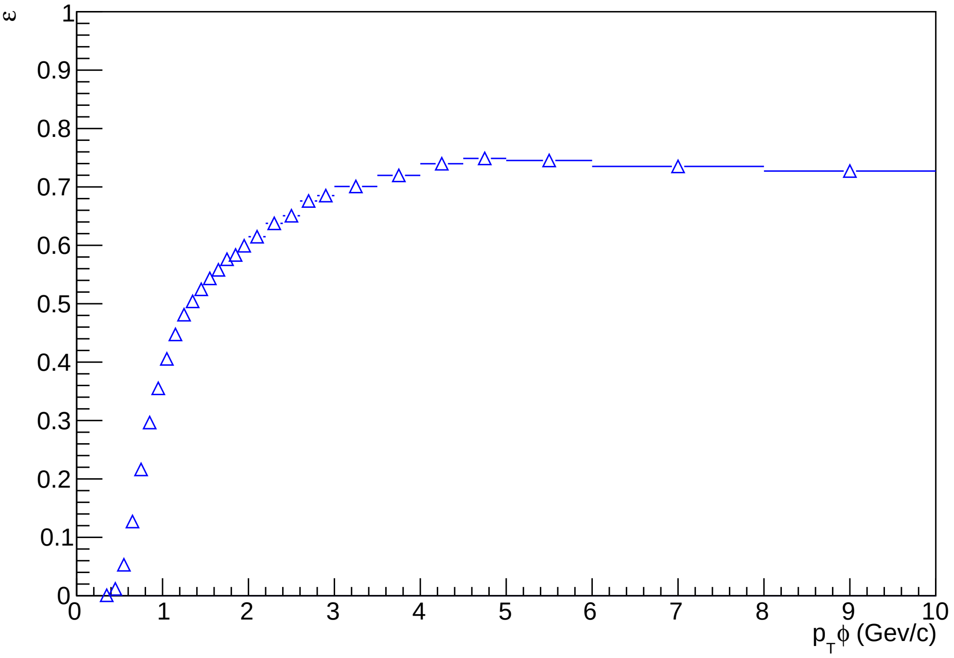

FIGURE 4.4: Inclusive ϕ-meson reconstruction efficiency as a function of pT.

following. The signal extraction systematics have not been inherited and have been evaluated in this thesis. Moreover the signal extraction from the 2-Dimensional histograms is a completely novel technique for which an evaluation of the systematics is valuable at this stage.
Recalling that the default fit set up is taken to be:

1. The ϕ meson mass and width are let free to vary within 10% of the PDG reported value [11].
2. The Chebyshev polynomials coefficients are let free to vary in [-1,+1].
3. The invariant mass fit region is taken to be [0.99,1.05] GeV/c^2.

   In addition to those, the Voigtian introduces:

4. The resolution parameter is let free to vary in [0.00,1.00] GeV/c.

To understand how these arbitrary assumption affect the results, we can repeat the analysis using the following assumptions:

1. Mass and width of the resonance are (in turn) fixed to the PDG value.
2. The background can be represented by a fifth or third degree Chebyshev polynomial.
3. A number of different ranges to fit the data can be used.

Once the signal extraction is repeated for each variation, the result is saved in terms of relative deviation from the standard fit, in percentage, for each bin for which we measure the yield directly. A summary of the standard fit procedure together with

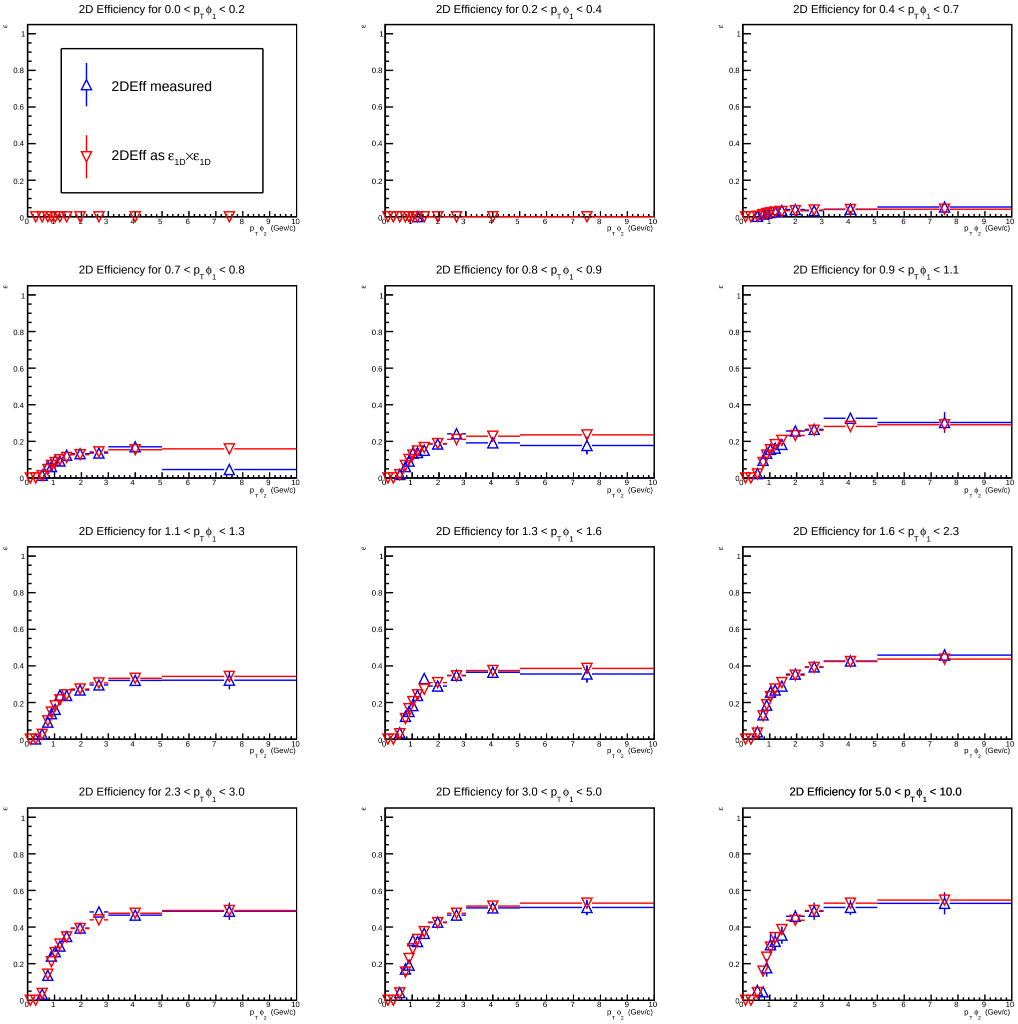

FIGURE 4.5: 2-Dimensional efficiency and acceptance compared to the 1-Dimensional product.

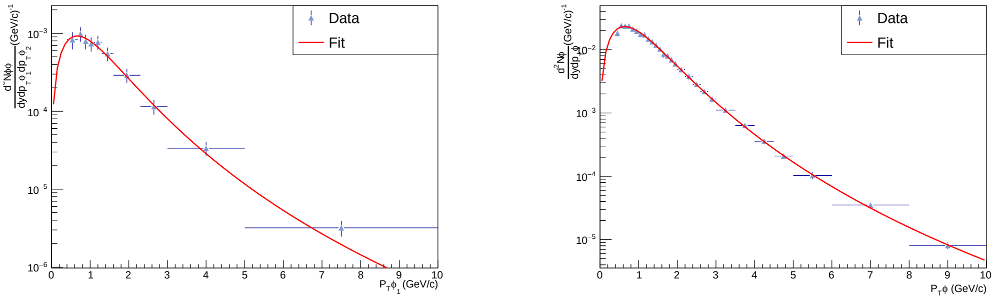

(A) Simple conditional yield for the 2-Dimensional analysis with Levy-Tsallis fit highlighted.

(B) Inclusive yield for the 1-Dimensional analysis with fit of the Levy-Tsallis highlighted.

FIGURE 4.6

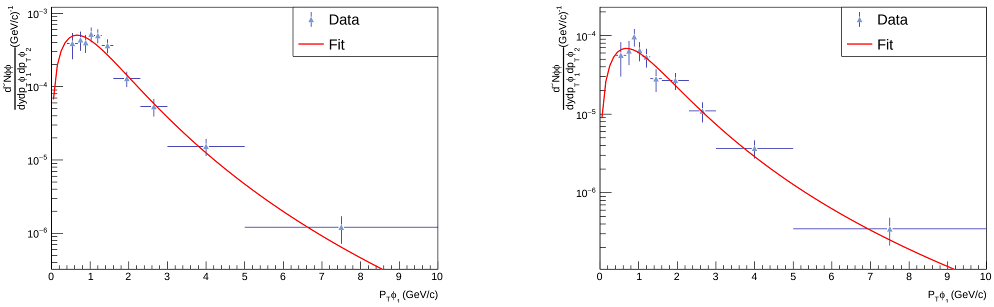

FIGURE 4.7: Measurements of double conditional yields for the 2-Dimensional analysis where $p_T\phi_2$ [1.1-1.3] (left) and [2.3-3.0] (right).

	Default Fit	Systematics measurement
ϕ mass	Free	Fixed
ϕ width	Free	Fixed
Resolution par.	Free	Free
Background function	4° Chebyshev	3° Chebyshev 5° Chebyshev
Fit Range	[0.99-1.05]	All combinations for: Min. val. 0.990,0.995,1.000 Max. val. 1.040,1.050,1.060,1.070

TABLE 4.3: Summary of the standard fit procedure parameters and their variations in fit procedure to determine the systematic uncertainty related to signal extraction.

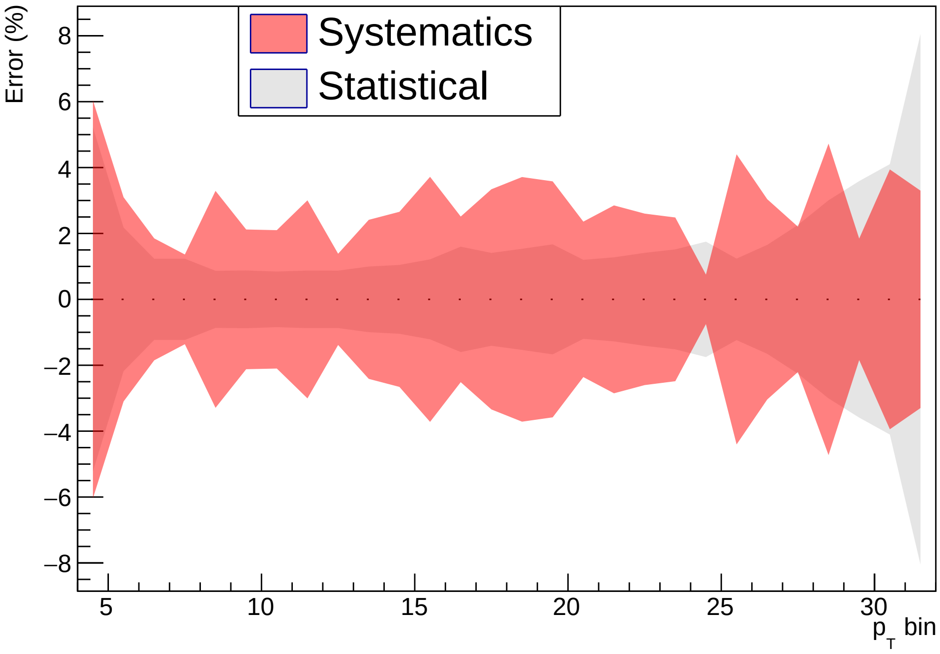

FIGURE 4.8: Comparison of Systematic and Statistical error for the Signal Extraction in the inclusive production analysis.

the systematic variations is listed in Table 4.3.

After a bin-by-bin estimation is achieved, we consider the mean and RMS of the variations. This is done in an attempt to make the safest assumption and to avoid underestimating the signal extraction systematic uncertainty. A summary of the systematic uncertainties assigned to the raw signal extraction in the 1-Dimensional case are shown in Figure 4.8. A summary of the systematic uncertainties assigned to the raw signal extraction as a function of p_T in the 2-Dimensional case are shown in Figures 4.9-4.10-4.11.

In both cases there is the possibility that the limited statistical precision may have caused an overestimate of the systematic uncertainty. In particular for the p_T bins where the statistical uncertainty is large there is a hint of an increase of the systematic uncertainty, which might be a sign of the fact that statistical fluctuations have a role into the procedure for the estimation of the systematic uncertainties. For this reason a mean has been performed to smooth over those bins, and the result has been rounded up to account for greater variations. This is a very rudimental approach that will need refinement in the near future, together with a new assessment of the other systematics, but can nonetheless give a sense of the actual entity of the systematic uncertainties.

We have decided to assign the systematic uncertainty of the raw signal extraction a constant value as a function of p_T, being 3% for the inclusive analysis and conservatively 10% for the 2D analysis. It has to be noticed that the assigned 3% for the inclusive analysis is in line with the systematic uncertainty estimated for the published results [34] that accounted for a 2-10% systematic error on the signal extraction. A summary of the assigned systematic uncertainties is reported in Table 4.4.

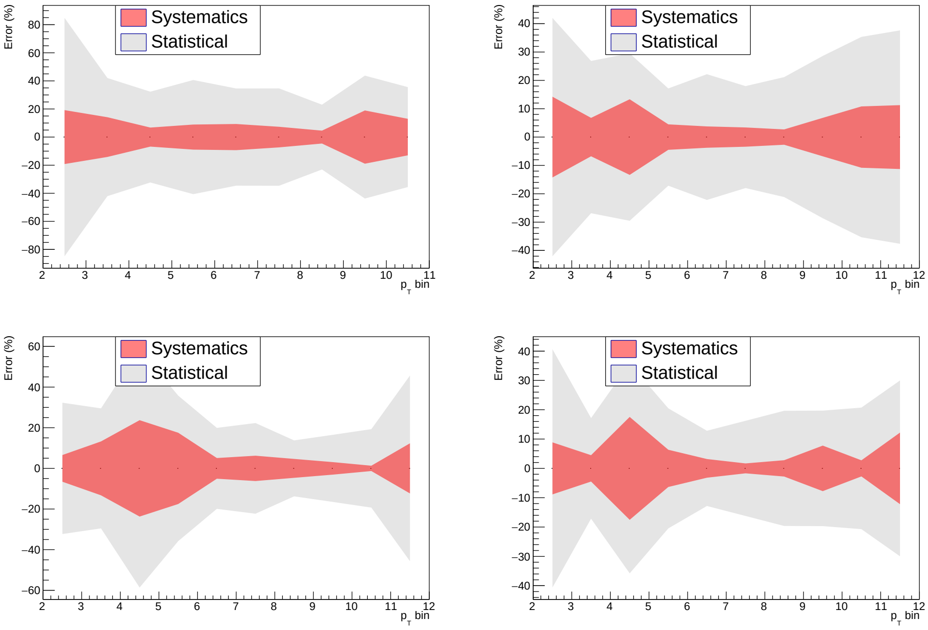

FIGURE 4.9: Comparison of Systematic and Statistical error for the Signal Extraction in the 2-Dimensional analysis for p_T [0.4-0.68], [0.68-0.82], [0.82-0.95]. [0.95-1.1]

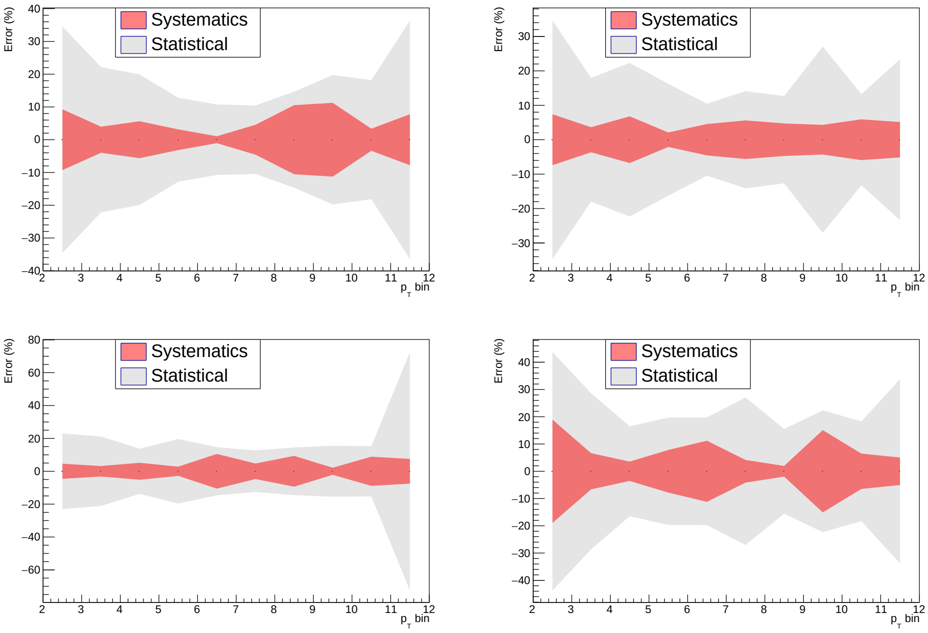

FIGURE 4.10: Comparison of Systematic and Statistical error for the Signal Extraction in the 2-Dimensional analysis for p_T [1.1-1.3], [1.3-1.6], [1.6-2.3]. [2.3-3.0]

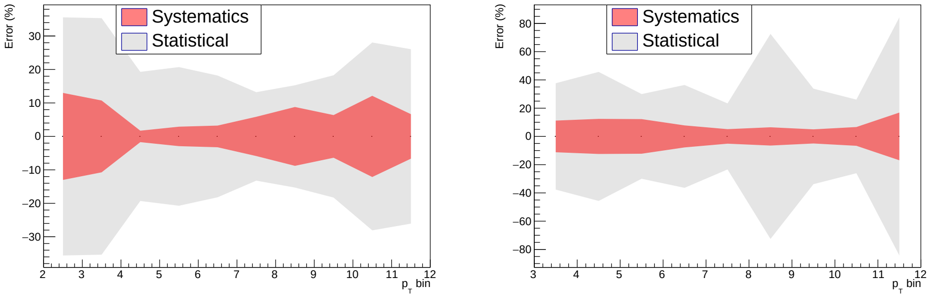

FIGURE 4.11: Comparison of Systematic and Statistical error for the Signal Extraction in the 2-Dimensional analysis for p_T [3.0-5.0], [5.0-10.]

	1-Dimensional	2-Dimensional
Branching Ratio [11]	0.5%	1%
Tracking [34]	8.0%	16.0%
PID [34]	1.5%	3.0%
Trigger efficiency [34]	$^{+6.2\%}_{-3\%}$	$^{+6.2\%}_{-3\%}$
Signal Extraction	3.0%	10.0%

TABLE 4.4: Summary of the Systematic uncertainties used in the analysis

4.1.9 Mean p_T measurement

As a secondary measurement, the mean transverse momentum of the ϕ-meson production spectra, can be performed to further characterize the measurement. The mean transverse momentum characterizes the shape of the spectrum and can be a useful tool to quickly describe it. We report the mean p_T ($\langle p_T \rangle_\phi$) of the differential yield, together with the mean p_T ($\langle p_T \rangle_{\phi\phi}$) of the simple differential yield and report all the double differential yields mean p_T in Figure 4.12.

The results are shown in Table 4.5. The mean transverse momentum of the 1-Dimensional analysis can be compared to the one reported in [34]. In this Thesis only the statistical errors are reported, as a systematic assessment was not performed yet. There is a visible discrepancy between the [34] reported value and the measured one. This discrepancy can be explained by the spectrum being harder than the one previously measured, with up to 20% difference at high p_T. The reason for this discrepancy is under investigation.

	Measured p_T	$\langle p_T \rangle_\phi$	$\langle p_T \rangle_{\phi\phi}$
This Thesis	[0.4 -10] GeV/c	1.161±0.005	1.30±0.05
Previous Paper [34]	[0.4 -6] GeV/c	1.07±0.005±0.03	\

TABLE 4.5: Final result for the 1-Dimensional and 2-Dimensional mean transverse momentum.

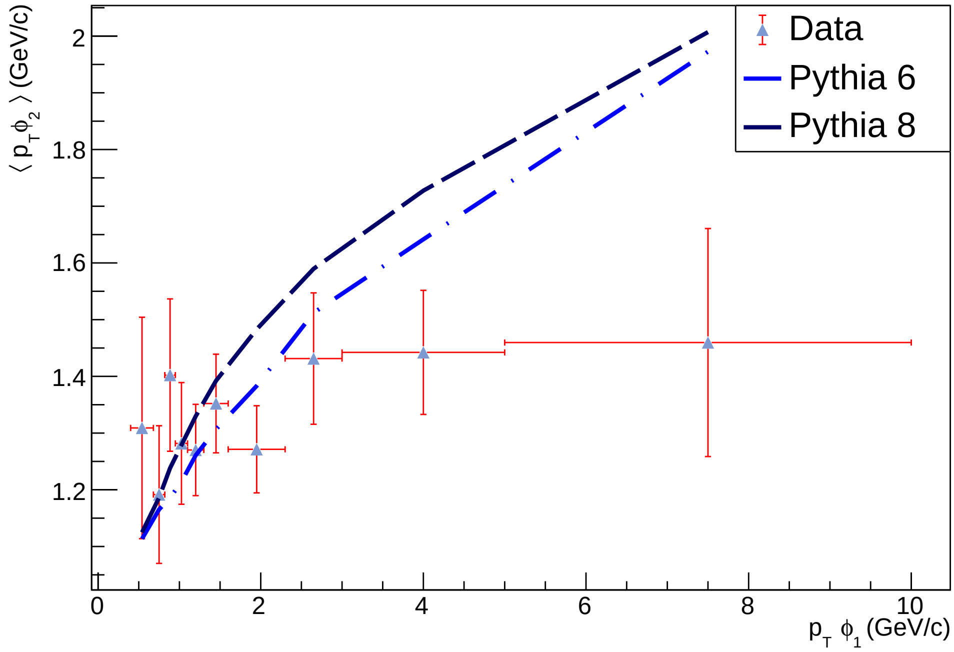

FIGURE 4.12: Mean transverse momentum of the conditional yields in the 2-Dimensional analysis.

4.2 Results

The final results of the analysis are the inclusive yields for the ϕ meson ($\mathrm{d}N_{\phi}/\mathrm{d}y$) and the ϕ meson pairs ($\mathrm{d}N_{\phi\phi}/\mathrm{d}y$), together with the parameters characterizing the production statistics we discussed in Chapter 3: the production probability mean (μ_{ϕ}) and variance (σ^2_{ϕ}), the yields ratio (($\mathrm{d}N_{\phi\phi}/\mathrm{d}y)/(\mathrm{d}N_{\phi}/\mathrm{d}y)^2$) and the γ_{ϕ} parameter. A summary of these measurements is given in Table 4.6.

We can start our results review from the inclusive yield of ϕ mesons. The measured ϕ-meson yield $\mathrm{p_T}$ spectrum is compared to the Pythia Monte Carlo predictions from the two versions used in the analysis (Fig. 4.13). Furthermore the measured inclusive ϕ-meson yield is also compared to the Pythia Monte Carlo predictions (Fig. 4.19a). The inclusive yield can also be compared to the measurement performed in [34], so its results are listed along in Table 4.6 and the measured ϕ-meson yield $\mathrm{p_T}$ spectra are compared in Figure 4.14. The spectrum is harder than the one previously measured, with up to 20% difference at high $\mathrm{p_T}$. The reason for this discrepancy is under investigation.

The inclusive conditional ϕ-meson pair yield $\mathrm{p_T}$ spectra are compared in a similar fashion with the Monte Carlo generators in Figures 4.15, 4.16 and 4.17. Furthermore the second conditional spectrum, built from the integration of the previous conditional yields, can be compared to Monte Carlo predictions (Fig. 4.18). The measured inclusive ϕ-meson yield and Pythia predictions are listed in Table 4.6. Again the spectra seem to differ from the Pythia predictions, nonetheless the two versions systematically over and underestimate the inclusive yields (Figs. 4.19a-4.19b).

As far as the parameter we introduce in Chapter 3 are concerned, a more careful discussion should be carried out. The mean of the production distribution (μ_{ϕ}) is the inclusive ϕ-meson yield, and thus has already been discussed. The variance of the distribution (σ^2_{ϕ}) is less straightforward: recalling equation 4.1.9, its derivation relies on a combination of the 1-D and 2-D yields. The yields measurements have a too large error to constrain this quantity as an absolute value with sufficient precision to drive conclusions about the physics of the process.

Conversely the yields ratio and the γ_{ϕ} parameter benefit from a very useful cancellation; given they rely on ratios, many systematic errors can be assumed to partially cancel out. It is the case of (($\mathrm{d}N_{\phi\phi}/\mathrm{d}y)/(\mathrm{d}N_{\phi}/\mathrm{d}y)^2$), where the systematics for Tracking, PID, Branching Ratio are greatly reduced, and can be then combined with the full Trigger efficiency and Signal Extraction. Even though, to the sole purpose of systematic cancelation, the more natural ratio would be $(\mathrm{d}N_{\phi\phi}/\mathrm{d}y)/(2\mathrm{d}N_{\phi}/\mathrm{d}y)$. The proposed ratio has the advantage of being directly comparable to a poissonian distribution, that will always yield 1/2. Given the measurement are dominated by systematics, these cancellations greatly help the measurement precision. In fact this measurement has a satisfying precision, although it is a preliminary result that can be refined in the future with improved precision. This leaves a number of open possibilities for future measurements. Its comparison with Pythia generators (Fig: 4.20a) suggests the over and underestimation is still present.

Similarly, the γ_{ϕ} parameter benefits from the ratio error compensations. For this measurement we only considered the 1-Dimensional analysis systematics, combined with the 2-Dimensional Signal Extraction systematic. Here again, these cancellations help in improving the error that give the result a good significance. Its comparison with Pythia generators (Fig: 4.20b) shows a surprisingly good agreement between the two Pythia versions and the data, despite the discrepancies observed in the case of the other observables. Improvements on the resolution of this measurement would be greatly beneficial to a more thorough characterization of the statistics

	Measured p_T	$\mathrm{d}N_{\phi}/\mathrm{d}y$ ($\times 10^3$)	$\mathrm{d}N_{\phi\phi}/\mathrm{d}y$ ($\times 10^3$)
This Thesis	[0.4 - 10] GeV/c	$33 \pm 0.2^{+3.6}_{-3.1}$	$1.44 \pm 0.05^{+0.29}_{-0.28}$
Previous Publication [34]	[0.4 - 6] GeV/c	$32 \pm 0.4^{+4.0}_{-3.5}$	\
Pythia 6	-	27	1.06
Pythia 8	-	39	1.86

	$(\mathrm{d}N_{\phi\phi}/\mathrm{d}y)/(\mathrm{d}N_{\phi}/\mathrm{d}y)^2$	σ^2_{ϕ}	$\sigma^2_{\phi}/\mu_{\phi} - 1$ (%)
This Thesis	$1.30 \pm 0.04^{+0.}_{-0.}$	$0.035 \pm 0.05^{+0.25}_{-0.22}$	$5.33 \pm 0.36 \pm 2.7$
Pythia 6	1.42	0.029	5.05
Pythia 8	1.20	0.042	5.48

TABLE 4.6: (Top) Measured inclusive ϕ meson yield and inclusive ϕ meson pair yield compared to the previous publication results. (Bottom) Measured ratio of inclusive ϕ meson pairs yield to the inclusive ϕ meson yield squared, measured production distribution variance (see Eq. 4.1.9), measured deviation from the Poissonian distribution.

properties.

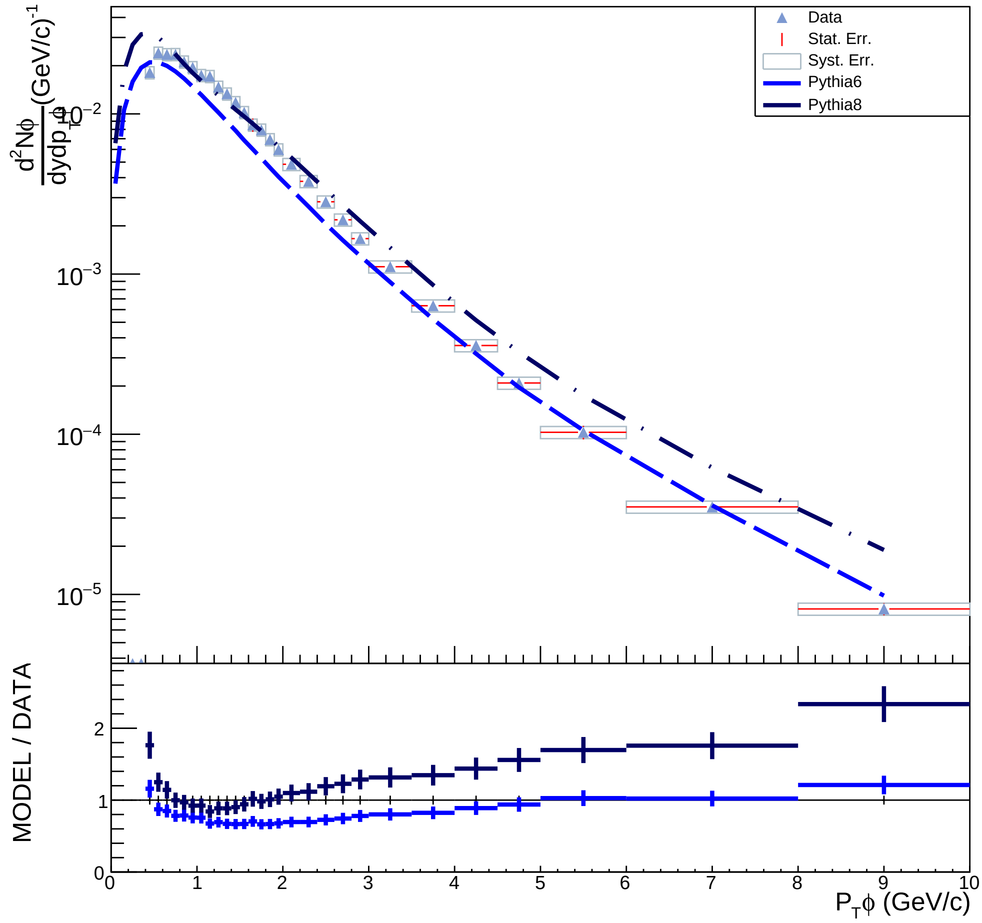

FIGURE 4.13: Comparison of Results with PYTHIA 6 and 8 Monte Carlo generators, with their ratio. From top left to bottom right the results are the 1-Dimensional yield

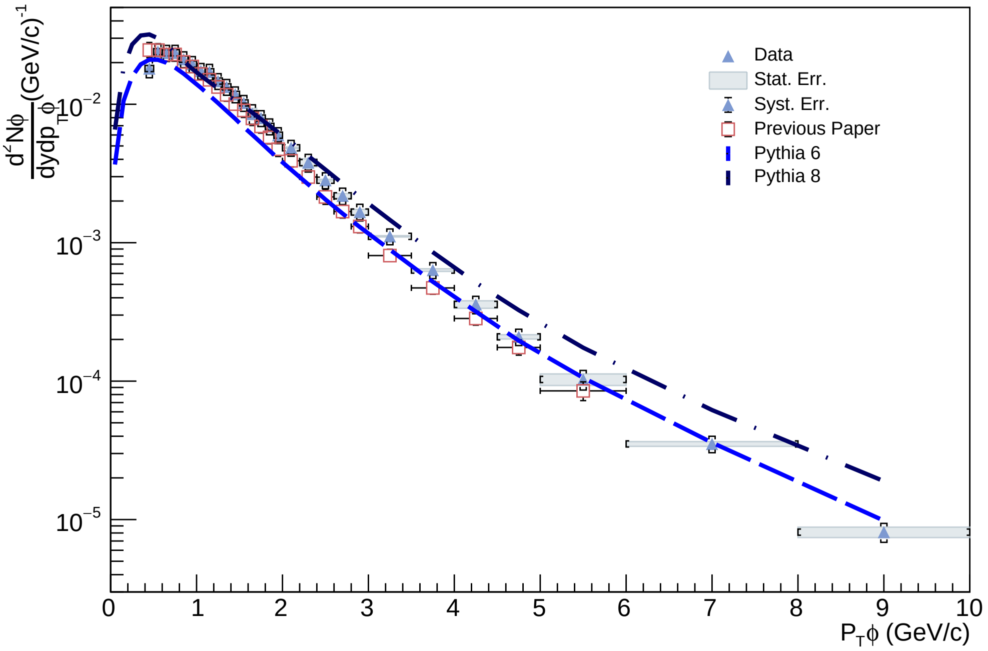

FIGURE 4.14: Comparison of Results to Pythia 6 Monte Carlo, Pythia 8 Monte Carlo and results from [34].

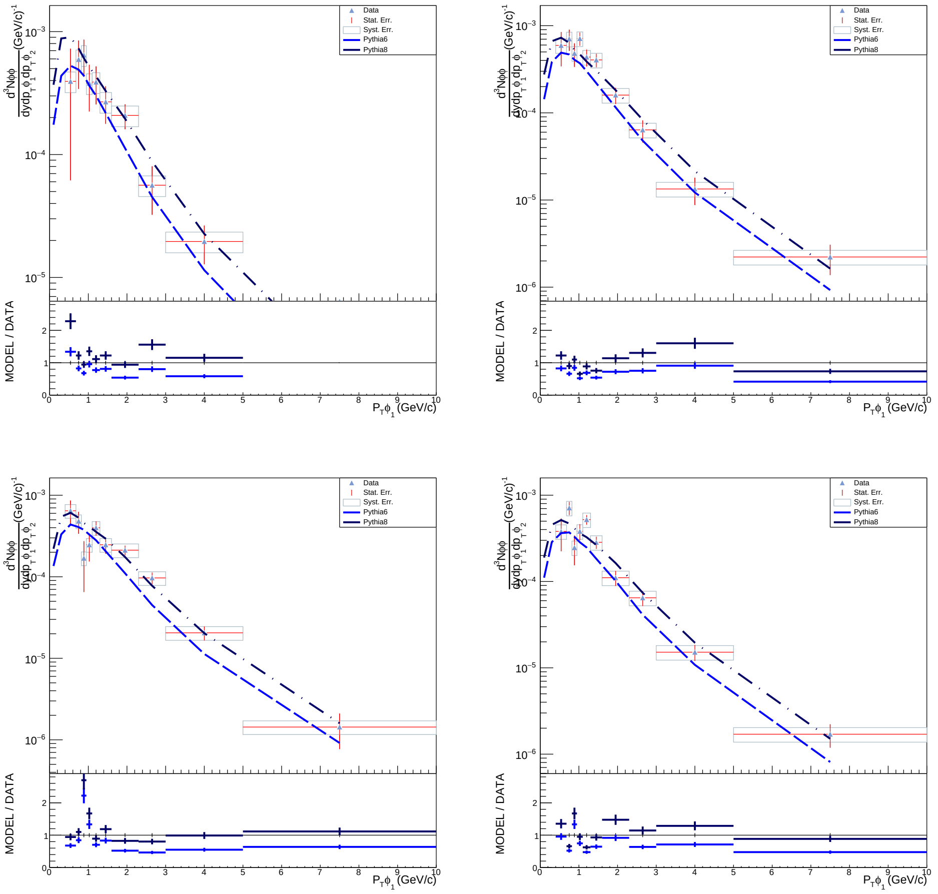

FIGURE 4.15: Comparison of Results with PYTHIA 6 and 8 Monte Carlo generators, with their ratio. From top left to bottom right the results are the conditional yields for p_T [0.4-0.68], [0.68-0.82], [0.82-0.95]. [0.95-1.1]

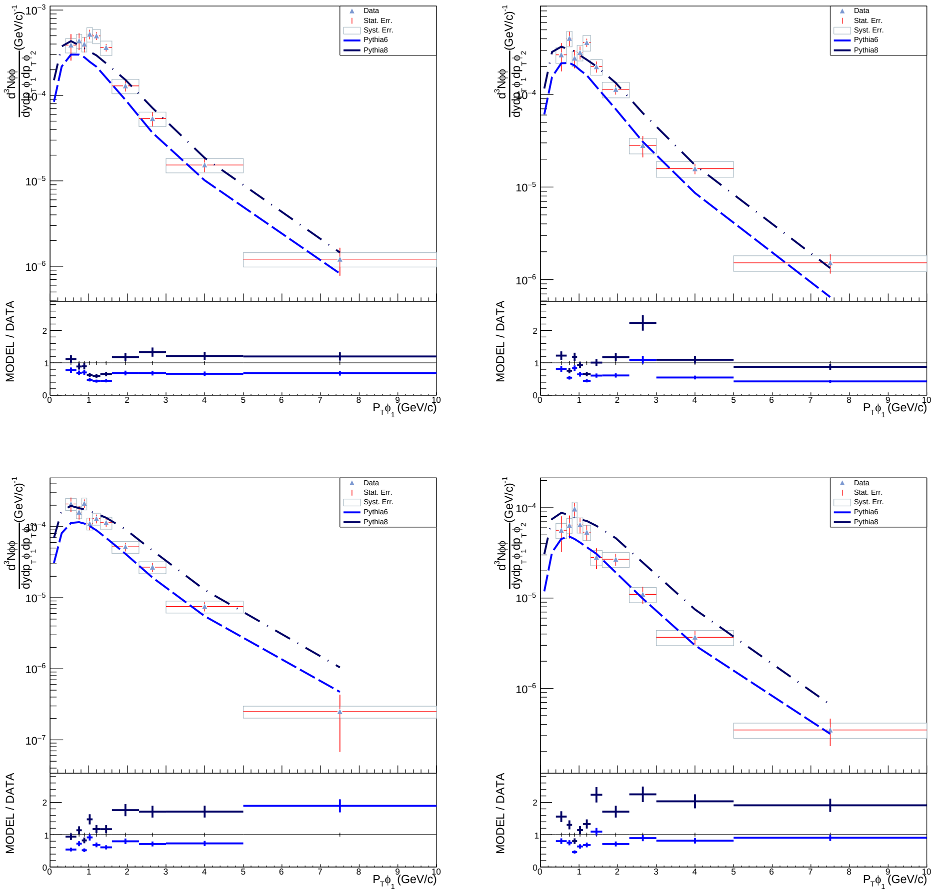

FIGURE 4.16: Comparison of Results with PYTHIA 6 and 8 Monte Carlo generators, with their ratio. From top left to bottom right the results are the conditional yields for p_T [1.1-1.3], [1.3-1.6], [1.6-2.3]. [2.3-3.0]

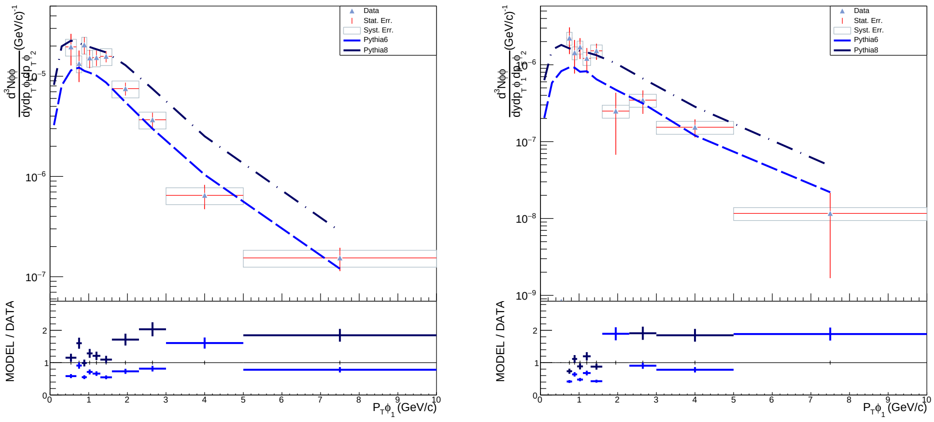

FIGURE 4.17: Comparison of Results with PYTHIA 6 and 8 Monte Carlo generators, with their ratio. From top left to bottom right the results are the conditional yields for p_T [3.0-5.0], [5.0-10.]

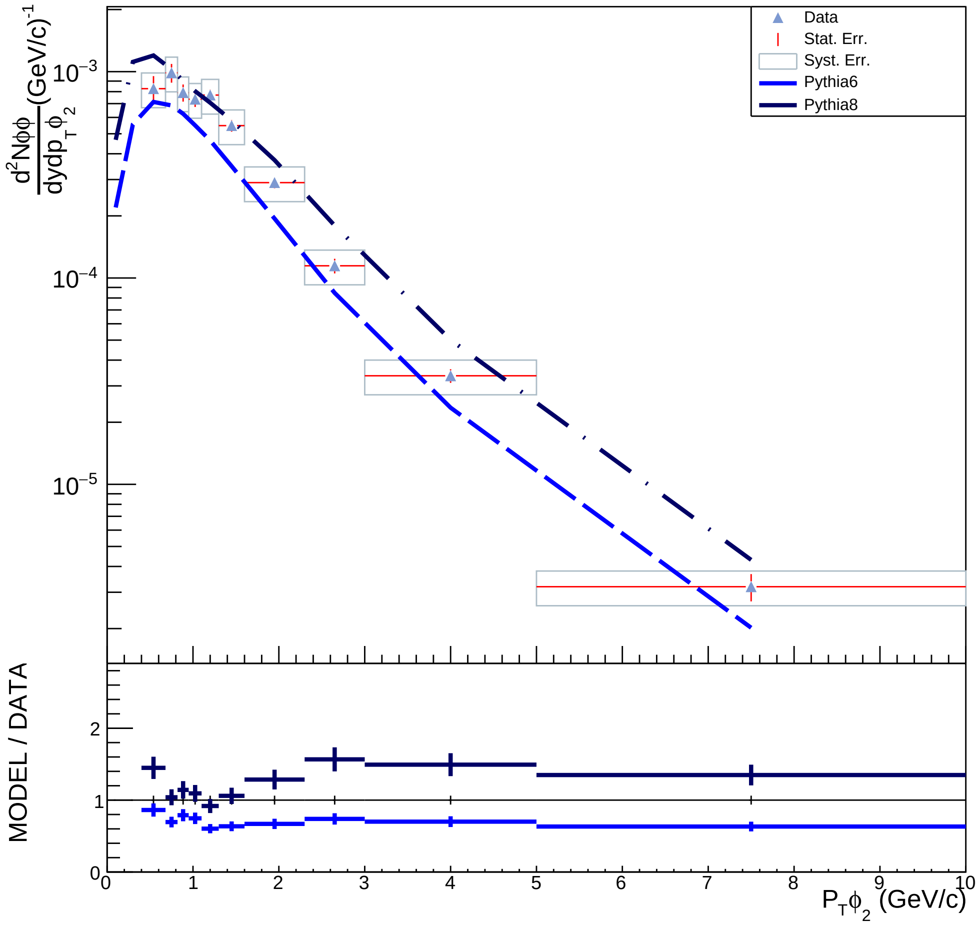

FIGURE 4.18: Comparison of Results with PYTHIA 6 and 8 Monte Carlo generators, with their ratio. The results are the integrated 2D yields.

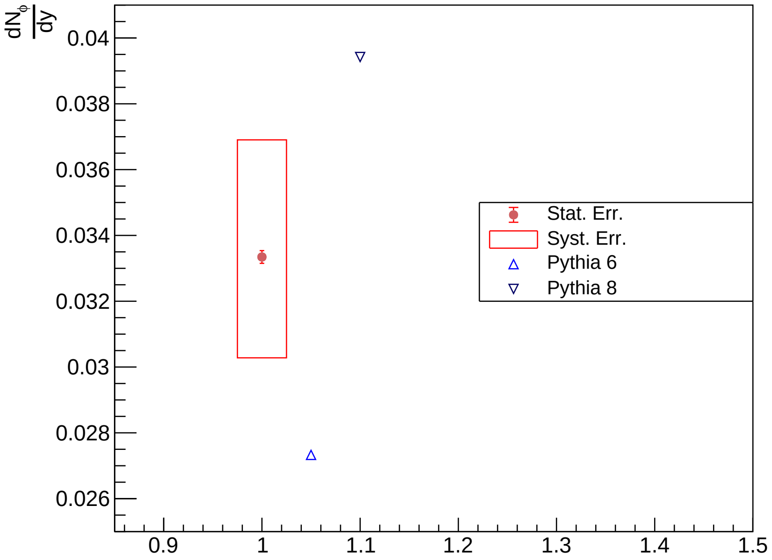

(A) Inclusive ϕ meson yield compared to Pythia predictions.

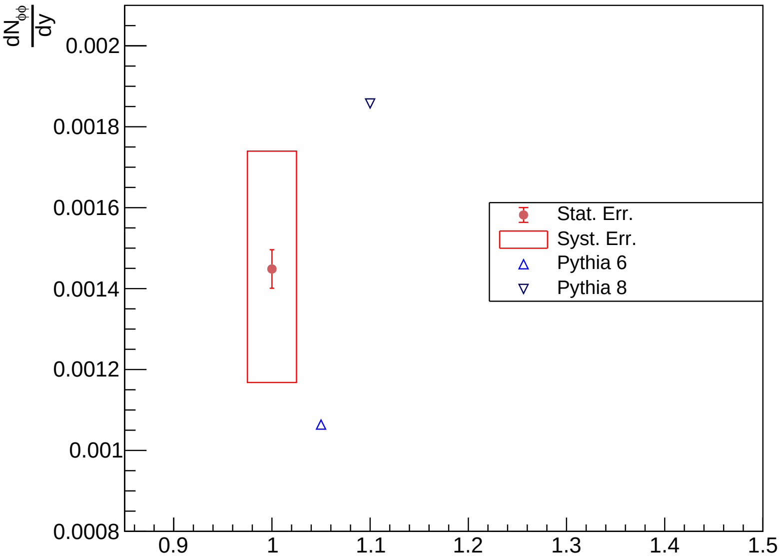

(B) Inclusive ϕ meson pair yield compared to Pythia predictions.

FIGURE 4.19

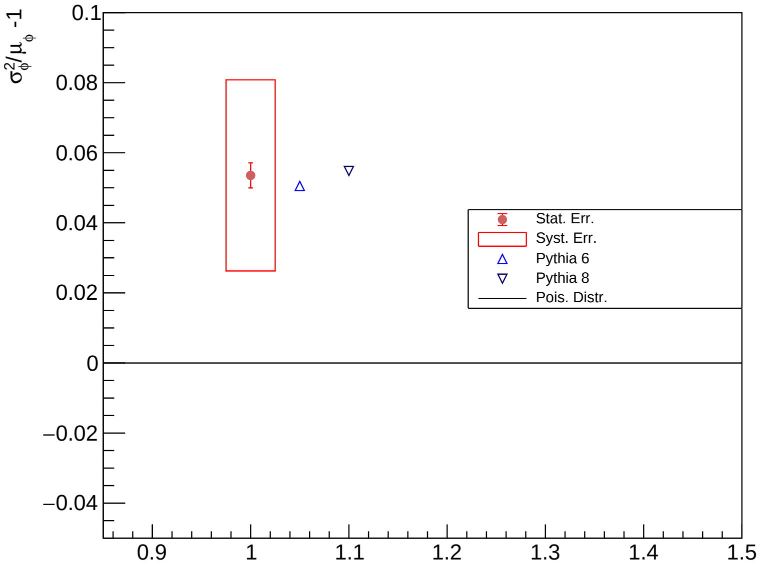

(A) Poisson deviation parameter as measured in data and as predicted in Pythia generators

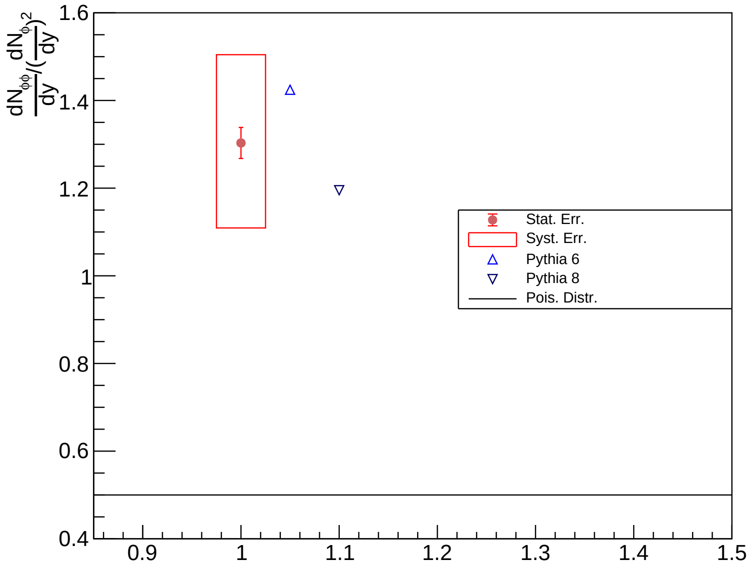

(B) Ratio of measured inclusive yield, ϕ pairs to ϕ squared.

FIGURE 4.20

Conclusions

In the present thesis we explored the possibility of performing a novel measurement with the ALICE experiment at the LHC, namely the measurement of the yield of pairs of ϕ mesons in proton-proton collisions.

The analysis technique extends the concepts of the classical invariant-mass analysis into a multidimensional invariant-mass space (2D in this case). The framework for the data analysis has been developed using a simplified analysis environment based on Pythia8 Monte Carlo events, providing evidence in favor of the feasibility of the technique and its validation for use on real data. In the Monte Carlo we tested and validated many assumptions that helped designing the analysis and improve its accuracy.

After the technique was established, it has been employed on a set of ALICE data, on which the inclusive ϕ meson yield was already measured, to have a reference to check. The inclusive (1-Dimensional) measurement could be reproduced within the uncertainties of the previous measurement, with a smaller statistical error.

The 2-Dimensional yield is a novel measurement, never performed before. The presented result represent a very good first estimate of the production of ϕ-meson pairs. This thesis has proven the feasibility of the technique and the possibility to perform such a multi-differential measurement with the ALICE experiment at the LHC. A larger statistical sample is expected to improve the analysis both in terms of statistical precision and in terms of the systematic uncertainties.

These first results open a new way to evaluate a number of parameters defining the production mechanisms of the ϕ meson, and consequently the strangeness production. We discussed about the statistical properties of the ϕ meson production in pp collisions at $\sqrt{s} = 7$ TeV, giving a first estimate for the mean and variance of the distribution. Moreover, the ratio of yield of ϕ meson pairs with respect to the inclusive ϕ meson yield is expected to show the degree of correlation in the production of ϕ meson pairs in hadronic collisions. The measurement reported in this thesis for this ratio is in qualitative agreement with the expectations from the Lund String Model, as it shows an enhancement of the production with respect to the simple poissonian expectation of the ratio being $1/2$.

This correlation in production is reflected in the deviation of the distribution deviance from a poissonian hypothesis (γ_ϕ). This deviation shows a surprisingly good agreement between the data and Pythia Monte Carlo. This might indicate that the Lund String Fragmentation Model correctly describes the degree of correlations in the production of ϕ-meson pairs, regardless of the details of the different tunes employed in Pythia 6 and 8.

It will be crucial to test other Monte Carlo event generator models against this measurement, especially those that employ different phenomenological mechanisms of hadronisation.

Bibliography

[1] "Performance of the ALICE experiment at the CERN LHC". In: *International Journal of Modern Physics A* 29.24 (2014), p. 1430044. ISSN: 1793-656X. DOI: `10.1142/s0217751x14300440`. URL: `http://dx.doi.org/10.1142/S0217751X14300440`.

[2] P. Skands. "Introduction to QCD". In: *Searching for New Physics at Small and Large Scales* (2013). DOI: `10.1142/9789814525220_0008`. URL: `http://dx.doi.org/10.1142/9789814525220_0008`.

[3] Helmut Satz. "The Quark-Gluon Plasma: A Short Introduction". In: *Nuclear Physics A* 862-863 (2011), pp. 4–12. ISSN: 0375-9474. DOI: `10.1016/j.nuclphysa.2011.05.014`. URL: `http://dx.doi.org/10.1016/j.nuclphysa.2011.05.014`.

[4] Peter Koch, Berndt M¸ller, and Johann Rafelski. "From strangeness enhancement to quark-gluon plasma discovery". In: *International Journal of Modern Physics A* 32.31 (2017), p. 1730024. ISSN: 1793-656X. DOI: `10.1142/s0217751x17300241`. URL: `http://dx.doi.org/10.1142/S0217751X17300241`.

[5] S. Acharya et al. "Suppression of Λ(1520) resonance production in central Pb-Pb collisions at $\sqrt{s_{NN}} = 2.76 TeV$". In: *Physical Review C* 99.2 (2019). ISSN: 2469-9993. DOI: `10.1103/physrevc.99.024905`. URL: `http://dx.doi.org/10.1103/PhysRevC.99.024905`.

[6] "Enhanced production of multi-strange hadrons in high-multiplicity proton-proton collisions". In: *Nature Physics* 13.6 (2017), pp. 535–539. ISSN: 1745-2481. DOI: `10.1038/nphys4111`. URL: `http://dx.doi.org/10.1038/nphys4111`.

[7] Vojtich PacÌk. "Elliptic flow of identified hadrons in small collisional systems measured with ALICE". In: *Nuclear Physics A* 982 (2019), pp. 451–454. ISSN: 0375-9474. DOI: `10.1016/j.nuclphysa.2018.09.020`. URL: `http://dx.doi.org/10.1016/j.nuclphysa.2018.09.020`.

[8] Christian Klein-Bˆsing. *New Results on Hard Probes in Heavy-Ion Collisions with ALICE*. 2018. arXiv: `1809.04936 [hep-ex]`.

[9] S. Acharya et al. "Measurements of inclusive jet spectra in pp and central Pb-Pb collisions at $\sqrt{s_{NN}}$=5.02TeV". In: *Physical Review C* 101.3 (2020). ISSN: 2469-9993. DOI: `10.1103/physrevc.101.034911`. URL: `http://dx.doi.org/10.1103/PhysRevC.101.034911`.

[10] S. Acharya et al. "Measurements of inclusive jet spectra in pp and central Pb-Pb collisions at sNN=5.02TeV". In: *Physical Review C* 101.3 (2020). ISSN: 2469-9993. DOI: `10.1103/physrevc.101.034911`. URL: `http://dx.doi.org/10.1103/PhysRevC.101.034911`.

[11] M. Tanabashi et al. "Review of Particle Physics". In: *Phys. Rev. D* 98 (3 2018), p. 030001. DOI: `10.1103/PhysRevD.98.030001`. URL: `https://link.aps.org/doi/10.1103/PhysRevD.98.030001`.

[12] S. Acharya et al. "Υ suppression at forward rapidity in Pb-Pb collisions at sNN=5.02TeV". In: *Physics Letters B* 790 (2019), pp. 89–101. ISSN: 0370-2693. DOI: `10.1016/j.physletb.2018.11.067`. URL: `http://dx.doi.org/10.1016/j.physletb.2018.11.067`.

[13] B. Abelev et al. "Suppression of Υ (1S)at forward rapidity in Pb-Pb collisions atsNN=2.76TeV". In: *Physics Letters B* 738 (2014), pp. 361–372. ISSN: 0370-2693. DOI: `10.1016/j.physletb.2014.10.001`. URL: `http://dx.doi.org/10.1016/j.physletb.2014.10.001`.

[14] E. L. Bratkovskaya, O. Linnyk, and W. Cassing. *Electromagnetic probes of the QGP*. 2014. DOI: `https://doi.org/10.1002/asna.201913580`. arXiv: `1409.4190 [nucl-th]`.

[15] S. Acharya et al. "Direct photon elliptic flow in Pb-Pb collisions at sNN=2.76 TeV". In: *Physics Letters B* 789 (2019), pp. 308–322. ISSN: 0370-2693. DOI: `10.1016/j.physletb.2018.11.039`. URL: `http://dx.doi.org/10.1016/j.physletb.2018.11.039`.

[16] Johann Rafelski and Berndt Müller. "Strangeness Production in the Quark-Gluon Plasma". In: *Phys. Rev. Lett.* 48 (16 1982), pp. 1066–1069. DOI: `10.1103/PhysRevLett.48.1066`. URL: `https://link.aps.org/doi/10.1103/PhysRevLett.48.1066`.

[17] F. Becattini. *An introduction to the Statistical Hadronization Model*. 2009. arXiv: `0901.3643 [hep-ph]`.

[18] Peter Braun-Munzinger, Krzysztof Redlich, and Johanna Stachel. "PARTICLE PRODUCTION IN HEAVY ION COLLISIONS". In: *Quark-Gluon Plasma 3* (2004), pp. 491–599. DOI: `10.1142/9789812795533_0008`. URL: `http://dx.doi.org/10.1142/9789812795533_0008`.

[19] Volodymyr Vovchenko, Benjamin D˜nigus, and Horst Stoecker. "Canonical statistical model analysis of p-p, p-Pb, and Pb-Pb collisions at energies available at the CERN Large Hadron Collider". In: *Physical Review C* 100.5 (2019). ISSN: 2469-9993. DOI: `10.1103/physrevc.100.054906`. URL: `http://dx.doi.org/10.1103/PhysRevC.100.054906`.

[20] Vytautas Vislavicius and Alexander Kalweit. *Multiplicity dependence of light flavour hadron production at LHC energies in the strangeness canonical suppression picture*. 2016. arXiv: `1610.03001 [nucl-ex]`.

[21] T. Pierog et al. "EPOS LHC: Test of collective hadronization with data measured at the CERN Large Hadron Collider". In: *Physical Review C* 92.3 (2015). ISSN: 1089-490X. DOI: `10.1103/physrevc.92.034906`. URL: `http://dx.doi.org/10.1103/PhysRevC.92.034906`.

[22] S. Acharya et al. "Multiplicity dependence of (multi-)strange hadron production in proton-proton collisions at $\sqrt{s}$s†=†13 TeV". In: *The European Physical Journal C* 80.2 (2020). ISSN: 1434-6052. DOI: `10.1140/epjc/s10052-020-7673-8`. URL: `http://dx.doi.org/10.1140/epjc/s10052-020-7673-8`.

[23] J. Aichelin and K. Werner. "Centrality dependence of strangeness enhancement in ultrarelativistic heavy ion collisions: A core-corona effect". In: *Phys. Rev. C* 79 (6 2009), p. 064907. DOI: `10.1103/PhysRevC.79.064907`. URL: `https://link.aps.org/doi/10.1103/PhysRevC.79.064907`.

[24] Silvia Ferreres-SolÈ and Torbj˚rn Sj˚strand. “The space-time structure of hadronization in the Lund model”. In: *The European Physical Journal C* 78.11 (2018). ISSN: 1434-6052. DOI: 10.1140/epjc/s10052-018-6459-8. URL: http://dx.doi.org/10.1140/epjc/s10052-018-6459-8.

[25] Christian Bierlich et al. “Effects of overlapping strings in pp collisions”. In: *Journal of High Energy Physics* 2015.3 (2015), p. 148. DOI: 10.1007/JHEP03(2015)148. URL: https://doi.org/10.1007/JHEP03(2015)148.

[26] R. Stock et al. “Strangeness enhancement in central S + S collisions at 200 GeV/nucleon”. In: *Nuclear Physics A* 525 (1991), pp. 221 –226. ISSN: 0375-9474. DOI: https://doi.org/10.1016/0375-9474(91)90328-4. URL: http://www.sciencedirect.com/science/article/pii/0375947491903284.

[27] Esma Mobs. *The CERN accelerator complex - August 2018. Complexe des accÈlÈrateurs du CERN - Ao˚t 2018*. 2018. URL: https://cds.cern.ch/record/2636343.

[28] G. Contin. *The MAPS-based ITS Upgrade for ALICE*. 2020. arXiv: 2001.03042 [physics.ins-det].

[29] In: *Nuclear Instruments and Methods in Physics Research Section A: Accelerators, Spectrometers, Detectors and Associated Equipment* 881 (2018), pp. 88–127. ISSN: 0168-9002. DOI: 10.1016/j.nima.2017.09.028. URL: http://dx.doi.org/10.1016/j.nima.2017.09.028.

[30] Nicolo Jacazio. “PID performance of the ALICE-TOF detector in Run 2”. In: *PoS* LHCP2018.arXiv:1809.00574 (2018), 232. 7 p. DOI: 10.22323/1.321.0232. URL: http://cds.cern.ch/record/2637371.

[31] Giacomo Volpe. “PID performance of the High Momentum Particle IDentification (HMPID) detector during LHC-Run 2”. In: *Nuclear Instruments and Methods in Physics Research Section A: Accelerators, Spectrometers, Detectors and Associated Equipment* 952 (2020). 10th International Workshop on Ring Imaging Cherenkov Detectors (RICH 2018), p. 161803. ISSN: 0168-9002. DOI: https://doi.org/10.1016/j.nima.2019.01.030. URL: http://www.sciencedirect.com/science/article/pii/S0168900219300695.

[32] D. Blau. “Performance of the ALICE electromagnetic calorimeters in LHC Runs 1 and 2 and upgrade projects”. In: *Journal of Instrumentation* 15.03 (2020), pp. C03025–C03025. ISSN: 1748-0221. DOI: 10.1088/1748-0221/15/03/c03025. URL: http://dx.doi.org/10.1088/1748-0221/15/03/C03025.

[33] Sabyasachi Siddhanta. “Muon physics at forward rapidity with the ALICE detector upgrade”. In: *Nuclear Physics A* 982 (2019). The 27th International Conference on Ultrarelativistic Nucleus-Nucleus Collisions: Quark Matter 2018, pp. 947 –950. ISSN: 0375-9474. DOI: https://doi.org/10.1016/j.nuclphysa.2018.10.034. URL: http://www.sciencedirect.com/science/article/pii/S0375947418303154.

[34] B. Abelev et al. “Production of K*(892)0 and ϕ(1020) in pp collisions at $\sqrt{s} =$ 7 TeV”. In: *The European Physical Journal C* 72.10 (2012). ISSN: 1434-6052. DOI: 10.1140/epjc/s10052-012-2183-y. URL: http://dx.doi.org/10.1140/epjc/s10052-012-2183-y.

[35] S Hageb˚ck and L Moneta. “Making RooFit Ready for Run 3”. In: *Journal of Physics: Conference Series* 1525 (2020), p. 012114. ISSN: 1742-6596. DOI: 10.1088/1742-6596/1525/1/012114. URL: http://dx.doi.org/10.1088/1742-6596/1525/1/012114.